Diffuse Molecular Gas in the Cygnus X Star Forming Region and its Effect on the Star Formation Law

by

Kaylie Green

A thesis submitted in partial fulfillment of the requirements for the degree of

Master of Science

Department of Physics

University of Alberta

Abstract

Observations of star forming regions in our Milky Way show that there are two different forms of molecular gas: bright star forming molecular clouds and large diffuse clouds. What is not yet known is the difference in physical properties between these two types of molecular gas and the contribution of these diffuse clouds to the star formation efficiency in our galaxy. In this thesis I identify physical properties of low surface brightness gas in the nearby star forming regions of Cygnus X and W80, and explore the presence of these diffuse clouds as solutions to the increased efficiency of star formation observed in local clouds. I find that these low surface brightness clouds do not contribute in a significant way to the total molecular gas mass of the region. I also find that the method used for tracing star formation has a larger effect on the calculation of large scale star formation rate than previously thought.

"The wonder is, not that the field of stars is so vast, but that man has measured it."

Anatole France

The Garden of Epicurus (1894)

Acknowledgements

First of all, I would like to thank all of the members of my committee for their support and advice over the last couple years. Thank you to Greg Sivakoff for both his helpful science advice and life advice over the last couple of years. Also a big thanks for all of his attention to detail while reviewing this thesis. Thank you to Roland Kothes for all of the guidance and lessons on data reduction! Also thank you to both Roland and Erik for the opportunity to go to Hawaii to collect my data.

I would like to thank Erik Rosolowsky for being an excellent supervisor and mentor over the last two years. Not only for all of the lessons in programming, data analysis, physics of the ISM, and the countless other topics needed to complete this thesis, but also for exercising a lot of patience dealing with my seemingly endless questions, concerns, and bugs in my code. I also appreciate the many words of wisdom I can take with me on the journey forward, such as "Never underestimate the power of a three-color image. Or the Force".

From a research point of view, thank you to Tomas Robinson for supplying the catalogue of Bolocam peaks that came in handy during this research process, and Chris Brunt of Exeter University for supplying the CO (1-0) datasets. I would like to thank the staff of the Joint Astronomy Centre for their support during my visit to JCMT including Ian Coulson, Jan Wouterloot, and especially Jim Hoge who is both an amazing observer and human being in general.

This research made use of Observations from the James Clerk Maxwell Telescope. The James Clerk Maxwell Telescope has historically been operated by the Joint Astronomy Centre on behalf of the Science and Technology Facilities Council of the United Kingdom, the National Research Council of Canada and

the Netherlands Organisation for Scientific Research.

A special thanks to the volunteers and crew of the U of A Observatory for all of the fun nights spent trying to find faint but fantastic objects in a light polluted sky! I would like to thank Sharon and Greg for the opportunity to be a part of the observatory team as a TA. Also thank you to Robin, Khaled, Arash, Tomas, Steffan, Colin, Clayton, Jeanette, Charles, and Khilesh, among many other observatory staff and volunteers.

I would also like to thank my officemates Arash, Robin, Eric, and Erica for putting up with me over the last couple years, and in particular Arash for always being extremely helpful. Also for the constant supply of cookies and jokes (often aimed at me) when I needed them. Thank you to the other members of the Astro group including Dario, Veselina, Eric, and Alice for their support and research advice. Thank you to Khaled for supplying coffee on a regular basis and not complaining when I booked 8 months worth of early morning school group visits to the observatory.

Thank you to my family and friends for the support over the years, namely my parents Ingrid and Rick and brother Jarred. To my friends in Edmonton, Julia and Kalista for the emotional support, along with my D&D group members: Cameron, Anna, Brendan, and Kyle. A special thank you to my boyfriend Kyle for putting up with me during the many panic filled moments of my degree. Most of which occurred in the last few months.

Contents

1 Introduction **1**

1.1 Dynamical Properties of Star Formation 3

1.1.1 Turbulence 4

1.1.2 Magnetic Fields 4

1.1.3 Radiation Field 5

1.2 Stages of Star Formation 5

1.2.1 Early Stages of Star Formation 5

1.2.2 Later Stages of Star Formation 7

1.3 Galaxy-scale Star Formation 8

1.4 Local Neighborhood Star Formation 10

1.5 This Work 14

2 Molecular Line Emission and Excitation Conditions **16**

2.1 Carbon Monoxide Lines 18

2.1.1 Isotopologues of CO 19

2.1.2 Light from Molecules 20

2.1.3 Radiative Transfer 24

2.1.4 Non-LTE Models 26

2.2 Observer Conventions 28

2.2.1 Single Line Spectra 28

2.2.2 Moment Analysis 28

2.2.3 Description of Temperatures 30

3 Low Surface Brightness Gas **31**

3.1 Cygnus X Star Forming Region 31

3.1.1 Cygnus X Raster Map 35

3.2 W80 35

3.2.1 W80 Raster Map 38

3.2.2 Mosaics 47

3.2.3 Integrated Velocity Maps 47

3.2.4 Moment Maps 48

3.2.5 Outflows 51

3.3 Brightness Distribution Function and Cloud Identification . . . 51

3.4 Locating Low Surface Brightness Gas 62

4 Physical Conditions of Low Surface Brightness Gas **66**

4.1 Cygnus X Dense Gas Tracers 67

4.1.1 Data Processing and Reduction 70

4.1.2 CO(1-0) Data 72

4.1.3 Gaussian Modelling 72

4.1.4 Spectrum Extraction 72

4.1.5 Models of CO Emission Lines 74

4.1.6 RADEX Parameter Grids 75

4.1.7 Bayesian MCMC with emcee and RADEX 76

4.2 Line Fitting 79

4.2.1 Mass Determination 85

4.2.2 Conversion Factor 89

5 The Contribution of the Faint Gas Component to the Star Formation Law **91**

5.1 Extragalactic Star Formation Rate 92

5.2 Galactic Star Formation Rate 94

5.2.1 Cygnus X 95

5.2.2 W80 96
5.3 Comparing Tracers of Star Formation for Bright and Faint Gas . 99
5.3.1 Effects of Sampling 102
5.4 Discussion of Star Formation Rates 104

6 Summary and Conclusion **110**
6.1 Further Work 113

A Description of Packages **120**
A.1 Python 120
A.2 Starlink 121

B Spectral Fits **122**

List of Tables

3.1 HARP/ACSIS Observation Parameters 40

4.1 ^{13}CO/C^{18}O HARP/ACSIS Observation Parameters 71
4.2 Grid Parameters 76
4.3 Total Mass of Cygnus X Molecular Clouds 88
4.4 Total Mass of W80 Molecular Clouds 89

List of Figures

1.1 Hubble image, HII region 6
1.2 Stages of star formation 8
1.3 Star formation rate from Leroy et al. 2013 12
1.4 Gould Belt star formation rate 13

2.1 Gas velocities and spectral lines 29

3.1 Cygnus X and the Gould belt in the Milky Way 32
3.2 Cygnus X at submillimetre, radio, infrared frequencies 36
3.3 Observational scan pattern 40
3.4 W80 and Cygnus X observed regions 41
3.5 Fourier cleaning algorithm 46
3.6 W80 moment maps 48
3.7 W80 literature dust and IR sources 49
3.8 W80 multiwavelength observations with molecular contours . . . 52
3.9 W80 location of molecular outflows 53
3.10 W80 Bright and faint gas 56
3.11 Image processing with morphology 58
3.12 Brightness distribution functions of negative velocity gas 59
3.13 Brightness distribution functions of positive velocity gas 60
3.14 Brightness distribution functions of faint gas 61
3.15 Cygnus X bright and faint gas 63
3.16 Brightness Distribution function of W80 clouds 64

4.1 JCMT HARP 4×4 grid of receivers. The on-sky projected beam separation is 30″, with a 15″ beamwidth. 68
4.2 Clouds observed with dense gas tracers 70
4.3 Sample CO(3-2) and CO(1-0) spectrum 73
4.4 Sample spectrum fit with model 81
4.5 Sample Markov chain for fit parameters 82
4.6 Plots of model parameters for all lines 83
4.7 Parameter plots after filtering out poor fits 84
4.8 Cygnus X bright gas surface density images 87
4.9 Cygnus X faint gas surface density image 88
4.10 X_{CO} in Cygnus X 90

5.1 Cygnus X H_α and 24 μm MIPS cutouts 93
5.2 Integrated intensity maps of Cygnus X showing associated YSOs 97
5.3 Integrated intensity maps of Cygnus X showing associated YSOs 98
5.4 Distribution of W80 YSOs 99
5.5 W80 YSOs associated with clouds 100
5.6 W80 YSOs associated with clouds 101
5.7 Star formation rate from Galactic and extragalactic tracers . . . 103
5.8 Comparison of Galactic and extragalactic star formation tracers for Cygnus X. 104
5.9 Extragalactic SFR using different sampling areas 105
5.10 Extragalactic SFR using different sampling areas with X_{CO} as a mass tracer 106
5.11 Galactic SFR using different sampling areas 107
5.12 Galactic SFR using different sampling areas with X_{CO} as a mass tracer 108

Chapter 1

Introduction

The process of star formation in galaxies is a continuous process, fuelling the evolution of all galaxies. Star formation sets the stellar content of galaxies, and therefore the history of star formation determines the light that we see from even the most distant galaxies. Through gas processing, star formation leads to the enrichment of the interstellar gas with metals (all elements on the periodic table with atomic number greater than helium). The fact that the star formation process appears similar from the earliest galaxies to today indicates that this universal process is key to our understanding of all aspects of astronomy.

Galaxies like the Milky Way are made up of a mixture of dust, stars, atomic, and molecular gas, where stars are formed within the molecular gas component. Molecular gas in galaxies is typically grouped into Giant Molecular Clouds that have sizes of 25−200 pc[1] [18]. Most of the molecular gas in the Milky Way exists between 4 and 8 kpc from the Galactic centre in a region known as the Molecular ring [71]. In every galaxy that we observe, areas of molecular gas indicate areas of star formation, and therefore the understanding of the physics of molecular clouds is key to the whole star formation process.

The properties of molecular clouds vary depending on the scale being dis-

[1] 1 parsec (pc) = 3.086×10^{16}m

cussed, as molecular clouds can range in size from Giant Molecular Cloud (GMC) complexes of sizes 25−200 pc, to dark clouds of 0.3−6 pc in size, to molecular cores with sizes of 0.1 pc that form individual stellar systems [18]. The interstellar medium is defined by the chemical state of its dominant component hydrogen: ionized, atomic, or molecular. Atomic gas exists at temperatures of between 100 K and 5000 K, and molecular gas is much colder, usually $\sim$10 K with densities of $10^3 - 10^4$ particles per cm^3. Large GMC complexes can have masses of $10^5 - 10^6$ M$_\odot$[2] [18]. Properties of clouds vary over the course of their lifetime and can depend on whether the cloud is forming lower mass or higher mass stars [31]. The coldest regions of molecular gas are dense cores, the sites of individual star formation and collapse.

The most common species is H_2 with the next being He. But within regions of molecular clouds where densities and low kinetic temperatures shield molecules from ionizing radiation and dissociation, we see the formation of many molecules including carbon monoxide (CO), ammonia (NH_3), and water (H_2O), among hundreds. Different molecules require different physical conditions to form. For example, CO is formed easily, and therefore is ubiquitous in molecular clouds. Complex hydrocarbons are more volatile, and more readily destroyed by radiation, and therefore only exists in the densest, coldest regions of molecular clouds where molecules are shielded from radiation by other molecules [77]. Therefore the detection of these molecules would indicate the presence of dense cores, which are likely to form stars, whereas detection of carbon monoxide indicates the presence of molecular gas in general, from Giant Molecular Cloud complexes to individual bright star forming regions. Even though H_2 is the most common molecule in the universe, it is largely invisible to observers (discussed in Chapter 2). But since the conditions necessary to produce H_2 are also required to produce other molecules like CO, we use molecules other than H_2 as tracers for the whole molecular gas component. In-

[2] 1 solar mass, M$_\odot = 1.989 \times 10^{30}$ kg.

teractions with hydrogen both in gas phase, and on the surfaces of dust grains is the major method of producing most molecules we find as well [77].

1.1 Dynamical Properties of Star Formation

Stars form when a molecular cloud collapses under its own gravity. Regions of molecular gas exist in a careful balance of internal pressure driving the cloud apart, the force of gravity holding the gas in place, and often external pressure from the surrounding medium. This relationship is described using the virial theorem, by which the gravitational energy is balanced by pressure forces, kinetic energy of the gas, and magnetic fields (e.g., in [73]). From this relationship comes a critical mass and length scale defining the conditions for the onset of collapse, known as the Jeans mass and Jeans length. Molecular clouds with radii less than the Jeans length (Equation 1.1; [73]), or with masses greater than the Jeans mass (Equation 1.2; [73]) will begin to collapse under their own gravity. These expressions depend on the densities and temperatures of a region. Using typical temperatures of molecular gas ($n_{H_2} \sim 10^4$ cm^{-3} and $T \sim 10\ K$) we see a critical mass of 1 M$_\odot$ and a critical length of 0.19 parsec. This is about the mass and length scale observed for molecular cores.

$$\lambda_J = 0.19 \text{ pc} \left(\frac{T}{10 \text{ K}}\right)^{1/2} \left(\frac{n_{H_2}}{10^4 \text{ cm}^{-3}}\right)^{-1/2} \tag{1.1}$$

$$M_J = 1.0 \text{ M}_\odot \left(\frac{T}{10 \text{ K}}\right)^{3/2} \left(\frac{n_{H_2}}{10^4 \text{ cm}^{-3}}\right)^{-1/2} \tag{1.2}$$

Other factors such as turbulence, magnetic fields, chemical composition, and radiation are thought to be important in core stability, but are neglected in this simple analysis.

1.1.1 Turbulence

If the collapse of a clump or core in a molecular cloud depended on the force of gravity alone, star formation would be much more efficient than we observe currently. Scale dependence makes turbulence important [49]. Although the term turbulence may bring to mind unstructured disturbances to the gas within a molecular cloud, turbulence has clear correlations that relate large and small scales. Its influence on molecular clouds and their collapse is therefore an increasingly well studied topic. Turbulent motions work to support a cloud against gravitational collapse, and for scales greater than 0.1 pc, turbulence becomes a driving factor in the density structure of a cloud [49]. Turbulence also controls the line width of emission from molecular clouds. Three dimensional simulations of turbulence in magnetized and unmagnetized media also show a correlation between density differences and turbulence. This is often parameterized by the Mach number, or the ratio of the speed of a disturbance to the isothermal sound speed in the medium. A relationship exists between the size and the line width observed for a molecular cloud [40], which is predicted by models of turbulence [52].

1.1.2 Magnetic Fields

Magnetic pressure within a clump can halt further collapse of a molecular cloud. The effect of the ambient magnetic field on cloud structure is dictated by the magnetic critical mass, which is the mass at which magnetic energy balances out gravitational energy, thus preventing further collapse of the cloud. Masses greater than this value will continue to collapse and are referred to as magnetically supercritical clouds [18]. For clouds with densities of 10^4 cm^{-3}, the typical magnetic field strength is around 50μG [12]. The dependence of core collapse on magnetic fields also depends on collisionality, resistivity, and magnetic field diffusion in the cloud.

1.1.3 Radiation Field

The ambient radiation field also plays a large factor in the properties of molecular clouds and whether or not they are susceptible to gravitational collapse. Ultraviolet radiation from young stars within a parent molecular cloud slowly erodes away the cloud through photodissociation. The dissociation and ionization of the gas of a molecular cloud produces bright cavities of hot gas that we see as photodissociation regions (PDRs), and HII[3] regions. HII regions are the most common direct tracer of star formation, and radiate in optical light (see Figure 1.1).

1.2 Stages of Star Formation

1.2.1 Early Stages of Star Formation

The earliest stage of star formation begins with the formation of molecular filaments. Fluid and turbulent motions within Giant Molecular Clouds produce filamentary structures that run across observations of star forming regions. Within the densest filaments, there is evidence for fragmentation. These fragments then continue on to form prestellar cores and later protostars [2]. Filaments vary in size from less than 0.1 pc to more than 10 pc and are largely isothermal. They seem to be formed by large scale processes in molecular clouds and have been linked to turbulent motion. Filamentary structures act as "hubs" for star formation [51] and enhanced star formation and early cluster formation is seen at the intersection between multiple filaments. As quiescent or non star-forming filamentary structures are seen, filaments appear to be precursors to clump and core formation in molecular gas [2].

[3]HII is spectroscopic shorthand for ionized hydrogen.

Figure 1.1: Hubble Space Telescope image of the Monkey Head Nebula, showing the edge of the ionization front formed from newly formed high mass stars. There is a clear divide between the hot ionized gas or HII (blue) and cold molecular gas (red) in the image. Credit: NASA, ESA, Hubble Heritage Team `http://www.nasa.gov/sites/default/files/14-076-hubble-anniversary3_0.jpg`

1.2.2 Later Stages of Star Formation

The later stages of star formation occur at small scales, on the order of the size of individual young stellar objects (YSOs). In Figure 1.2, we can see that the collapse and formation of a star occurs in four main stages. Initially a star begins as a prestellar core, which has a fairly uniform density throughout [3]. After it starts to collapse, the core develops a central peak that continues to accrete material from the surrounding envelope. The transition from a uniform dense clump to a Class 0/I YSO with a central protostar and disk occurs over 1 Myr. In its prestellar core stage, most of the mass still exists in the envelope of the clump and not in the central YSO. By the Class 0/I stage, much more material has accreted onto the central YSO from the surrounding envelope, and by the Class II stage the envelope is gone and all of the material has accreted onto the YSO and disk surrounding it [31]. During the Class 0-II stages, YSOs also show signs of bipolar outflows or jets, which are detectable when studying molecular gas or dust. A star spends around 0.5 Myr in Class 0/I stage, and 1.5 Myr in its Class II stage [24]. A star can remain in its Class III phase much longer, up to 10 Myr and by the end of which it is fully evolved and fusing hydrogen. Tracers of each stage of star formation vary. Very young YSOs in their Class 0 and I stages are still deeply embedded in their parent molecular cloud. Due to the cold temperatures and high densities, these are best detected in submillimetre and far-infrared light. Class II and III YSOs have accreted most of their surrounding envelope meaning it is possible to view these stars in shorter wavelengths of near-infrared and optical light as they are no longer completely obscured from view [18]. For high mass stars, their strong winds and UV radiation clear out a cavity surrounding them of hot ionized material, visible in optical light (see Figure 1.1).

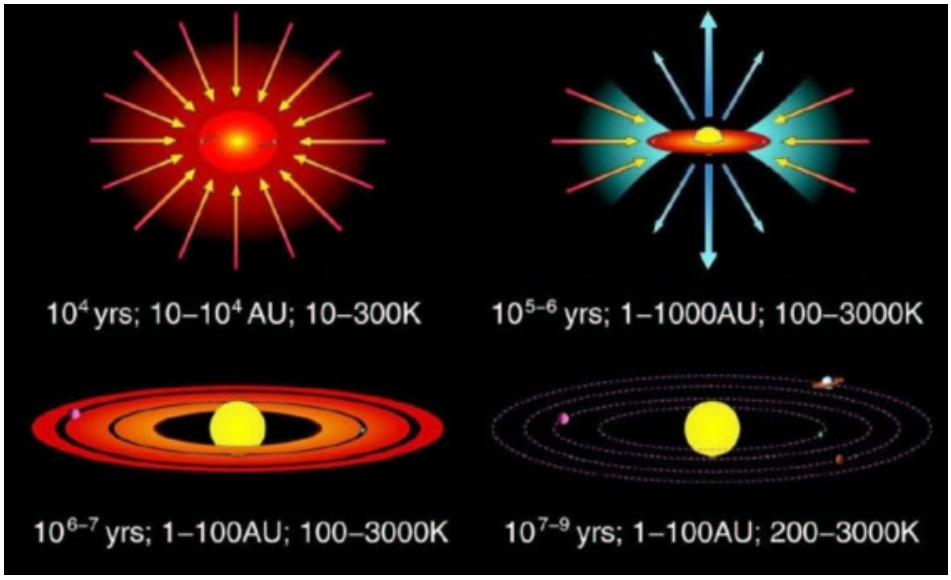

Figure 1.2: Evolution of a star from prestellar core (top left) to Class 0/I YSO (top right) to Class III YSO (bottom left), and finally a fully evolved star and planetary system (bottom right). Class II sources are not shown on this illustration, they have a much thicker disk than Class III sources and no envelope.

1.3 Galaxy-scale Star Formation

Despite the complexity of the individual star formation events, the measurements of star formation on galaxy scales is not only possible, but straight forward and surprisingly uniform across any galaxy. By averaging measurements over large regions, the complexities present on smaller scales appear to be averaged out. Densities within individual molecular clouds may vary wildly, but in distant galaxies where individual molecular cloud regions and filaments are not resolved, we notice that the overall properties show the same uniform correlation from galaxy to galaxy. We focus on is the Schmidt relation [65], which is a power law relation between physical parameters of gas. These physical parameters are derived from the assumed relationship between star formation and gas depletion. This relationship was advanced when studies of many galaxies of the local universe and indicated that this powerlaw relation is universal with an index of 1.4 ± 0.15 [32]. This is referred to as the Kennicutt-Schmidt law (KS

law). The fact that this relationship exists even in galaxies from their earliest to the latest stages tells us that star formation is a constant, ongoing process in the Universe. Relationships are seen between various stages in the star formation process. For instance there is a relation between the stellar initial mass function (IMF) and the distribution of cores. The initial mass function is the distribution that describes the number of stars in different mass bins; the IMF follows a powerlaw or broken powerlaw shape showing that low mass stars are much more common than high mass stars. We would expect that the distribution of clump masses match the distribution of star masses [31], and there is a closer relationship between the IMF of stars and the IMF of clumps than there is between the IMF of stars and the IMF of clouds. Stellar and cluster IMFs ([62]; [35]; [9] for stars, [38] for clusters) are typically steeper with much more of the mass residing in lower mass stars. The IMF of clouds [58] shows that even though small molecular clouds are more common, most of the mass exists in large molecular cloud complexes. This is further evidence that cores are precursors to stars.

The simplicity of this relation is that it says more gas leads to more star formation, and no matter where you look in the galaxy stars are produced from gas with the same efficiency [44]. However, this scaling relationship shows some dependency on the environment and tracer observed, suggesting the picture is more complicated [31]. Examining the total gas component results in a relationship with greater scatter than the observation of molecular gas alone. Merger-induced starburst galaxies show a variation in this nonlinear relation [44], and examining the relation on smaller scales instead of averaging over the disk of a galaxy can affect the universality of this relation further.

The fact that young stellar objects (YSOs) exist within dense regions of gas and dust often prevents us from observing them directly, especially in other galaxies. We therefore look to other methods that trace their formation. HII regions are the ionized regions around high mass star forming regions. The

ionizing photons from HII regions can be detected through H_α[4] emission [31] even at large distances. Observations of SFRs using high mass tracers like HII region observations then depends upon the stellar IMF. When comparing observations of ionizing photons to the modelled stellar IMFs, we see that only the upper tail is being sampled. Most extragalactic calculations of SFR depend upon the assumption that over large, unresolved scales, differences in the IMF population will be averaged out. However, resolved studies of molecular clouds using high mass tracers such as H_α may cause an underestimate of star formation rate. This is discussed at length in [31], where they compare the situation to what observers in another galaxy would measure for star formation around the Sun. Using high mass tracers, these observers would only detect the nearby HII regions of the Orion nebula, and would not observe the dense regions of low mass star formation nearby. The assumptions based on IMF would lead to the conclusion that the SFR is a factor of 8 smaller than the true SFR ([37]; [31]).

The assumption would naturally be that the KS law pertains to our own galaxy as well, down to the scale of individual star forming complexes, but this is not what we see.

1.4 Local Neighborhood Star Formation

A study by [44] looked to identify any possible variation from the KS law in nearby galaxies as a result of the star formation tracer used, or the type of gas surveyed. The authors explored the possibility that variations come from differences in method used to measure star forming surface density and the surface density of molecular gas, along with possible differences in conversion factors or galaxy properties. Measurements were obtained from regions of nearby galaxies using multiple tracers (see Figure 1.3). The authors determine that molecu-

[4]Balmer $n = 3$ to $n = 2$ transition.

lar gas provides the best tracer for star formation rather than the combined molecular and atomic mass. They concluded that the efficiency of star formation varies slightly from region to region, but overall follows a powerlaw relation with an index of 1.

In our own neighbourhood, we see star formation occurring in clouds all around us known as the Gould Belt, a region of stars and clouds less than 600 pc from our own solar system, (see Figure location Chap 2). Due to its proximity, the star formation rate can be calculated directly by counting the number of YSOs of different classes and dividing by their mean lifetime (see Figure 1.2). A study of star formation in the Gould belt clouds showed that star formation in the local clouds of the Gould belt are more efficient at forming stars than its extragalactic counterparts by a factor of 10 (see Figure 1.4) [28].

There are a few possible solutions to this problem, some more likely than others. It is possible that there is a problem with the IMF; however this is well modelled and known (see references in above discussion of stellar IMF) and therefore highly unlikely to be the problem. Problems with the IMF are also something that can be directly compared with stars we see in our own galaxy of all masses. Another possible explanation could be that the Gould belt is an atypical star forming region. There have yet to be large extensive studies of other regions of star formation in our galaxy that more closely resemble the star forming regions we see in other galaxies. It could also be that all of the gas is not being accounted for. We have discussed the diffuse molecular component, and previously this was thought to be a small amount of the mass of the Galaxy. However, the results show that it could be a larger portion of the gas than previously thought [64]. The possibility exists that the difference in star formation efficiency of local clouds arises due to differences in density [39]. Dense gas traces star formation, and therefore the correlation between star formation rate and gas is strongest for dense gas. The fact that the Kennicutt-Schmidt law is independent of galaxy type suggests that something may still

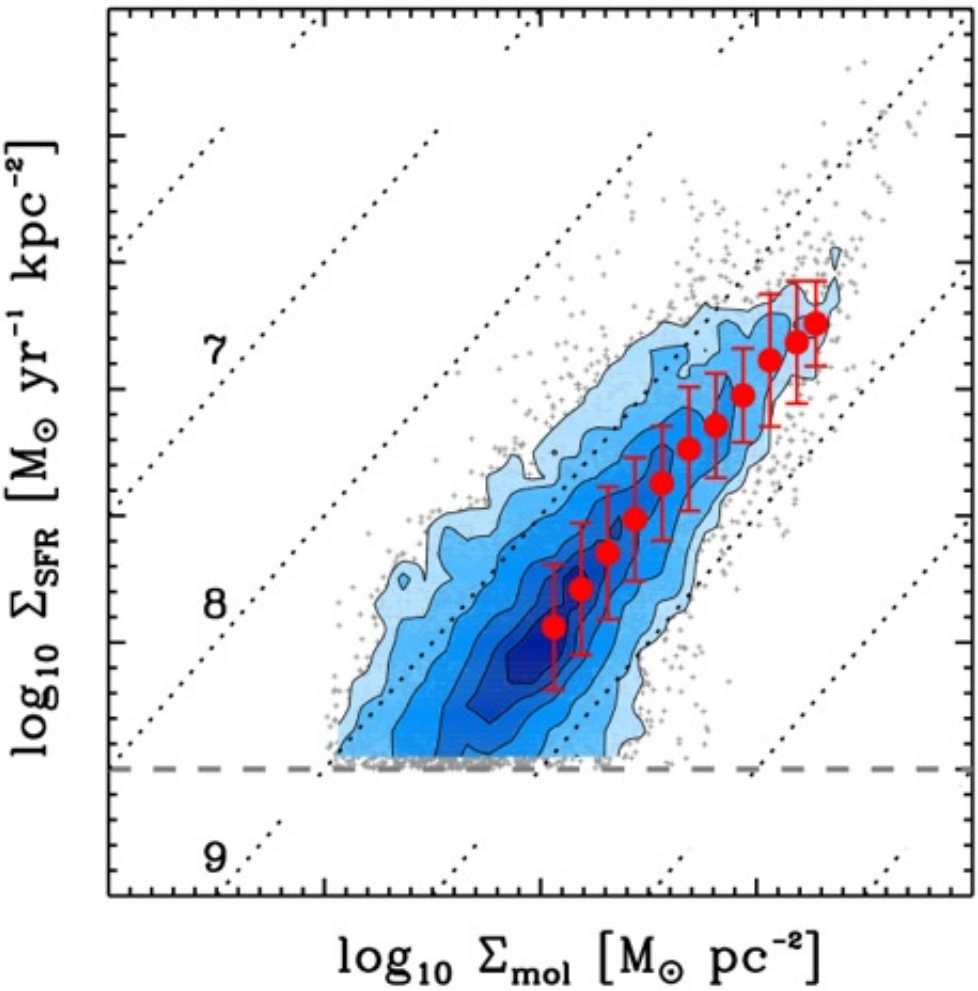

Figure 1.3: Figure 4 from [44] showing the star formation rate as a function of the molecular gas mass sampled using multiple tracers and different regions. This shows a linear relationship between SFR and the surface density of molecular gas that is independent of tracer or region studied. © AAS. Reproduced with permission.

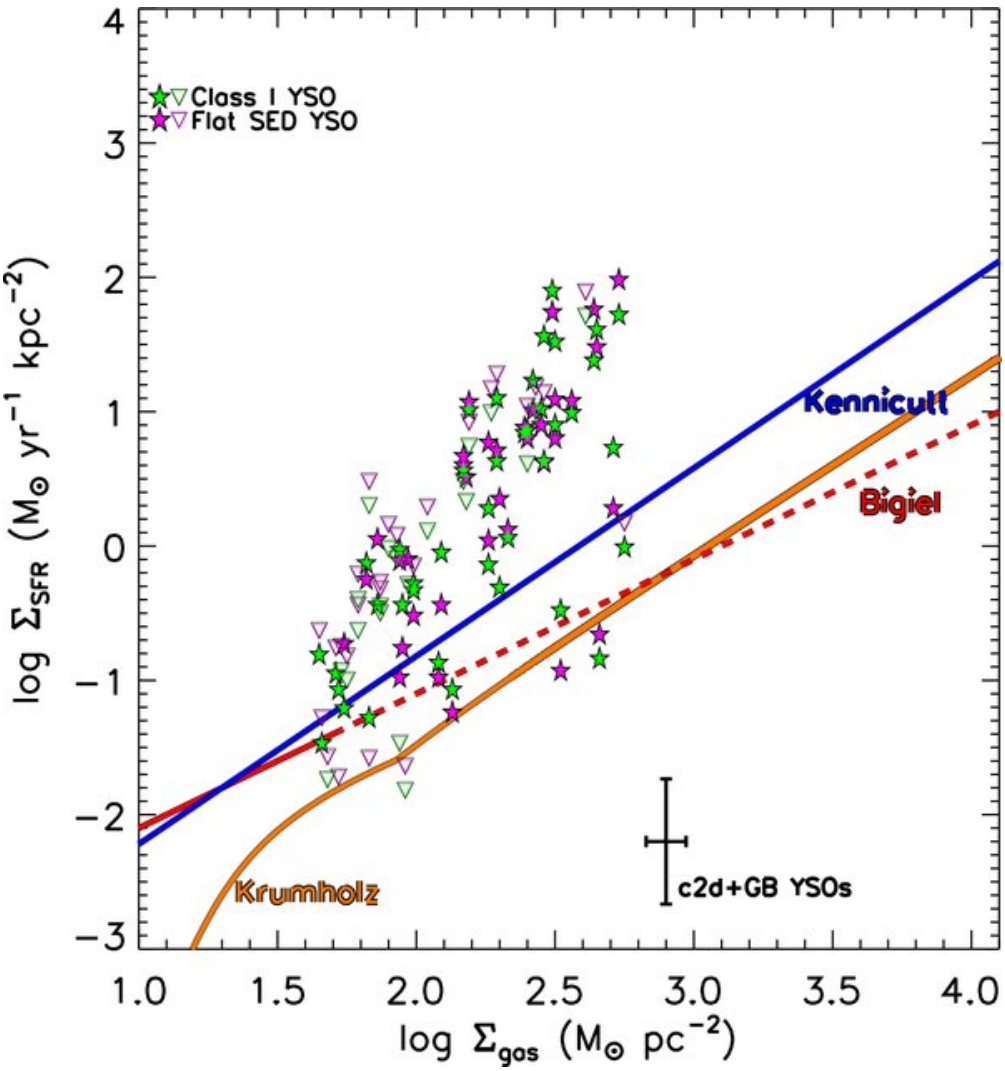

Figure 1.4: Figure 3 from [28] showing the star formation rate for the local clouds of the Gould belt compared with extragalactic relations. © AAS. Reproduced with permission.

be missing from measurements of local star forming efficiency. It could also be a discrepancy in the star formation tracers used. This is thought to be unlikely [44], but even if unlikely it could still be a contributing factor. What is needed to make progress in this discussion is a study of another region in the Galaxy that resembles those we identify in other galaxies.

1.5 This Work

The Cygnus X star forming region is a well studied region of the Milky Way galaxy. It is a very active region of both high and low mass star formation, making it an ideal region of the sky to study the physical conditions necessary for all types of star formation. In 2012, a pathfinder survey of the Cygnus X region revealed the presence of diffuse low surface brightness gas in the foreground of the star forming complex, believed to be associated with it [23]. The Cygnus X star forming complex has many bright HII regions alongside large OB associations, making it an ideal analog for the star forming regions studied in other galaxies. The presence of Galactic and extragalactic star forming tracers allows us to calculate a rate of star formation that is unbiased to the type of tracer used. In addition the presence of both a bright star forming component and diffuse (seemingly quiescent) gas component makes it an ideal laboratory to test the hypothesis that the inclusion of this faint gas would correct the higher efficiencies detected in Milky Way clouds compared to the efficiencies we detect in other galaxies of the Local Group. The properties of the diffuse component of molecular gas are not well known, so I take the opportunity to identify any differences in physical characteristics of the diffuse Galactic clouds and the typical star forming clouds resolved in nearby galaxies.

In my analysis, I use molecular line data and star formation rate data to study the efficiency of star formation in the Cygnus X region of the Galaxy to see if the low surface brightness quiescent clouds contribute to the calculation

of mass, thus lowering the star forming efficiency for local clouds. I also explore the possibility that the choice of SFR tracer contributes to the high star formation rate by using both Galactic and extragalactic SFR tracers. Furthermore, I look at possible methods for identifying diffuse cloud structures in datasets of molecular gas, including the probability distribution of brightness temperature of clouds. The primary focus of this work is on the Cygnus X region, for which I calibrate my method of faint cloud identification and explore extragalactic and Galactic methods of determining star formation efficiency. I then apply my method to observations of the W80 region, which has evidence of similar faint gas. I also produce the first high-resolution large scale molecular gas observations of the W80 region.

This thesis is structured as follows. In Chapter 2 I discuss carbon monoxide line emission and set up the formalism for the model of molecular gas emission lines. In Chapter 3 I discuss low surface brightness gas and my method for identifying these clouds in data. I also discuss the data reduction and raster map production for both the Cygnus X and W80 regions, and give an overview of the literature for both regions. In Chapter 4 I discuss the spectral fitting of molecular cloud emission lines for bright and low surface brightness clouds, and what we can infer about their physical properties as a result. Lastly, I present the SFRs and molecular gas surface densities of Cygnus X and W80 determined using Galactic and extragalactic tracers, and compare my results to those of [44] and [32].

Chapter 2

Molecular Line Emission and Excitation Conditions

To test the hypothesis that low surface brightness (LSB) clouds drive the discrepancy between Galactic and extragalactic star formation laws, I measure the physical conditions in the LSB gas. We observe the resolved molecular clouds in the Cygnus X region and determine the molecular gas mass using the rotational emission lines of the CO molecule, which will be discussed in this chapter. Detailed descriptions of the observations used along with the steps involved in the data reduction process are included in Chapter 3[1]. CO is the most commonly used tracer of Galactic and extragalactic molecular gas mass. Recently, observers have also focussed on observations of thermal emission from dust, which traces both the atomic and molecular gas component. The primary focus of this thesis is the processing and analysis of CO emission in the two regions of interest, Cygnus X and W80, and the comparison of using extragalactic and Galactic tracers of star formation. Details of the CO line model and physical parameters of interest are discussed in Section 2.1. We fit this model of CO emission to the data using a Bayesian method with a Markov-chain Monte-Carlo implementation (MCMC), and the theory is discussed in

[1]Here I outline how rotational lines provide diagnostics of molecular cloud conditions.

Chapter 4. For the observations of star formation rate, I rely on both common extragalactic tracers, and Galactic SFR tracers to explore whether the star formation efficiency is biased by the choice of tracer used. We use both publicly available and processed data for the star formation rate, and therefore the primary focus of this work is in the reduction, processing, and analysis of the molecular line data that has been obtained.

The analysis includes the production of large raster scan maps of the W80 region, seen for the first time in high-resolution molecular line emission. The Cygnus X region maps were processed as a part of the same observing project by [23]. In addition, I acquired further pointed observations using dense gas tracers in the submillimetre band. The raster maps of both the Cygnus X and W80 region show emission from the ^{12}CO molecule, as ^{12}CO is the most abundant isotopomer of CO and the second most common molecule species in the interstellar medium (ISM). It is therefore bright and can be observed quickly enabling production of large scale region maps. The large maps allow us to identify large scale molecular cloud structures both through algorithmic analysis, and through by-eye examination of the data. We then observe select lines of sight using emission lines from rarer isotopologues of CO, ^{13}CO and C^{18}O. As these emission lines are much fainter and require longer integration times, I observe a select few clouds for long periods instead of mapping the whole region to guarantee the detections of faint lines. We also have access to lower energy CO(1-0) line data[2]. Although these data have lower resolution than our CO(3-2) line data, the CO(1-0) line transition provides essential constraints in our model.

[2]Numbers in parentheses represent transition lines within the molecule. 1-0 indicated emission from the transition of a molecule from the first excited state to the ground state.

2.1 Carbon Monoxide Lines

Molecular hydrogen is the most abundant molecule in our universe. In spite of its abundance, detecting H_2 has always been a great challenge in astronomy. The main reason for this difficulty is that H_2 is a homonuclear molecule, and thus has no electric dipole moment [18]. Molecular hydrogen has zero net orbital angular momentum, zero electron spin, and is symmetric under refection. The lowest electronic energy levels correspond to its quadrupole moment, which requires far infrared and shorter wavelengths to excite. Transitions between ortho- and para-hydrogen molecules (the hydrogen spin isomers) require temperatures of 510 or 1015 K to excite a transition, and the lowest vibrational energy levels of hydrogen require gas temperatures of over 6000 K [7]. Given the temperatures of molecular clouds are less than 100 K with dense star forming regions typically less than 10 K above the cosmic microwave background, there is no way to excite the molecular hydrogen in a typical dense cloud. Helium gas is also invisible for similar reasons. Therefore studies of H_2 require a tracer such as other molecules (CO) or dust. We know that some other molecules form under the same conditions as H_2. Dust is pervasive in molecular clouds and dust mass can be converted to total gas mass through the well known dust to gas ratio seen in both atomic and molecular clouds [7]. Dust absorbs and reddens light from background stars, and thus allows the calculation of gas mass through extinction in optical and infrared bands. We also see thermal radiation from dust at the typical 10 K temperatures of molecular clouds, which is visible in infrared and submillimetre. In addition, astronomers observe emission through the vibrational levels of polycyclic aromatic hydrocarbon particles which radiate at wavelengths less than 50 microns [18].[3] The limitation is that extinction studies are only a viable option for studying molecular gas in local clouds, and therefore we rely on molecular line tracers for extragalactic studies.

[3]Extinction is the process of absorption and scattering of light from a source by dust. Blue light is preferentially absorbed and scattered, leading to 'reddening' of light from stars.

By far the most widespread method of studying molecular gas is through the radio and millimetre emission lines of the most abundant species after H_2, CO. With a weak dipole moment, CO has low lying energy levels that are easily excited at the low temperatures in molecular clouds [18]. These are excited through collisions with H_2, and therefore CO is sensitive to density [7]. Many studies of the mass of molecular clouds use a direct comparison between the total integrated intensity of the ^{12}CO $(1-0)$ line and molecular hydrogen column density. This value is known as $X_{\rm CO}$ or the CO-to-H_2 conversion factor. The power of this relation is that any CO emission, even that of unresolved clouds in distant galaxies can be converted into a mass of molecular material following Equation 2.1[4] [7]:

$$\mathrm{N_{H_2}(cm^{-2})} \;=\; \mathrm{X_{CO}\ W_{CO}} \tag{2.1}$$

For our own galaxy, the standard value is $X_{\rm CO} = 2 \times 10^{20}$ cm^{-2}(K km s^{-1})$^{-1}$. The origin of this relation comes from a study of the population of rotational lines of the CO molecule. I will measure X_{CO} for the Cygnus X region in Chapter 5.

2.1.1 Isotopologues of CO

Different isotopologues of carbon monoxide are excited under different physical conditions. ^{12}CO is the most abundant, therefore emission from low-J levels of the molecule are easily detectable from all molecular clouds, even at low densities. ^{12}CO is used as a mass tracer in extragalactic studies as it can be assumed that all molecular gas is being detected. The abundance of ^{12}CO compared to H_2 is 2×10^{-4} [6]. ^{13}CO is 65 times less abundant than ^{12}CO, and

[4] $W_{\rm CO}$ is the integrated intensity with equation $W_{\rm CO} = \Delta v \sum T$ where v is the velocity width of a channel and T is the main beam temperature. $N_{\rm H_2}$ has units of cm^{-2}, and represents the number of particles in a cm^2 column through the medium. This is referred to as the column density.

$C^{18}O$ is even less abundant with a $^{12}CO/C^{18}O$ fraction of 5.0×10^2 [6]. The less abundant isotopologues of ^{13}CO and $C^{18}O$ are thus found in denser molecular gas. The downside to using ^{12}CO alone for determining mass is that the high density of ^{12}CO often means emission lines are optically thick through a process known as radiative trapping. Radiation produced from one ^{12}CO molecule likely will not escape the cloud before being reabsorbed. Therefore not all emission escapes the cloud, and a measurement of intensity is not an accurate measurement of the amount of material within the cloud. The frequently used analogy is trying to study the density of a building by observing one wall. You cannot see through the wall and so can only assume the amount of material from the size of the one wall. ^{13}CO and $C^{18}O$ suffer from this problem less. Their optically thinner lines mean that emission is proportional to the density of molecules since most photons escape the cloud. Knowledge of a regions physical conditions is then determined by combining models of both ^{12}CO and a dense gas isotopologue. Optically thick ^{12}CO radiation bands can be used to infer temperature, and line radiation from ^{13}CO or $C^{18}O$ can be used to infer how much gas is there.

2.1.2 Light from Molecules

A full discussion on the derivation of physical parameters is given in [47]. I will give a summary of the concepts important to this work. Transitions between energy levels of a molecule occur in one of three ways. Electronic transitions near the ground state have energies on the order of 1 eV and are detected in optical and UV bands. Vibrational transitions from the stretching of molecules have energies on the order of $10^{-1} - 10^{-2}$ eV and are detected in infrared light; rotational transitions have energies on the order of 10^{-3} eV and are detected in centimetre/millimetre bands [7]. Hyperfine splitting of energy levels are the result of interactions between the nuclear and electron spins of a molecule and are visible in radio at energies of 10^{-6} eV [18].

We rely on rotational transitions of CO to trace molecules. Rotational transitions are the result of fine structure splitting of a molecule's energy levels due to the interaction of the molecule's dipole moment with the ambient radiation field [18]. It is the transition between these lines that are possible within the cold gas of molecular clouds because $kT \sim 10^{-3}$ eV at 10 K. The rotational energy of the molecule depends upon the total angular momentum quantum number J (Equation 2.2) [18],

$$\mathrm{E_{rot}} = \frac{\hbar^2}{2\mathrm{I}}\mathrm{J(J+1)} - \mathrm{D[J(J+1)]^2} \tag{2.2}$$

where I is the moment of inertia of the molecule and D is the constant for centrifugal stretching. For linear diatomic molecules, the rigid rotor assumption represented by the first term of Equation 2.2 is sufficient for low J.

With that in mind, the population of states within a parcel of gas exchanging energy with its environment can be described using the partition function as described in [47],

$$\mathrm{Q_{rot}} \approx \sum_J (2\mathrm{J}+1)\exp\left(-\mathrm{B}\frac{\mathrm{J(J+1)}}{\mathrm{kT}}\right) \tag{2.3}$$

$$\tag{2.4}$$

Where $\mathrm{B} = \frac{\hbar^2}{4\pi\mathrm{I}}$.

The intensity of a ΔJ transition line relies on the energy levels of a molecule existing in a state of statistical equilibrium in that all transitions to a level are balanced by all transitions out of it. This is known as detailed balance, and allows for the calculation of the population of a given state. Transitions between energy levels are described in terms of Einstein coefficients A, B, and C, which are the probability of a molecular transition from state i to j through spontaneous, stimulated, or collisional means respectively.

Transitions between levels can occur through spontaneous emission de-

scribed by the probability of this transition, Einstein coefficient A_{ij} [5] with units s^{-1}. Stimulated excitation or deexcitation represented by coefficient B_{ij} with units of $erg^{-1}cm^3s^{-2}$ and collisional excitation and deexcitation represented by rate coefficient C_{ij} with units cm^3s^{-1}. Therefore the population of a line in relation to all other lines of the molecule is found by equating the ways that depopulate a line with the ways in which lines are populated, as in Equation 2.5. [6]

$$\begin{aligned} & n_i \left[\sum_j (n_{\text{collider}} C_{ij} + B_{ij} \int_0^\infty J_\nu \phi_{ij}(\nu) d\nu) + \sum_{j<i} A_{ij} \right] \\ = & \sum_j n_j n_{\text{collider}} C_{ij} + \sum_j n_j B_{ji} \int_0^\infty J_\nu \phi_{ji}(\nu) d\nu + \sum_{j>i} n_j A_{ji} \end{aligned} \tag{2.5}$$

Knowing the relative populations of each energy level based on n_{collider}, ambient radiation field emission J_ν, and line profile ϕ_ν, we can compare the basic physics of the region to observable radiation. For transitions to level i from all other $j > i$ levels (the right side of Equation 2.5), the first term shows the probability of collisions between molecules causing a transition. The second term shows the probability of the ambient radiation field of stimulating a transition, and the third term is the likelihood of a spontaneous deexcitation to level i from levels above it. The left side of Equation 2.5 is made up of these same terms, but describe molecules in level i transitioning out of it.

The column density of a line, or the number of molecules in a given state in a cm^{-2} column along a line of sight, is equivalent to the volume density (particles cm^{-3}) of the molecular gas integrated over the path length:

[5] A_{ij} is the einstein coefficient for transition from level i to j

[6] n_i and n_j are the number density of particles in state i and j respectively. n_{collider} is the number density of the collider species, J_ν is the specific intensity of the emission from the transition in question, and ϕ_{ji} is the line profile for the transition.

$$N_u = \int n_u \, ds \tag{2.6}$$

We relate the path length ds to the optical depth τ or the opacity of the medium we are looking through by dividing the coefficient of absorption κ.

$$ds = \frac{d\tau}{\kappa} \tag{2.7}$$

When molecules absorb background emission they transition from a lower to higher state, therefore the coefficient of absorption can be described in terms of the density of molecules in the lower and higher states, and the statistical weights of each (g_u, g_l),

$$\kappa = \frac{c^2}{8\pi\nu^2}\frac{g_u}{g_l} n_l A_{ul} \left(1 - \frac{g_l}{g_u}\frac{n_u}{n_l}\right) \phi_\nu \tag{2.8}$$

The factor ϕ in Equation 2.8 above represents the line profile, which we model as a Gaussian function in this research.[7]

The column density of molecules in one energy level of a system is represented by Equation 2.9[8].

$$N_u = \frac{3h}{8\pi^3|\mu_{lu}|^2}\left[\exp\left(\frac{h\nu}{kT}\right) - 1\right]^{-1} \int \tau_\nu d\nu \tag{2.9}$$

The factor $|\mu_{lu}|$ is the magnitude of the dipole moment and the assumption is made that the population of molecules follows a Boltzmann distribution described by excitation temperature $T_{\rm ex}$[9]. This is the temperature required for this condition to be satisfied within the gas, but does not describe the physical temperature of the system itself.

[7] ν is the frequency of a transition.

[8] τ_v is the optical depth at one frequency, whereas τ is the total optical depth

[9] $T_{\rm ex}$ can be particular to a level. Local thermodynamic equilibrium (LTE) criteria are met if $T_{\rm ex}$ is constant for all lines

The total column density is then described as

$$\frac{N_{\rm tot}}{N_u} = \frac{Q_{\rm rot}}{g_u} \exp\left(\frac{E_u}{kT_{\rm ex}}\right) \tag{2.10}$$

This emphasizes the strong connection between the physics of the gas itself and a quantity that is readily observable. The column density depends on the excitation temperature of the gas and the optical depth along the line of sight. Optical depth and excitation temperature can be determined from observations using the equation of radiative transfer Equation 2.11.

2.1.3 Radiative Transfer

Not only is infrared and submillimetre light produced by the gas of a molecular cloud, it is also absorbed by other molecules along the line of sight. Therefore any model of molecular emission lines must account for this attenuation of emission through the the interstellar medium. Radiative transfer is a complex topic as it requires detailed knowledge of the media absorbing and emitting radiation, and it is often the medium itself we are trying to study in the first place. An in depth discussion of radiative transfer can be found in [72]. The total intensity of the emission at a certain wavelength that is received by a telescope is equal to the radiation absorbed by the interstellar medium subtracted from the total emission from the gas[10]. This is referred to as the equation of radiative transfer Equation 2.11,

$$-\frac{dI_\nu}{d\tau_\nu} = \Sigma_\nu - I_\nu \tag{2.11}$$

where the Source Function, Σ, is the is the intensity of emission from the medium along the line of sight with the source. The solution for a uniform

[10]This is acquired across the whole line of sight.

medium is given by Equation 2.12:

$$I_\nu \;=\; B_\nu(T_{\rm ex})(1-e^{-\tau_\nu}) + I_\nu^{\rm bg} e^{-\tau_\nu} \tag{2.12}$$

The value f is the filling factor, but for beam filling emission such as the large clouds of this study, I assume the filling factor is 1.

For the models used in this research, a uniformly emitting and absorbing medium is assumed, and therefore optical depth is proportional to distance through the cloud, with an optical depth of zero indicating the edge of the cloud closest to the observer. The reasonable assumption is made that over large scales, the radiation background can be defined as a blackbody with equation:

$$B_\nu(T) \;=\; \frac{2h\nu^3}{c^2}\frac{1}{e^{h\nu/kT}-1} \tag{2.13}$$

with temperature equal to the excitation temperature of the gas [47]:

$$T_{\rm ex} = h\nu/k\left[\ln(\frac{n_l g_u}{n_u g_l})\right]^{-1} \tag{2.14}$$

For millimetre spectral line measurements, what we are measuring is the difference between the source and the background intensity. Background emission from the sky is subtracted during the observing run and baseline subtraction step of the data reduction, so the total intensity of emission in the dataset is represented by Equation 2.15. Therefore what we are measuring is Equation 2.15, the difference in intensity between the source and background. This is also why all spectra (see Appendix) show the base of the spectrum at zero.

$$\Delta I \;=\; [B_\nu(T_{\rm ex}) - B_\nu(T_{\rm bg})][1-\exp(-\tau_\nu)] \tag{2.15}$$

The temperature measured by the receivers of the Heterodyne Array Receiver Program (HARP) are values of radiation temperature at the frequency observed, given bythe equation below [79]:

$$T_R = \frac{c^2}{2k\nu^2}\Delta I_\nu \tag{2.16}$$

The final model of the emission spectrum from the receiver is given by Equation 2.17,

$$T_R = \frac{c^2}{2k\nu^2} f[B_\nu(T_{\rm ex}) - B_\nu(T_{\rm bg})][1 - \exp(-\tau_\nu)] \tag{2.17}$$

where f is the filling factor, but for beam filling emission such as the large clouds of this study, I assume the filling factor is 1.

From the emission model discussed, it is clear that radiation temperatures give information on the excitation temperature and optical depth of the gas, which allow us to calculate volume and column densities for the region. The above calculation for our models is handled through the radiative transfer code RADEX [76] for a set of physical parameters chosen using a Monte-Carlo approach and a given range of physically possible results. We use RADEX to find $T_{\rm ex},\ \tau_\nu$ for a given $T,\ n,\ N_{\rm tot},$ and $\phi(\nu)$, where $N_{\rm tot}$ is the total column density of all transitions in $\rm cm^{-3}$.

2.1.4 Non-LTE Models

Building and fitting molecular line models to observations are complicated by non-LTE (Local Thermodynamic Equilibrium) conditions in a non-homogenous medium. The CO molecules in low-lying states are sub-thermally excited, meaning level populations are not excited and deexcited through collisional processes alone. In addition radiative excitation and deexcitation play a key role in populating the rotational lines of a molecule [79]. Therefore LTE as-

sumptions are invalid when modelling radiative transfer through a cloud, and the calculation of level populations and the radiation field are coupled. The problem is simplified by using a large-velocity-gradient (LVG) assumption when building radiative transfer algorithms. The assumption is that large scale motions of the gas are present, in which the system velocity changes on a scale larger than thermal broadening of the lines [79]. Therefore interactions between photons and gas are only considered on small scales. Radiative transfer is then modelled using the probability that a photon produced by gas within the cloud can escape unabsorbed [76]. If the optical depth is high, the emergent intensity approaches the source function (Σ), whereas if the gas is optically thin, emergent intensity is equal to the blackbody temperature integrated over the cloud scaled by the optical depth.

We use RADEX [76], a large velocity gradient (LVG) radiative transfer code to obtain excitation temperature and optical depth values for the ^{12}CO(3-2) and ^{13}CO(3-2) lines from Cygnus X molecular clouds. RADEX has been used to model the emission of many molecules for the purpose of obtaining physical parameters in molecular clouds (e.g. [29], [10], [66]). The LVG approximation assumes that the large scale velocity gradient is large compared to the velocity distribution at a single point [70]. This allows the calculation of level populations and radiative transfer to be computed separately, by defining optical depth in terms of a probability of a photon escaping in the medium (β). For a homogenous slab of material, this relation is $\beta = (1 - e^{-3\tau})/3\tau$ [76]. RADEX iteratively calculates the level populations from the escape probability (optical depth) until a converging model is reached.

2.2 Observer Conventions

2.2.1 Single Line Spectra

In this thesis, by spectral line observations, I am referring to observations of the same line (for example the ^{12}CO (3-2) line at 345 GHz) from clouds moving at different velocities relative to us in the Galaxy, thus Doppler shifting their emission from the 345.7959899 GHz line. We are travelling around the Galactic centre at 220 km/s, and based on the known rotation curve of the Galaxy, the apparent velocity of clouds decreases towards the Galactic centre, then increases towards the edge of the Galaxy eventually showing negative velocities outside of the solar circle (an 8.5 kpc ring around the Galactic centre intersecting the Solar System). Therefore each channel in a spectrum from submillimetre line emission actually corresponds to gas radiating at the observed wavelength, but located at a certain distance from the Sun. Lines in our spectra indicate different bodies of gas at different positions along the line of sight, rather than different lines of different energies. Velocities are all measured relative to our own rest frame and are labeled '$v_{\rm LSR}$' for velocity relative to our Local Standard of Rest.

2.2.2 Moment Analysis

Throughout this work, I frequently refer to moment maps, and present images of a few in later chapters. Moment analysis in astronomy is the process of integrating over a spectrum to show a specific property of the emission. Moment 0 maps are calculated by integrating the total emission along the spectral axis Equation 2.18. This is a measurement of integrated intensity. Moment 1 maps are created by adding up the intensity weighted velocity throughout the dataset (Equation 2.19). This informs the observer which channels, or which velocities are dominating the emission. Moment 2 maps show a measurement of velocity dispersion in the dataset (see Equation 2.20) and can be used as an

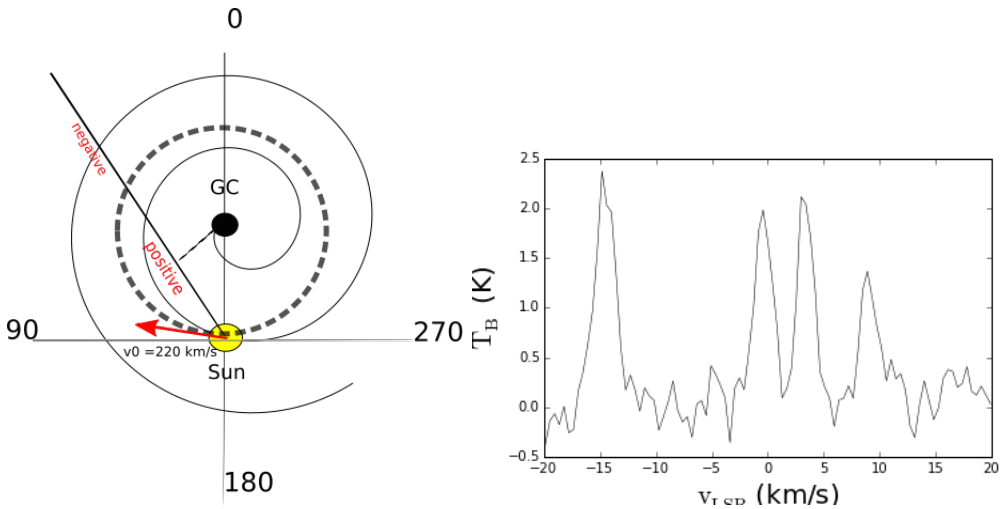

Figure 2.1: An example of a spectrum is shown in image to the right, where we see a series of lines at different velocities. The image on the left is a model of the galaxy showing the Galactic centre and the position of the Sun at 8 kpc. The sun is moving around the galaxy at 220 km/s, and velocities measured along a line of sight are quoted relative to this value. Along the line of sight shown in the figure, gas velocities increase positively moving away from the sun until they reach their highest possible velocity tangent to the Galactic centre, then begin to decrease. At the edge of the solar circle (dashed line), the velocity will be zero. After the solar circle, velocities start to increase in the negative direction into the outer galaxy.

measurement of turbulent gas within the dataset. In the following equations, moments are calculated by summing over the spectral axis (velocity).

$$M_0 = \Delta v \sum T(v) \tag{2.18}$$

$$M_1 = \frac{\sum vT(v)}{\sum T(v)} \tag{2.19}$$

$$M_2 = \sqrt{\frac{\sum (v - M_1)^2 T(v)}{\sum T(v)}} \tag{2.20}$$

2.2.3 Description of Temperatures

Astronomers frequently refer to a measurement known as brightness temperature as a means of presenting their observations. A brightness temperature is not a physical temperature such as the kinetic temperature of a gas. Brightness temperature is the temperature a blackbody would have to produce the same flux as a source Equation 2.16.

The receiver measures an antenna temperature (T_A) calculated from the power of the source detected at the receiver. The system temperature ($T_{\rm sys}$) is the total temperature of the system from noise, sky background, and source. Knowledge of the system temperature allows the calculation of antenna temperature, which represents the source. Correcting data for atmospheric absorption gives a measurement of corrected antenna temperature (T_A^*). Correcting this value for beam size, and receiver efficiency gives a telescope-independent main beam temperature or radiation temperature (T_R).

Chapter 3

Low Surface Brightness Gas

In this chapter I will discuss the process of locating regions of low surface brightness gas in the Galaxy. Based on the observations of the diffuse gas component of the Galaxy in [64] and [63], one could expect to find low surface brightness clouds in the interarm region of the Galaxy. I search for regions of low surface brightness gas towards bright areas of high mass star formation previously known to be associated with dark, dusty clouds that have the potential to be the source of low surface brightness gas in submillimetre. The focus of my research is the Cygnus X and W80 regions of the Galaxy as a continuation of an ongoing observing project.

3.1 Cygnus X Star Forming Region

The Cygnus X star forming region is a well studied region of the Milky Way Galaxy. It is a very active region of both high and low mass star formation, making it an ideal region of the sky to study the physical conditions necessary for all types of star formation. First observed in 1952, the name Cygnus X was chosen due to the large quantity of extended radio emission present observations [54]. The region itself is nearby at less than 2 kpc and is associated with multiple large OB associations, the largest of which is Cygnus OB2. Located

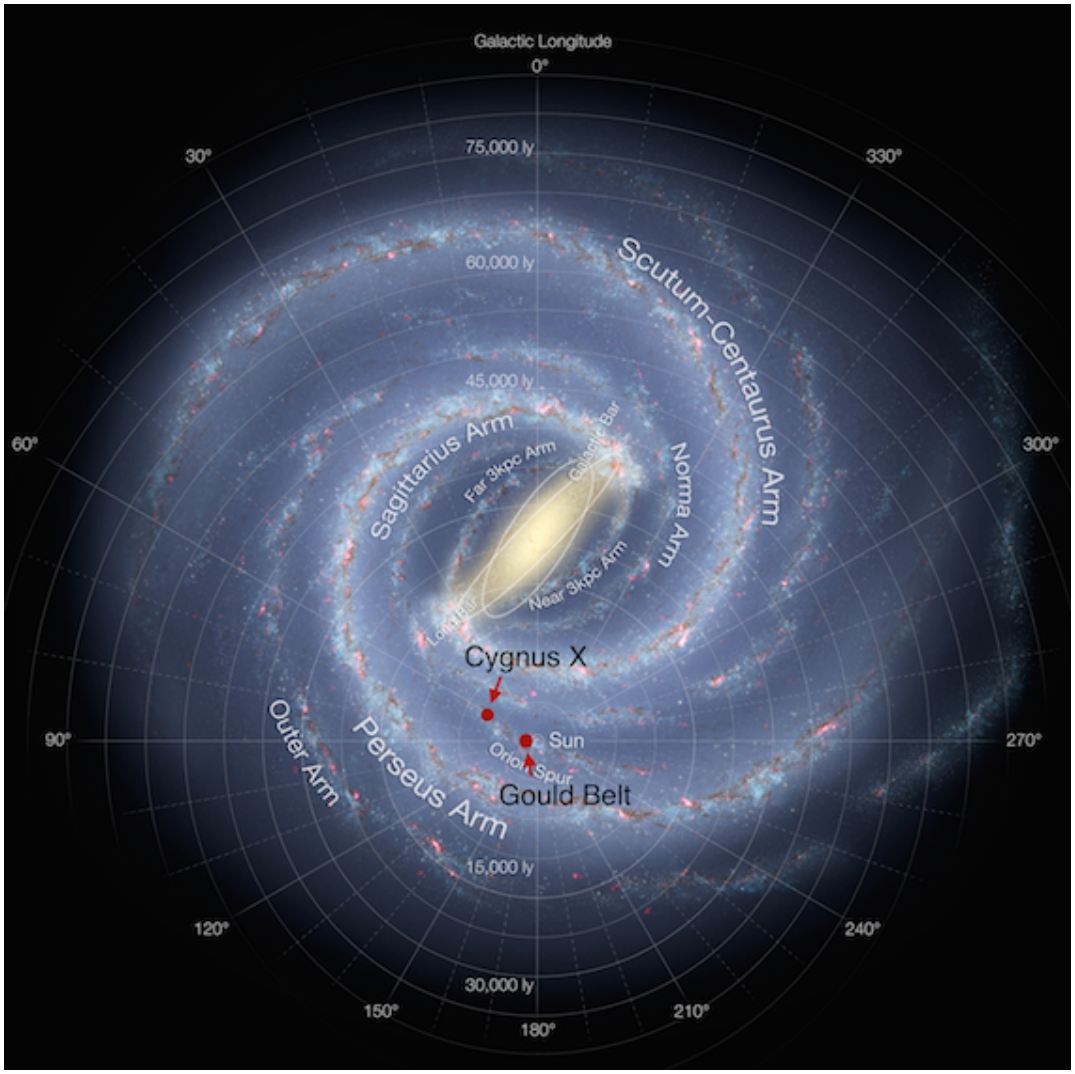

Figure 3.1: Map of Milky Way showing locations of the Gould belt and Cygnus X regions relative to the Sun. Background image courtesy of ESO.

at 1.7 kpc, Cyg OB2 is an association of thousands of low-mass stars amongst 120 bright O-type and hundreds of B-type stars (e.g., [33])[1]. A catalogue of Spitzer protostar candidates was published containing 1800 Class 0/1 and flat sed protostars identified using 24 micron photometry [36]. They observed that the protostar luminosity function in the Cygnus X clouds varies based on the environment that is forming YSOs.

The big question surrounding the Cygnus X region is whether or not all of the molecular gas is part of a single complex. Because of the location of clouds and star forming regions in the part of the Galaxy where Cygnus X is situated, the velocity dispersion within the cloud complexes is larger than the velocity of the complex moving relative to the Solar System. This blending prevents the association of the velocity and distance of a cloud and makes it difficult to discern which clouds are truly connected. This ambiguity has a large impact on our understanding of the physics and dynamics of the region. Resolving this ambiguity must be determined through examining structure and painting a bigger picture of the gas in the region. Surveys of CO molecular gas (e.g., [15]; [45]; [67]) support the idea that Cygnus X is a single connected complex. [67] observed the Cygnus X North and South clouds in ^{13}CO(2-1) and ^{13}CO(3-2) (30" and 90" beams respectively) with KOSMA and present the Cygnus X region as a Strømgren sphere[2] surrounding the Cygnus OB2 cluster at 1.7 kpc (e.g., [33]). The Cygnus X North cloud is at the forefront of Cygnus OB2 and the Cygnus X South cloud at the far side.

Large associations of high mass stars drive evolution in the surrounding clouds, and these large associations and their surroundings are what we detect as star forming regions in other galaxies. The Cygnus X region was previously known to be associated with diffuse molecular gas that absorbs much of the background light from the OB associations. This makes Cygnus X an ideal

[1]O and B type stars are very luminous, hot stars with temperatures between 10,000 and 30,000 K. O type stars are very rare white-blue stars

[2]Sphere of ionized Hydrogen surrounding O and B type stars.

region in which to explore the connection between Galactic and extragalactic star formation laws.

With all of these in mind, [23] set out to survey the entire Cygnus X region in CO(3-2) using the James Clerk Maxwell Telescope (JCMT). Their initial study created a pathfinder dataset to determine the possibility of mapping the whole region at high angular resolution. The purpose of the study was to look for molecular outflows and study the different stages of star formation present in the molecular gas. One of their main results was that the Cygnus X region may not be one large molecular gas component at all, as previously thought (e.g., [67]). The authors identified three main cloud complexes in the pathfinder dataset. They find a cloud structure associated with the star forming regions DR20, DR21, DR22, and DR23 that has gas at negative velocities, a cloud structure at positive velocities associated with DR17 and W75N, and a band of low surface brightness clouds in the forefront of the region moving at low positive velocities [23]. They use data from the Canadian Galactic Plane Survey (CGPS) [74] to study HI self absorption associated with these cloud structures and find that most of the HI self absorption is correlated with these low surface brightness clouds. They also locate 47 molecular outflows, most of which were previously unknown, and determine that most belong to the DR21 and W75N clouds and not the diffuse low surface brightness gas. They observe uniform brightness temperatures across the surface of these clouds. Furthermore they find that these clouds have narrow line widths, only extending through a few channels of the pathfinder dataset. They determined that these clouds must be cold and dense to support such properties, as well as relatively devoid of star formation. These clouds were determined to be the clouds of the Great Cygnus Rift, a region of infrared dark clouds that obscure a large portion of this region of the Galaxy.

As a continuation of this project, I used the pathfinder map produced by [23] along with further dense gas tracers to determine properties of this low

surface brightness gas in Cygnus X.

3.1.1 Cygnus X Raster Map

The $^{12}CO(3-2)$ 345 GHz observations were reduced as a part of the pathfinder project for the Cygnus X region [23]. Observations were centered on 345.7959 GHz for the $^{12}CO(3-2)$ line. Maps were produced in single-sideband mode with 2048 channels at 0.423 km s^{-1} spacing. Sampling was performed at 7.5″, and the array was rotated so that the receptors could scan 7.5″ apart. The pathfinder dataset is a mosaic of eight 1×1 degree tiles. Since the weather fluctuated during the period of observation, the noise level differs from tile to tile. For this analysis, we chose to use data from the four eastern tiles as these tiles contain most of the emission in the dataset and have a higher signal-to-noise ratio than the four western tiles. The eastern tiles also contain the distinct low surface brightness gas. The location of the pathfinder observations relative to the W80 observations is shown on a 20 cm radio continuum mosaic from the Canadian Galactic Plane Survey [74] in Figure 3.4. I include Figure 3.2 to show the relation of major star forming regions to bright areas in IR, radio, and submillimetre. This emphasizes that the bright limbs in CO also show strong IR emission.

3.2 W80

The W80 complex located to the northeast of the Cygnus X star forming region is an evolved site of low mass star formation [11]. With a distance of 600±50 pc [41], this system is located in the same region of the Galaxy as the Cygnus Rift, making it an ideal target for the study of low surface brightness molecular gas.

The W80 complex includes the North American and Pelican Nebulae visible in optical in addition to the dark dust lane known as L935 [46]. W80 is a 3° in diameter complex [78]. It also shares a line of sight with the Cyg OB6 and

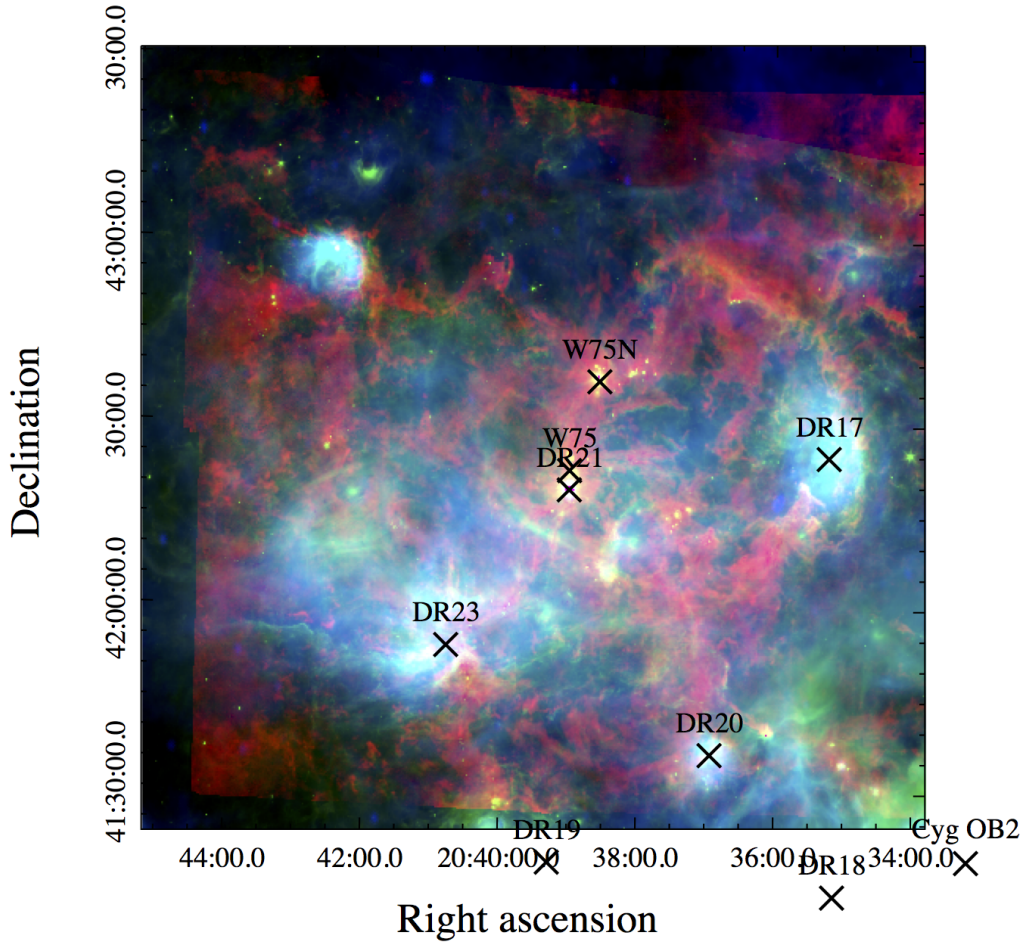

Figure 3.2: (top left) RGB image created using ^{12}CO integrated emission map (red), Spitzer 24 μm map (green), and CGPS 20 cm radio continuum image (blue). Major star forming regions are indicated.

OB7 clusters [75]. Two supernova remnants, G85.4+0.7 and G85.9-0.6 overlap W80 spatially but are located at distances of 3.8 and 5 kpc respectively [34]. SNR G84.2-0.8 is visible in the 1420 MHz radio continuum CGPS image shown in Figure 3.4 on the boundary of Tile 25 and 29 of the survey. Again this is a background source at 6 kpc [42] and thus not interacting with the molecular gas of this region. The bright HII regions of W80 are thought to be ionized by a star near the geometric centre of the W80 radio object [48], reddened by L935 in front of it. The likely candidate for ionization is an O5V star identified by [11] using the H and K bands of Two Micron all Sky Survey (2MASS) [69]. This source is one of many IR sources that were previously thought to be likely candidates for this ionization front as represented by the numerous studies aimed at finding the star.

The presence of bright HII regions and extended low density warm interstellar dust together with the dark dust clouds and numerous embedded stars brings the evolutionary stage of the region into question. HII regions trace later stages of star formation, whereas the presence of dark clouds with many signs of early time star formation are an indication of earlier stages of star formation. Bally & Scoville (1980) provide an evolutionary model of the region based on CO observations from the Five College Radio Astronomy Observatory [5]. They determined that W80 is an evolved region of star formation where the HII region we see as the Pelican and North American nebulae is breaking out of its parent molecular cloud, creating a streaming effect as the hot ionized gas flows into the low density intercloud medium. They detect symmetric high velocity gas showing evidence for an expanding and fragmenting molecular cloud. They identify gas at high positive velocities as gas erupting from the parent molecular cloud behind the HII region based on a correlation with Hα emission [5]. Gas at negative velocities is foreground gas based on its association with the dark dust lane. Based on their observations, they calculate $N_H \approx 0.8-2\times10^{22}$ cm^{-2} with a total mass of $M \approx 3-6\times10^4$ M$_\odot$. Based on the evolutionary stage of

the cloud, they estimate the age of the complex to be $3 - 6 \times 10^6$ years. Thus the W80 molecular cloud is in a post star formation stage where the parent cloud is being destroyed by the HII region within.

The L935 region is of primary interest in terms of the investigation of young star formation. There is evidence for the presence of young star clusters on the rim of dark clouds in the region [26]. The authors find that within a $2^\circ.4 \times 1^\circ.07$ Spitzer survey of young YSOs, there are 1600 YSO candidates, many of which lie in clumps overlapping the dark cloud. Most of these lie within the Gulf of Mexico region (see Figure 3.9 for locations of cloud regions on W80 map) where there are more young Class I YSOs. The median age of stars is ≈ 3 Myr [26]. HI self absorption is correlated with CO dark clouds and dense H_2CO regions [21].

At a distance of 600 pc, the presence of low and high mass star formation make W80 region an ideal analog for the study of diffuse molecular gas. We present moment maps produced from the JCMT $^{12}CO(3-2)$ raster maps of the W80 region at $15''$ angular resolution in Figure 3.6. This is the highest resolution CO survey to date. We identify the location of two outflows present in the dataset, and in addition, identify regions of low surface brightness gas separate from the Pelican and North American nebulae. Furthermore, I identify two regions of high velocity gas which may be accelerated by an expanding shell. We discuss the location of the YSO clumps relative to the diffuse emission and the percentage of molecular gas identified as faint or quiescent.

3.2.1 W80 Raster Map

Observations

The ^{12}CO(3-2) observations were taken at the James Clerk Maxwell Telescope (JCMT) using the Heterodyne Array Receiver Program (HARP) with the Auto-Correlation Spectral Imaging System (ACSIS). Data were obtained in August

of 2011. The project to map the W80 HII region was allocated 29 hours of Band 3 weather conditions to observe an 11 deg^2 area of the sky. Weather bands refer to different conditions for atmospheric opacity. For example Band 3 has $\tau_{225} = 0.8 - 0.13$ (note τ, i.e. the atmospheric optical depth, is at 225 GHz). Due to optimal weather conditions at the time of observation, data were taken at Band 1-3 conditions with τ ranging from 0.04 to 0.1. Therefore optimal noise levels could be achieved with faster scan times than initially requested. Observation parameters with atmospheric attenuation τ_{225} are given in Table 3.1.

On-the-fly mapping was used to create raster maps of the region, by which the field is sampled continuously by the telescopes as it sweeps across the field. Data cubes were scanned in a boustrophedon pattern (see Figure 3.3), allowing for a large region of the sky to be covered in less time. Due to the presence of bad receptors, spacing between scanning rows was set to half of the footprint of HARP ($120'' \times 120''$). Due to optimal weather conditions, scans were only performed in one direction for all but two requested tiles, so that more data could be collected in a shorter time. To avoid the confusion of real spatial structure from temporal effects, it is usually recommended that scans are taken in another direction (often perpendicular) to the original scan to get a consensus on the value of each cell. This process of 'basket-weaving' reduces the overall scan noise in the final data. Two of the low signal-to-noise data cubes were basket weaved but remaining cubes were scanned in one direction. Scan noise is removed during the data reduction process.

Data Analysis and Reduction

Data processing and reduction was performed using the submillimetre data analysis package *Starlink* [13]. Descriptions of all packages used in the data reduction and analysis are included in the Appendix. The raw data are downloaded as a time series cube: emission detected by each receptor as a function

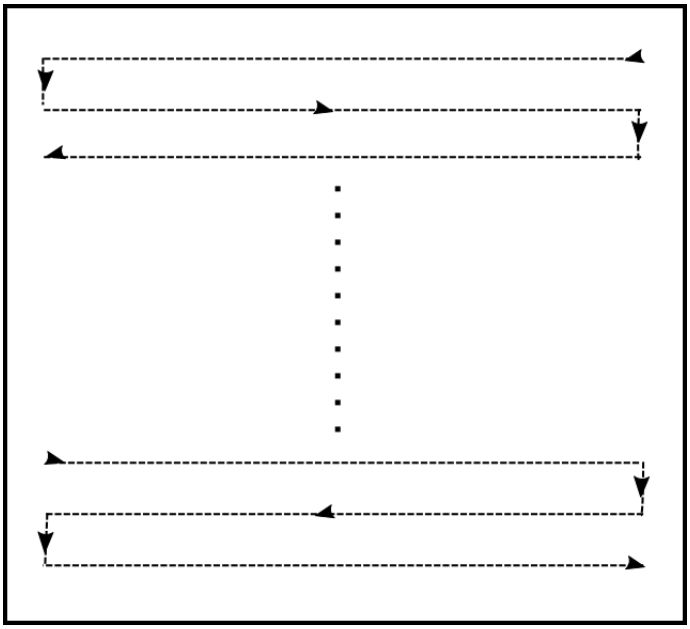

Figure 3.3: Boustrophedon Scan pattern followed by JCMT.

Table 3.1: HARP/ACSIS Observation Parameters

Source	date of obs.	int. time (s)	RA (deg)	Dec (deg)	τ start/finish
Tile 24	2011-08-31	3327.3	313.14	41.912	0.05/0.04
Tile 25	2011-08-27	1656.1	311.875	41.919	0.037/0.04
Tile 26	2011-08-28	3327.3	313.234	42.912	0.064/0.062
Tile 27	2011-08-30	3327.3	314.594	42.912	0.105/0.096
Tile 28	2011-08-28	3327.3	312.569	43.908	0.053/0.057
Tile 29	2011-08-29	3327.3	313.951	43.908	0.062/0.06
Tile 30	2011-08-30	3327.3	315.333	43.908	0.107/0.098
Tile 31	2011-08-29	3327.3	312.575	44.903	0.098/0.066
Tile 32	2011-08-29	3327.3	313.981	44.903	0.082/0.089
Tile 33	2011-08-31	3327.3	315.387	44.903	0.042/0.051

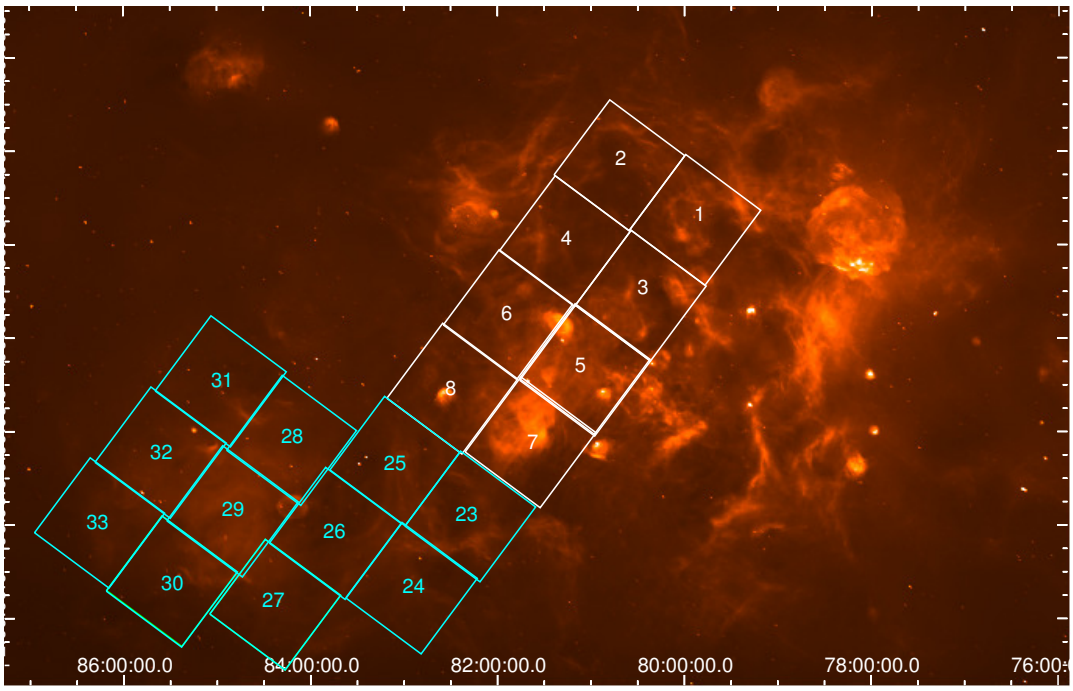

Figure 3.4: W80 and Cygnus X regions observed in ^{12}CO$(3-2)$ overlaid on the CGPS 21cm continuum mosaic. White tiles with numbers 1-8 indicate the location of the pathfinder dataset for Cygnus X reduced in [23]. The cyan tiles numbered 23-33 indicate the W80 mosaic put together in this project.

of time. This must be gridded to position-position-velocity (ppv) cube format for analysis and imaging. I used the KAPPA package function *makecube* for the process of gridding and tangent plane projection, but as the telescope was moving across the region during sampling, final datacubes are 1×1 degree in size.

The data reduction process was complicated by the sampling and scan pattern chosen. With two inoperational receptors at the time the observations were taken, the resulting maps show signs of streaking where no data were obtained. To remedy these gaps, the initial datacubes were gridded using a method of liner interpolation where the surrounding four pixels were sampled to obtain a missing pixel value. In addition, I allowed the default pixel size to be chosen by makecube for ideal map production. To fill in missing data, this meant that makecube chose a larger pixel size than the 6" sampling performed with HARP. With 7.5" pixels and linear interpolation of missing pixel values, the resulting datacubes showed aliasing affects from being undersampled. These appeared as large scale bright regions running along the scan direction of the cube. Therefore, final datacubes were created by gridding to $6''$ pixels, with the one-to-one pixel mapping to produce a properly Nyquist sampled (the minimum sampling needed to fully represent the incoming signal) final map for the 14" beam. This meant that large streaks of empty pixels ran through the datasets, which were corrected after the baseline subtraction.

Atmospheric calibration and continuum background subtraction are performed at the time of the observation by observing a standard source in between maps. Optical depth is tracked and accounted for so that atmospheric attenuation can be corrected. Temperature units of datacubes are therefore in units of corrected antenna temperature, or antenna temperature after calibration.

Baseline Subtraction

Due to variations in spectral response during the scan, all datasets require baseline correction. Inconsistencies in spectral response can be caused by fluctuations in atmosphere during the scan. We fit a third order polynomial to the spectral axis of each ppv cube in a region free of emission, and subtract this fit from the original cube. Typically no emission was present at velocities more negative than -40 km s^{-1} or greater than 30 km s^{-1}, but clouds present at high negative velocities meant I restricted fitting to channels between -200 and -85 km s^{-1} and greater than 30 km s^{-1}. This caused possible issues with improper baseline subtraction in regions where there are emission lines, but reduced the likelihood of subtracting real emission from data. The product is a datacube with receptors scaled to appropriate units of background subtracted radiation temperature. Uneven edges in cubes due to telescope turnaround (edges of scan pattern in Figure 3.3) were trimmed.

Filling in Missing Information

Lines of missing data in each datacube were filled using the KAPPA command *fillbad*. The command fits a smooth function to the datapoints surrounding a flagged pixel, and replaces the pixel with this value. I chose a footprint of 5×5 pixels to fill in each bad detection. The spectral axis remains unchanged. The number of iterations of the relaxation algorithm used was set to 5. The greater the number of iterations, the better the match to surrounding data. After each iteration, the root-mean-squared change in output values is given. This allowed me to choose the optimal iteration value.

Gaussian Smoothing

Even after filling in missing information in the data cubes, all cubes still retained residual scan noise. This appeared as faint streaks running across the datacube along the scan direction, visible in all channels at the same location.

Such artifacts were seen in [23] and were removed with a Gaussian smoothing method. We attempted the same approach. We created a convolved image from each dataset with a Gaussian beam of kernel dimensions $72'' \times 24''$ pixels, with the major axis aligned perpendicular to the scan direction for that dataset. Subtracting this smoothed cube from the original dataset, most of the emission was removed apart from the faint streaks which are constant and appear in all channels. Some residual emission remained, and this was flagged using the threshold tool of KAPPA. A third order polynomial was then fit along the scan direction, thereby giving a map of the line location, and these streaks were then removed from the data. As the streaking effect was still apparent in the dataset, I turned to a more robust method of removing scan noise using Fourier transforms.

Removing Faint Scan Artifacts with Fourier Transforms

Scan noise appears as horizontal or vertical streaks in the reduced data cubes. As the noise occurs as evenly spaced lines across the final data cube, I chose to scale down the effects of this noise using discrete Fourier transforms implemented through the python package *scipy* and its Fourier transform tool *fftpack*. The Fourier transformed cube, in frequency-frequency-velocity space, is created by applying a two dimensional discrete Fourier transform to each channel image, following Equation 3.1 [57]. From the moment map of the transformed cube (Figure 3.5), noise features are constrained to either a horizontal or vertical line in the Fourier transformed map.

$$H_n = \Sigma_{k=0}^{N-1} h_k \exp^{2\pi i k n / N} \tag{3.1}$$

Removing scan noise using FFTs is not a new method, and the procedure is outlined in [20] for basket-weaved data. The authors suggest using a smoothly

varying function to weight noisy regions in the Fourier transformed images of the two scan directions from 0 to 1 and normalizing before applying the inverse Fourier transform. For basket-weaved datasets, one would combine the weighted datasets and divide by the combined weights of both maps to mosaic results before applying the inverse transform. This process is known as plaiting. We have slightly adjusted this method to deal with our datasets, which are only scanned in one direction.

I start by creating a mask setting all values in the central circular area within a radius of 0.06 normalized spatial frequency units to one[3]. This omits nearly all real emission from the scaling process. Scan noise spikes are determined in the remaining transformed data by first using maximum and median value filters through *scipy*, The amplitude of the FFT image is sampled in 3×3 pixel boxes, maps of maximum and median values are returned. The difference between the maximum map and median map is found, and pixels with a difference value greater than the threshold cutoff of 2σ are flagged as a noise spikes.

I then create a median map by sampling the FFT image in 1×15 pixel boxes aligned perpendicular to the orientation of the scan noise, so that most pixels will be noise free. For each pixel flagged in the map, I take the corresponding value from the median map as an amplitude for both the replacement real and imaginary components. These are multiplied by the cosine and sine of $2\pi\phi$ for real and imaginary components respectively, with phase ϕ being drawn randomly from 0-1. Each channel image is then transformed back to ppv space, and the real component is added to the cleaned data cube.

[3]Spatial frequency represents the periodic nature of a structure. Low frequency points represent the largely unstructured emission belonging to the source; high frequency points belongs to objects with regular patterns such as noise in the original image, and therefore this is where we see scan noise appearing in the transformed image. I mask out the low frequency points to prevent altering emission from the source in the data.

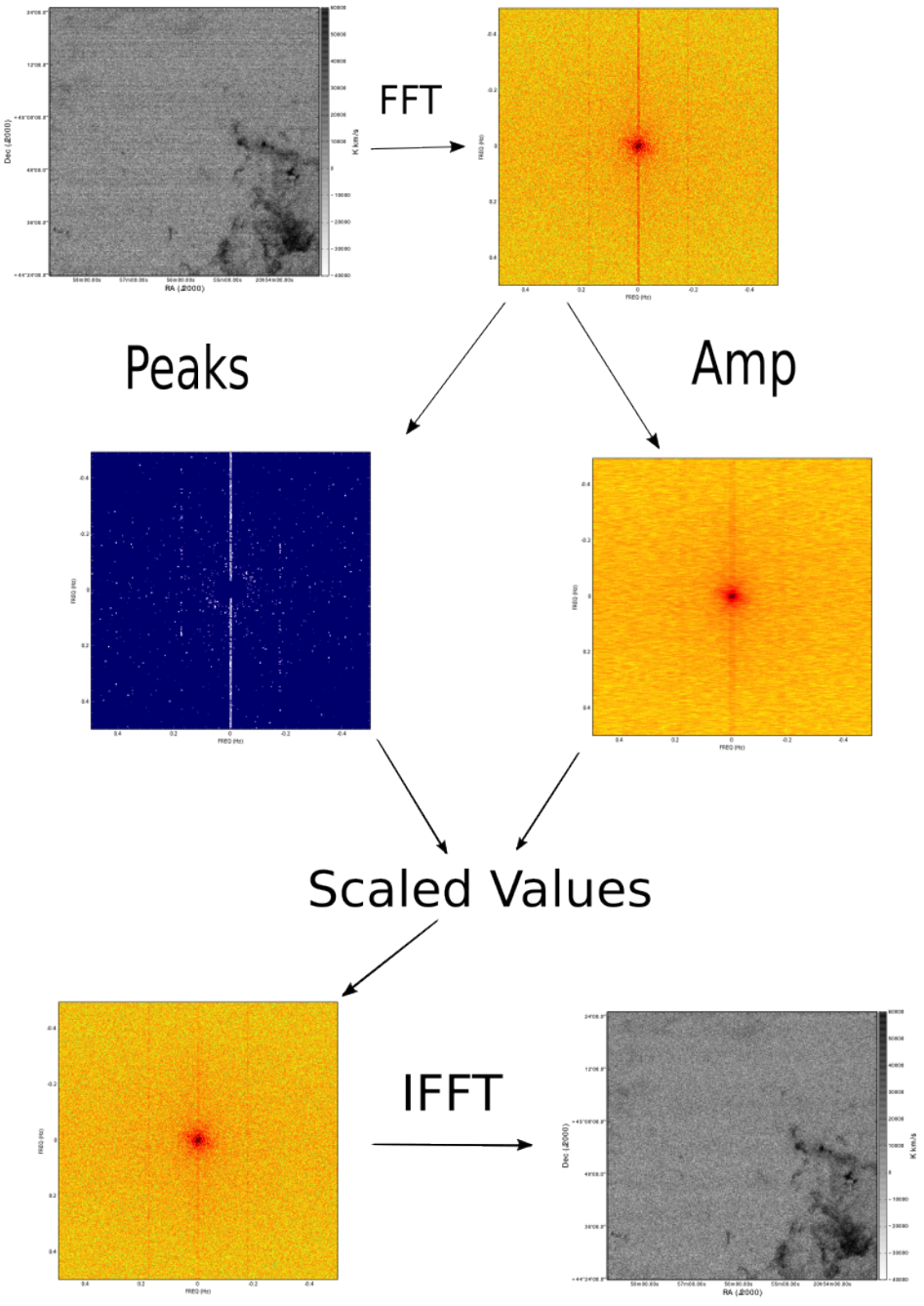

Figure 3.5: This Figure shows the process of Fourier Cleaning the data. Regions where noise spikes exist in the mask (labelled 'Peaks' above) are replaced with new complex values with amplitudes from the median filter mask (labelled 'Amp' above) and phase chosen randomly. We see scaled down noise peaks in the FFT image, which removes the streaks in the final cleaned image.

3.2.2 Mosaics

The final data mosaic was created using *wcsmosaic* as a part of KAPPA. The integrated moment 0 map of the whole region was also created as a mosaic of the individual Fourier cleaned images. The differences in residual scan pattern varied from cube to cube; thus each was treated separately to remove as much of the streaking as possible without affecting the emission. The moment maps shown in Chapter 5 are 5 σ_{rms} clipped to emphasize cloud structure, where $\sigma_{\rm rms}$ is the standard deviation of the thermal noise.

3.2.3 Integrated Velocity Maps

To visualize all ^{12}CO(3-2) emission, I present moment maps of the W80 region. As in §2.2.2, moment analysis is a method of examining large scale gas distributions in a region. Zeroth order maps show total integrated flux. First moment maps show mean velocity, or intensity weighted velocity distribution, and second moment maps show velocity dispersion. Moment maps were created using methods of the python package *SpectralCube* (see Appendix for package information). From a moment 0 map, we can see the total amount of gas in the data cube, as this is just the total integrated emission along the line of sight.

I used a method of sigma clipping to mask noise in the final maps. Each datacube was separately convolved in the spatial dimension with a 30″ Gaussian kernel and an appropriate noise cutoff determined from the distribution of negative values in the dataset. The cutoff value in the smoothed dataset is chosen to be 5 σ_{rms}. The mask created from the smoothed map was then applied to the corresponding full resolution dataset. Clipped cubes were then combined using the KAPPA function *wcsmosaic*. The clipped moment maps are given in Figure 3.6. An improved method of moment masking instead of sigma clipping of CO data is discussed in [14]. However, this method would reduce the likelihood of removing faint emission from the dataset. For the final W80

data cube, I found none of the large faint clouds with emission levels close to the noise background were removed by the clipping process, and thus did not pursue a more robust method of masking.

3.2.4 Moment Maps

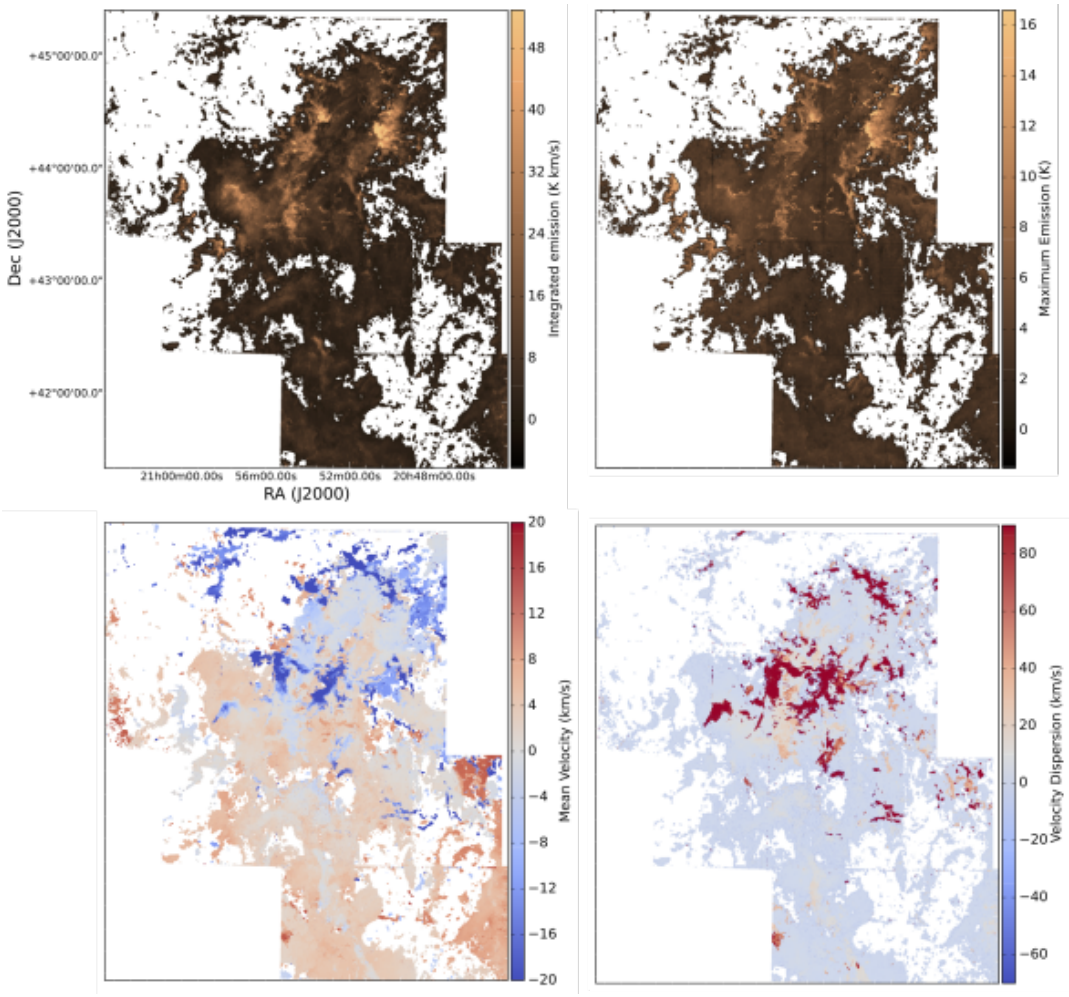

Figure 3.6: Moment 0 map (top left) showing total integrated emission in the datacube, maximum emission map (top right), moment 1 map (bottom left) showing velocity distribution of the gas, and moment 2 map (bottom right) showing velocity dispersion.

From the moment maps of the region presented in Figure 3.6, we detect high velocity CO at -80 km s^{-1}. These clouds appear as the darkest features

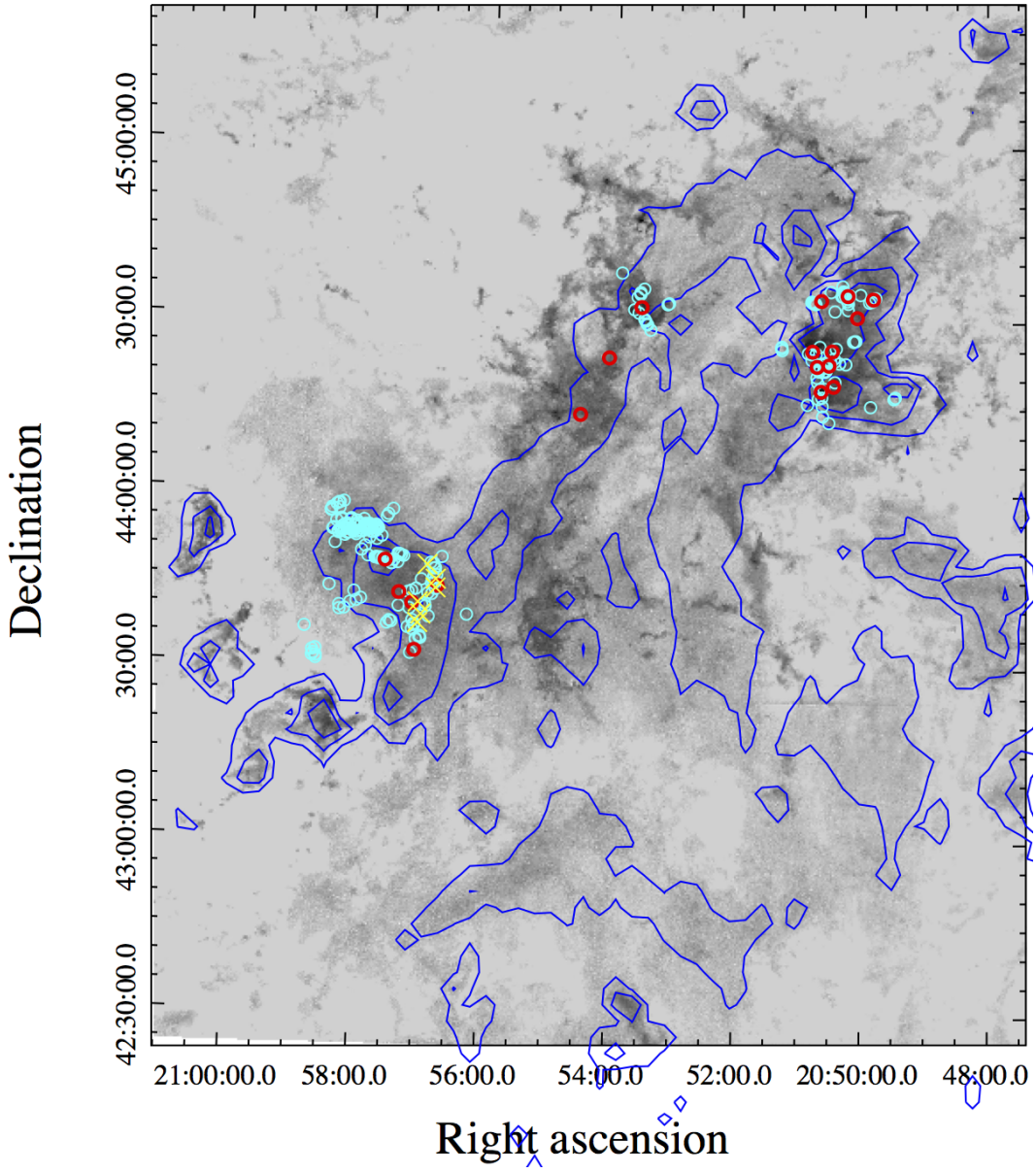

Figure 3.7: Moment 0 map of W80. Cyan regions mark molecular hydrogen objects (MHOs) and IR sources from [4], red marks Bolocam objects. Yellow markers show the location of molecular line fits for dense cores by [81].

in the moment 1 map. Although the spatial location of this gas seems to make it a likely candidate for association with the shock front of the HII complex, its location at -80 km s^{-1} places this gas far past the W80 region in the outer arm of the Galaxy. An examination of 21 cm spectral line data obtained from the Canadian Galactic Plane Survey reveals a possible association with an expanding HI bubble at this distance. As W80 is foreground to multiple SNRs, it is likely this gas is associated with a distant remnant. Expanding HII shells are capable of accelerating material, as we see in the molecular gas present out to -10 km s^{-1} and up to 10 km s^{-1} in positive velocity channels, but acceleration of more than 10 km s^{-1} is unlikely. We see that most of the emission lies around radial velocity of 0 km s^{-1}, which would be in agreement with a distance of 600 pc determined by previous studies.

In Figure 3.9, I highlight a few of the well studied morphological structures. The gas associated with the Pelican Nebula located to the north west of the image is bright in CO and connected to the gas of the North American nebula via the Atlantic region and Gulf of Mexico (see Figure 3.9 for locations of cloud regions). The gas of the Atlantic and Gulf of Mexico (hereafter GoM) that are seen as dark dust lanes in optical and infrared dark clouds, still appears to have a low surface brightness in submillimetre emission. The other dense molecular gas appears bright in the CO(3-2) line. This is another example of changing physical conditions of the gas, and can be compared to the clouds of the Cygnus Rift. They also occur at the same position in velocity space at about 600 pc. Therefore it is likely they are actually part of the same larger structure. Like the clouds in the Cygnus rift, the radiation temperature of these clouds remains uniform across the surface of the cloud at 1-2 K, with the exception of the region to the north east of the GoM. From previous surveys, we know that this region is the richest in star formation in the whole W80 complex, and this is evident by the bright ridge in the CO(3-2) image.

Unlike the clouds of the pathfinder dataset, the clouds that were identified

by eye as diffuse, low surface brightness gas, are far from quiescent. Previous studies of the YSOs and dense clumps associated with this region indicate that they are associated with the dense cloud. In Figures 5.4 and 5.5, I show plots of Class 0/1 and flat sed YSOs identified by [26]. There is a burst of young star formation occurring within the GoM. In the other area where we find low surface brightness gas to the south west of the GoM, I notice no bright peaks or association with YSOs. In Figure 3.7 we see the location of multiple Bolocam[4] sources associated with low surface brightness clouds. It is also evident that these clouds are sites of early stage star formation from the distribution of Class 0, I, II, and III YSOs. The Class 0/I and flat sources are concentrated in the molecular cloud structure, whereas the Class II YSOs are more dispersed, and the Class III YSOs are not associated with the clouds at all, but rather with the regions of the Pelican and North American HII regions.

3.2.5 Outflows

Examining the final data mosaic for the W80 region, I locate only two molecular outflows located near the most dense region of star formation in W80 in the GoM. I show the locations of these regions on 0 moment maps of W80 in Figure 3.9.

3.3 Brightness Distribution Function and Cloud Identification

Previous studies that have detected the presence of a low surface brightness cloud component have noticed distinctions in the features of clouds in terms of extent and lack of bright peaks over the surface. With the aim of determining a defining parameter to separate the distinct star forming gas from the diffuse

[4]Bolocam measures the thermal dust emission at $\lambda = 1.1$ mm. These data are from the Bolocam Galactic Plane Survey [1] and highlight dense star forming regions.

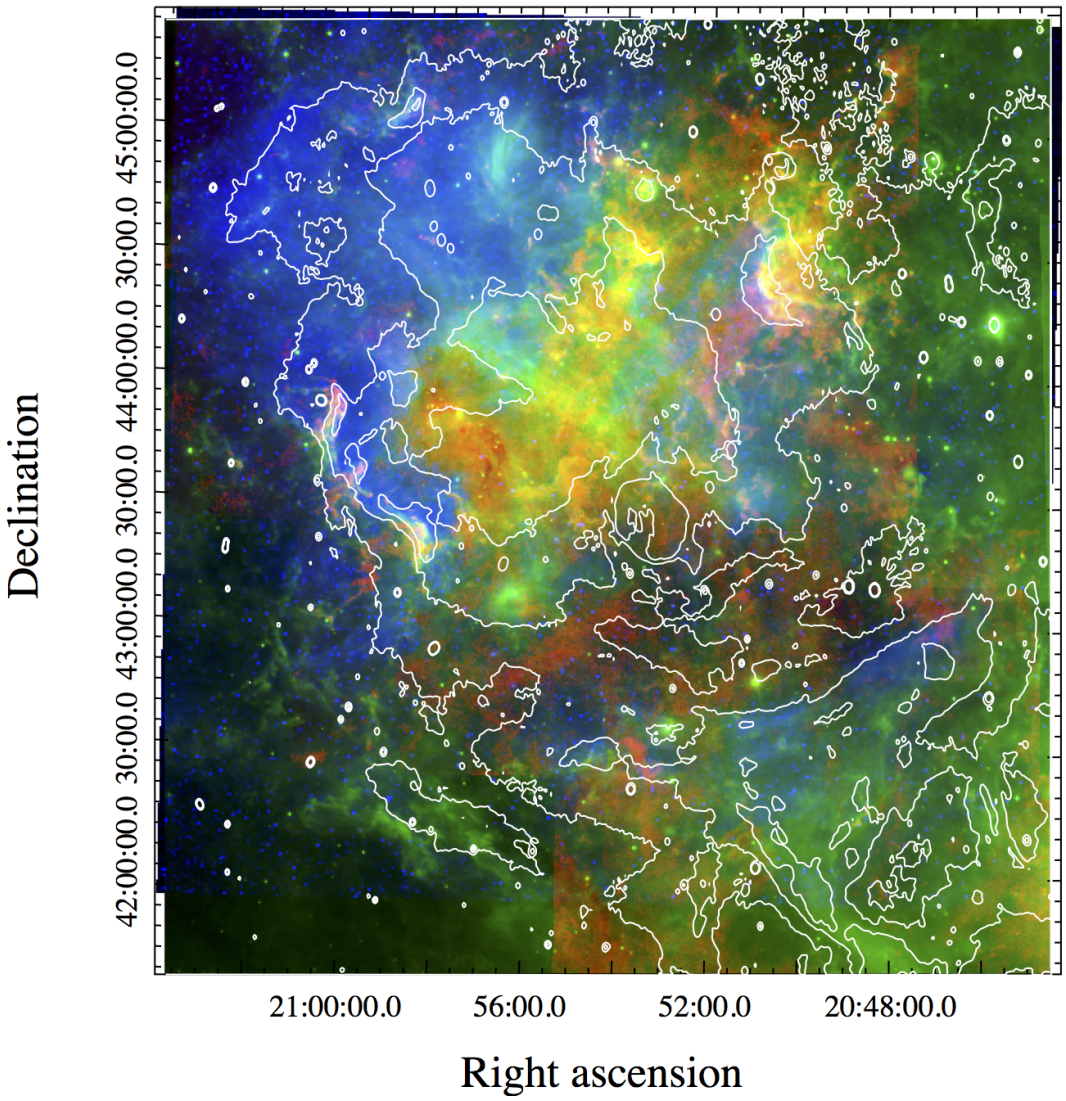

Figure 3.8: CO integrated intensity map (red), WISE 22 micron emission (green), DSS optical image (blue), and CGPS 21 cm continuum 5 K, 9 K, 11 K, and 14 K contours.

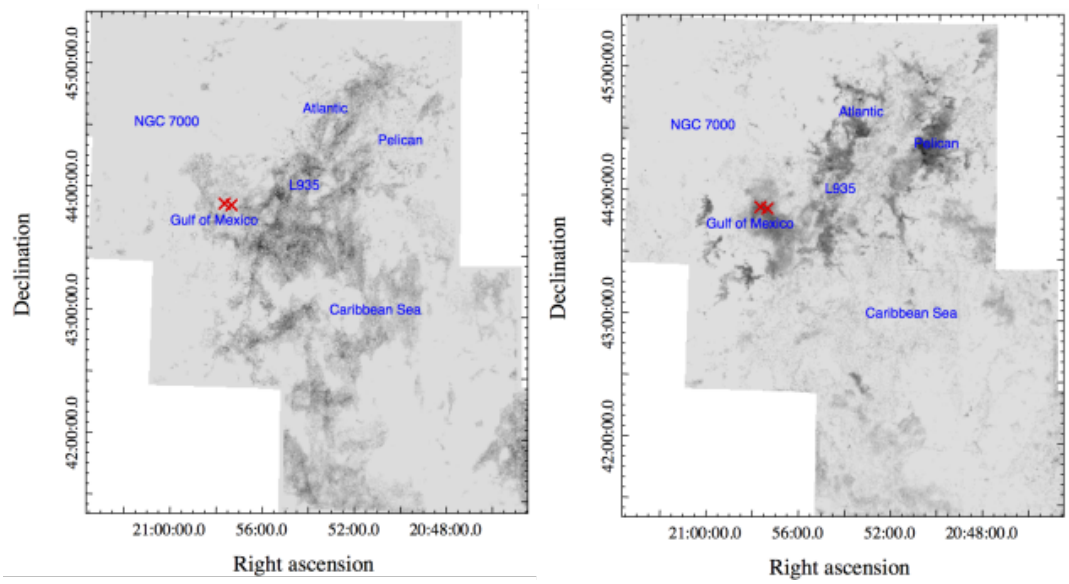

Figure 3.9: Integrated intensity maps of faint (left) and bright (right) gas in W80 with key regions labelled and the location of our two newly found molecular outflows shown in red. Color scale is inverted, darker regions represent stronger emission.

faint component in the Cygnus X dataset that comprises the Cygnus rift, I sought to use an attempt of cloud identification similar to that used by [64]. Attempts at a cloud-by-cloud identification through the use of dendrograms [60] failed, since the clouds of interest are too diffuse and faint. This is opposite to the compact bright clouds that algorithms like dendrograms are designed to find. Our interest is not in the small scale structure of the dataset, so I used a method of rolling box[5] parameter calculations to separate bright and faint gas, then the *label* function as a part of the *skimages measure* package to determine nearest neighbour voxel connections and produce labelled object cubes for the bright and faint gas.

I used a variation of the Brightness Distribution Index value defined by [64] to distinguish bright and faint gas. The authors recognized that the clouds of

[5]A rolling box is a method of calculating large scale parameter differences throughout a dataset by taking a square or cube region of a specified size, starting at one corner of a dataset, and stepping through the dataset performing statical calculations on every pixel within the box only at each step. It is 'rolling' since in general the step size is much smaller than the size of the box itself meaning each pixel is not included only once.

the interarm region had little evidence for emission above 4 K in brightness temperature opposed to the much brighter star forming gas. Our initial examination of the pathfinder Cygnus X dataset showed this same diffuse component contained little gas above 2 K in units of brightness temperature. The majority of the emission lying between around 0.5 K and 2 K ($2 - 8\ \sigma_{\rm rms}$ above noise background in ^{12}CO emission). Bright emission clearly associated with the DR17, DR21, and W75 star forming regions typically had temperatures well above 10 K, with the brightest gas being around 30 K. I performed a rolling calculation of the ratio of total bright to faint emission in $10 \times 10 \times 2$ pixel boxes throughout the dataset. I chose a shallow box in the velocity direction as the diffuse gas shows narrow line widths, individual clouds are typically only present in 2-3 channels of the dataset. The method was applied to a data cube smoothed to 40″ with a two dimensional Gaussian function to reduce the effect of noise on the calculation as well as to smooth cloud edges. I determined a brightness ratio (Equation 3.2) of bright to faint gas in a box at each position, and assigned each voxel in the resulting cube this new value. The use of brightness ratio here is different from the definition of brightness distribution index as defined by [64], since I am not taking the log of each component and I have determined different upper and lower boundaries for the gas based on properties of the cloud observed by eye.

$$\mathrm{BR} \;=\; \frac{\sum_i (T_i > 2\ \mathrm{K})}{\sum_i (0.5\ \mathrm{K} < T_i < 2\ \mathrm{K})} \tag{3.2}$$

I identified two clouds by eye that were representative of the diffuse gas component, and also those for which faint gas tracers observations were requested. These clouds were used in the calibration of the rolling box algorithm to identify cloud structure by changing the brightness temperature cutoffs to pick out different gas structures. Once the levels had been adjusted so as to

pick out the entirety of these two clouds from the rest of the gas in the region, I performed the same calculation on the rest of the datacube.

The very property that makes these clouds distinct is that they contain no bright features within their borders, therefore I chose the lower limit of the bright gas component so that the rolling calculation of brightness ratio (BR) is at or near zero over any extended diffuse component. Faint gas was then identified as any region in the BR cube with a value of zero, or near zero. Noise background was not included, as a sigma clipped dataset was used to mask background and intercloud regions as bad values, and are excluded in each determination of BR. I then subtracted all identified faint gas from the datacube leaving behind the bright star-forming component. The original unsmoothed data cube was then masked using the separated BR cube to give final bright and faint datasets. Moment maps showing the total integrated emission of each component are shown in Figure 3.10.

For this analysis, well known cloud structure identification from large scale down to smaller clumps is not necessary, and theoretically difficult as outlined in Colombo et al. (submitted). We are interested in large scale structure identification with YSOs and want to be able to make cloud mass estimates based on the fits of the CO(3-2) and CO(1-0) lines. I therefore assign object numbers to the original cloud label as mentioned above, with the lowest possible value of nearest neighbour connectivity. The reason for this is that we face the problem of velocity confusion near the edge of the solar circle. As the velocity of the clouds relative to the local standard of rest (LSR) is near zero, turbulence and other small scale motion within the clouds is larger than the overall velocity. Many background clouds appear in the same velocity channel as foreground clouds making a proper distance determination almost impossible. To avoid false connections in the spectral axis from being made, I designed the algorithm to be as insensitive as possible to connections between voxels, counting only direct connections (horizontal and vertical connecting pixels). The degree of

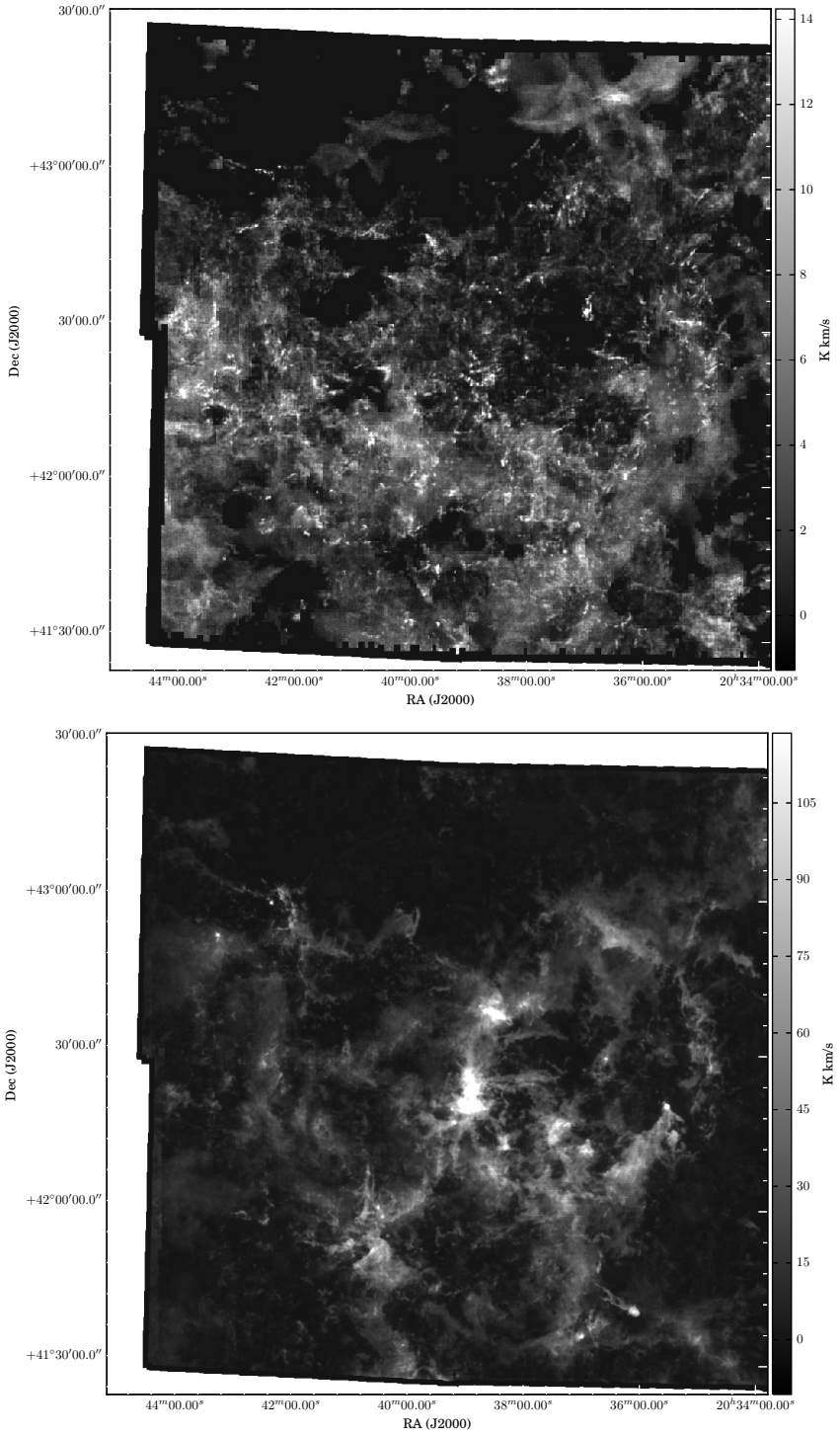

Figure 3.10: Integrated Intensity maps of Cygnus X faint gas (top) and bright gas (bottom). There are differences in brightness scale between the top and bottom image, the top image has a peak integrated intensity much lower than the emission in the bottom image.

connectivity is defined by the number of steps it would take to connect two pixels. If this is set to one, the pixels have to be touching, whereas a connection of two would include diagonal pixels.

I also separated the bright dataset into two separate datasets along the spectral axis to represent two of the three bands of clouds determined through HI Self Absorption[6] (HISA) feature association with CO by [23]. Contrary to previous studies, the authors find that the Cygnus X region consists of three separate regions of gas: faint gas in the forefront belonging to the Cygnus rift between 500 and 800 pc; bright gas associated with DR17 and W75 foreground of the Cygnus OB2 association between 1 and 1.7 kpc; and more distant background emission belonging to DR21 between 1.5 and 2.5 kpc. These are approximate, but they are able to distinguish gas belonging to DR21 as gas moving at negative velocities, gas associated with DR17 and W75 moving at positive velocities, and the gas of the Cygnus rift existing from velocities between 0 and 10 km s^{-1}. For simplicity, I use the maser distances to DR21 and W75 of $1.50^{+0.08}_{-0.07}$ kpc and $1.30^{+0.07}_{-0.07}$ kpc respectively, determined by [61] to represent distances to positive and negative gas structures.

Prior to cloud identification, I performed a morphological closing[7] on the boolean mask of each cube using a ball shaped structuring element with a width of 2 pixels to fill in holes in some of the clouds introduced by the rolling box method of identification. This closing also smoothed the cloud edges, and prevents small scale structure overlapping a larger structure from being identified as a separate object. I then performed an opening[8] with a small box shaped structuring element with a width of 3 pixels to remove noise spikes and outlines left by clouds in other datasets. This removed some of the otherwise

[6]HI is neutral atomic hydrogen.

[7]Closing is a mathematical operation of using a structuring element on an image to remove small holes by first dilating the image (expanding regions to match structuring element) followed by erosion (removing structures that do not match the structuring element).

[8]Opening is the reverse of closing, performing an erosion and then a dilation, this works to remove small areas of noise.

false connections within the cubes. The overall effect is demonstrated with one channel in Figure 3.11.

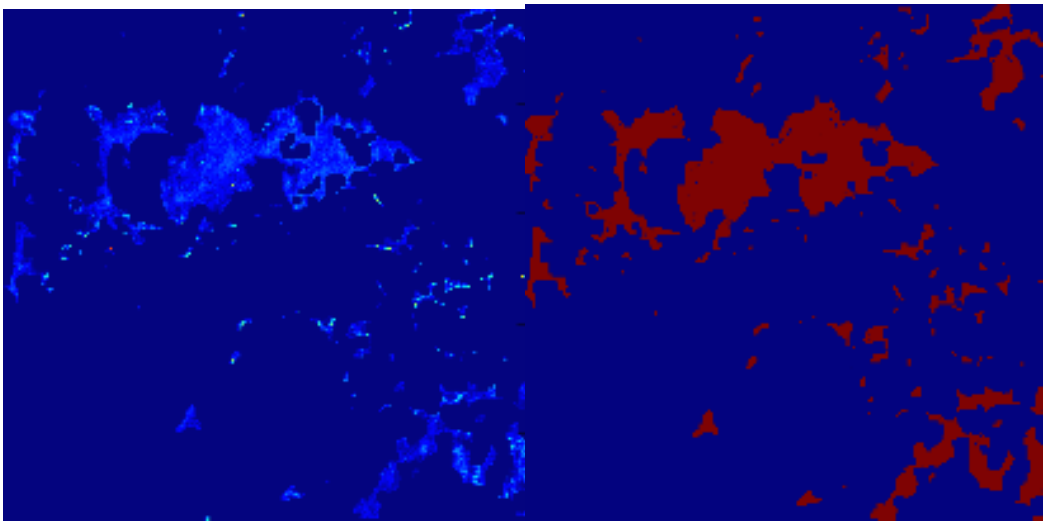

Figure 3.11: Before and after morphological opening and closing on channel of Cygnus X faint gas data cube. The mask (right) shows smoothed edges and some removed holes on surface of cloud.

The final cloud identification is completed on each of the three data cubes separately, with 2153 clouds identified in the negative velocity gas, 4940 clouds identified in the bright gas at positive velocities, and 1598 low surface brightness clouds.

In [64], the authors distinguish gas of the interarm and gas of the spiral arm regions using histograms of the brightness temperature taken over large samples of data, and they refer to these as brightness distribution functions (BDFs). They notice that gas of the spiral arms shows a lognormal BDF with an extended powerlaw tail from bright regions. Gas of the interarm region showed only a lognormal distribution that was truncated around 4 K. To compare our clouds with those of [64], I include samples of the brightness distribution functions for individual clouds shown in Figures 3.12, 3.13, and 3.14 along with an image of the cloud itself. Regions containing fewer than 5000 pixels are excluded from the analysis.

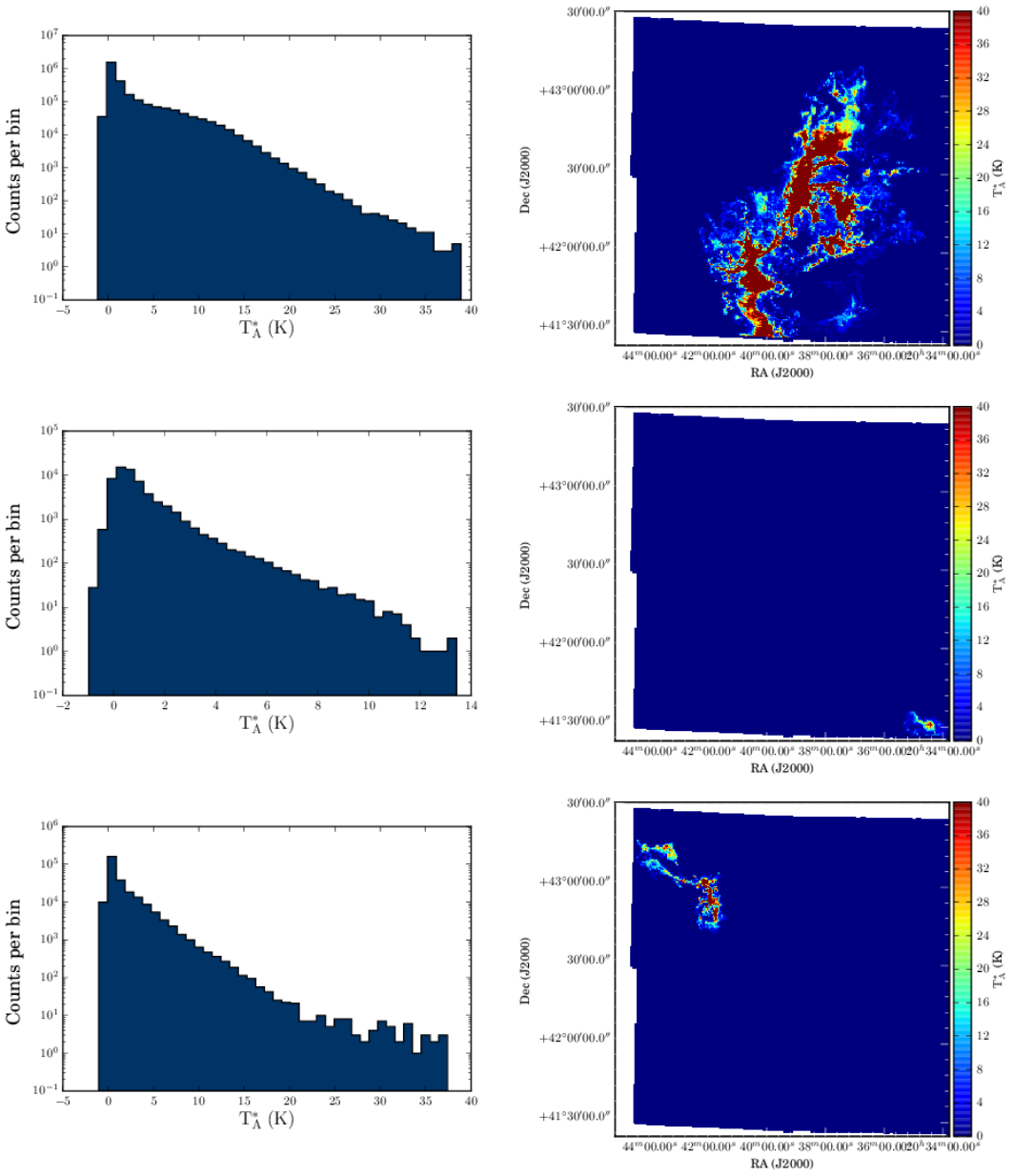

Figure 3.12: Brightness distribution functions of select large surface area molecular clouds moving at negative velocities. These clouds are believed to be associated with DR21 and show signs of active star formation.

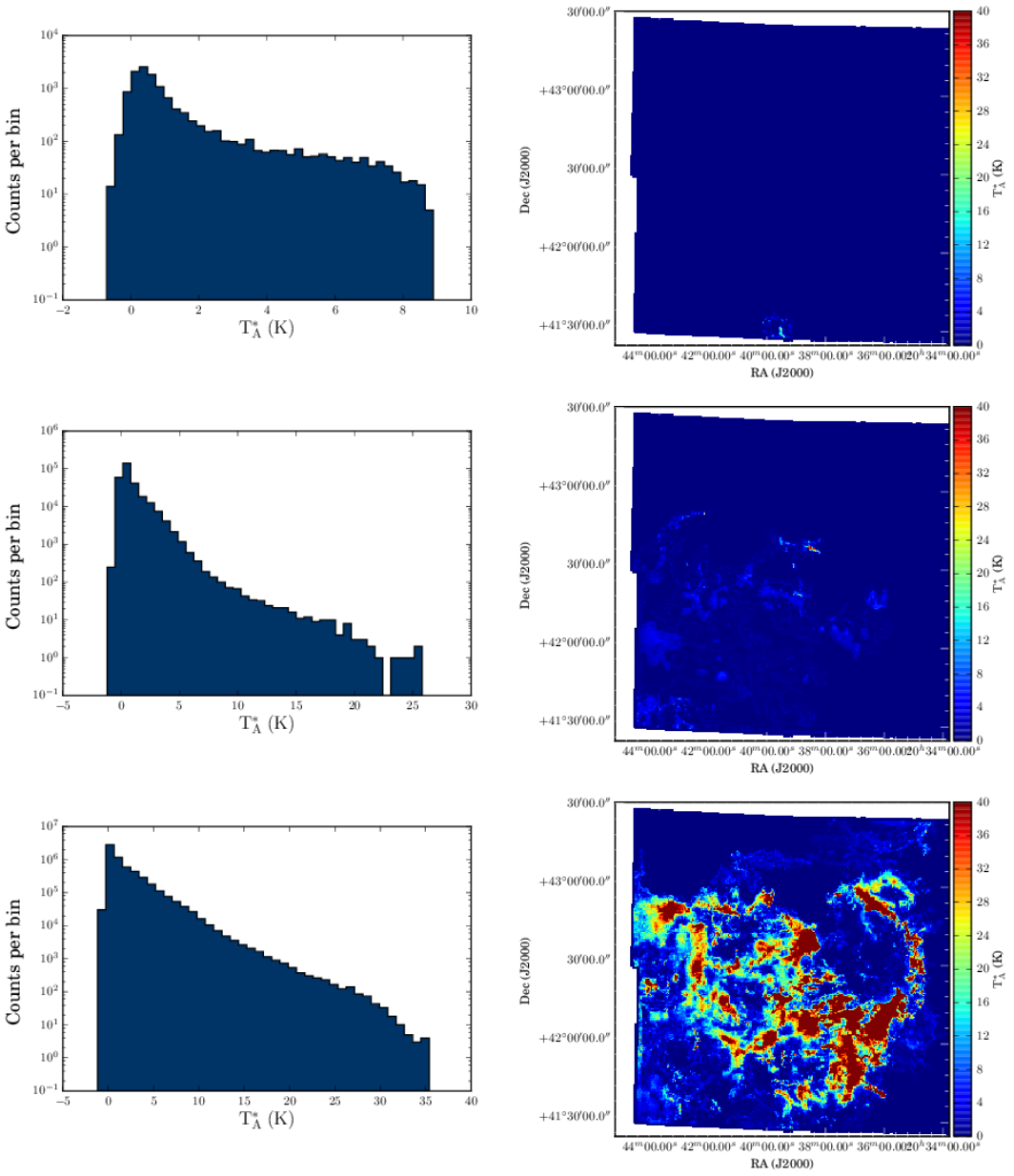

Figure 3.13: Brightness distribution functions of select large surface area bright molecular clouds moving at positive velocities. These clouds are believed to be associated with DR17 and W75 and show signs of active star formation.

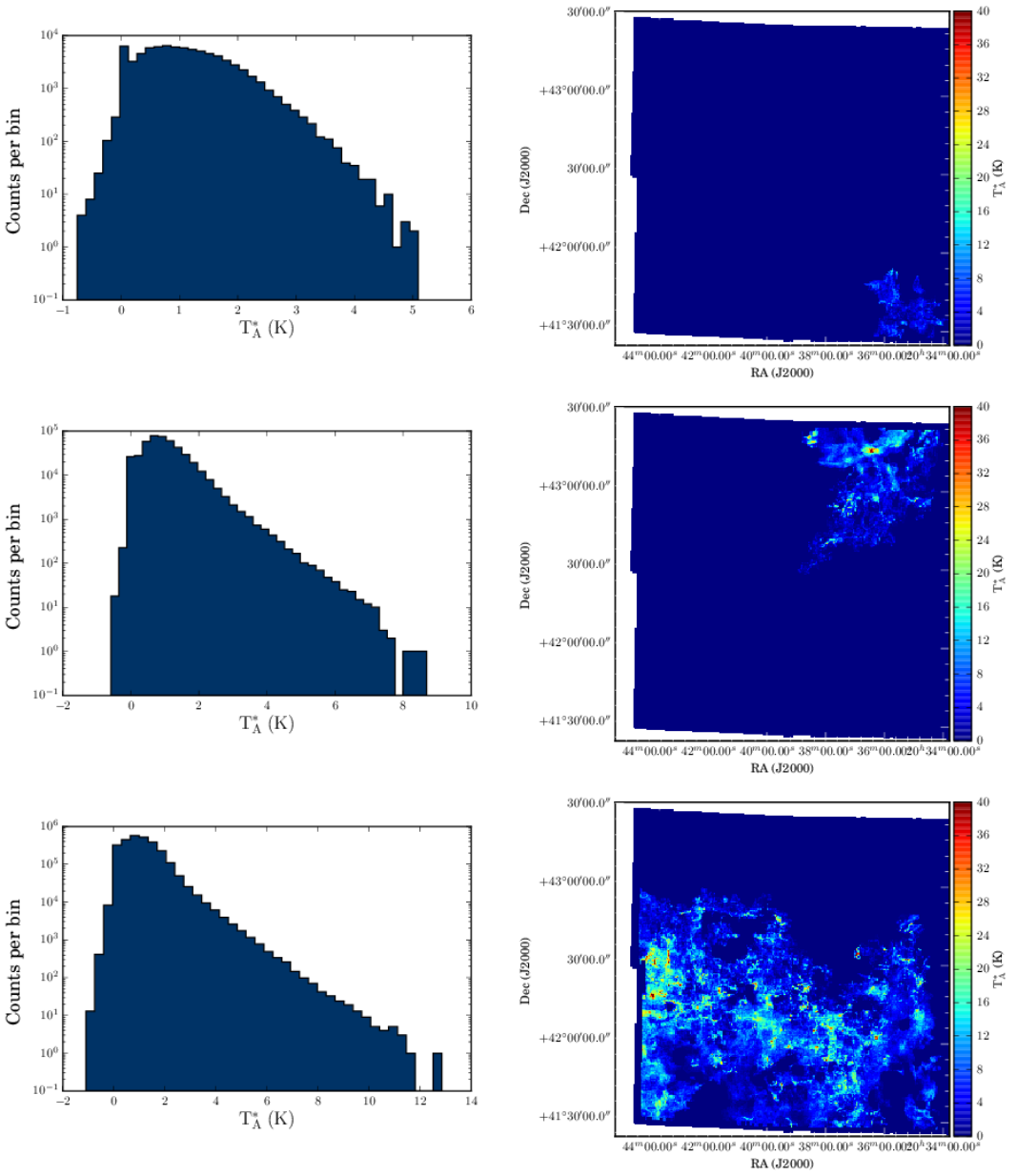

Figure 3.14: Brightness distribution functions of select large surface area faint molecular clouds moving at positive velocities. These clouds are believed to be associated with the Cygnus Rift.

I use the same process of distinguishing the low surface brightness gas in W80 as was done for the Cygnus X region. For the Cygnus X region, we have clear identifications performed by eye of the faint, diffuse gas component, and therefore I use the pathfinder dataset as a calibration for the gas of the W80 dataset in terms of defining a temperature cutoff for bright and faint gas. The moment maps for the faint and bright gas are shown in Figure 3.9. The main issue with using this method of filtering clouds is that we see evidence for rims and holes left behind from extracted clouds. To preserve the integrity of the maps, I did not remove this, even though these structures could affect mass and profile relationships determined for the region.

Object maps of individual cloud regions are created using the *label* function of *skimage* in python, combined with image morphology operators. Due to confusion of the gas at velocities near $v_{\rm LSR} = 0$, there are connections between much of the gas in the spectral axis. Therefore only a few large structures were identified in each dataset. The brightness distribution functions of some of the bright and faint cloud structures are shown in Figures 3.16.

Like the Cygnus X region, the shape of the brightness distribution function differs between the bright and faint gas, showing the lognormal distribution with a power law tail of bright gas and the lognormal BDF of faint gas.

3.4 Locating Low Surface Brightness Gas

From our findings, we see that low surface brightness gas in both the Cygnus X and W80 regions is concentrated to a narrow band of emission at a distance of around 600 pc. This gas is uniform in brightness temperature with typical temperatures around 2 K and narrow line widths. The brightness distribution functions are also narrow with typically lognormal shapes, and a calculation of rolling brightness distribution ratio on a smoothed map of the region shows that these areas have values of zero compared to the rest of the gas, indicating

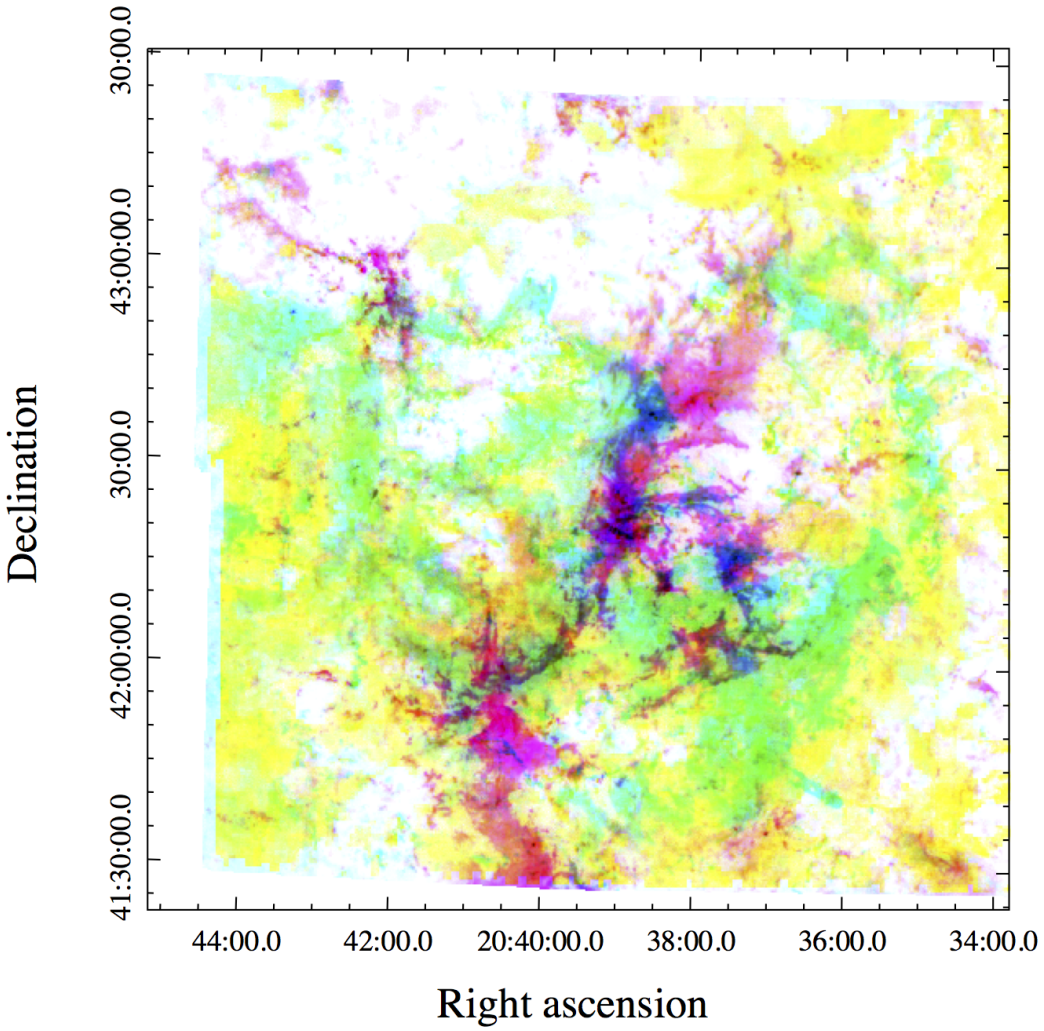

Figure 3.15: Color integrated intensity map of the Cygnus X region split into the negative clouds of DR21 (magenta), the positive velocity clouds of W75N and DR17 (cyan), and the faint clouds of the Cygnus Rift (yellow).

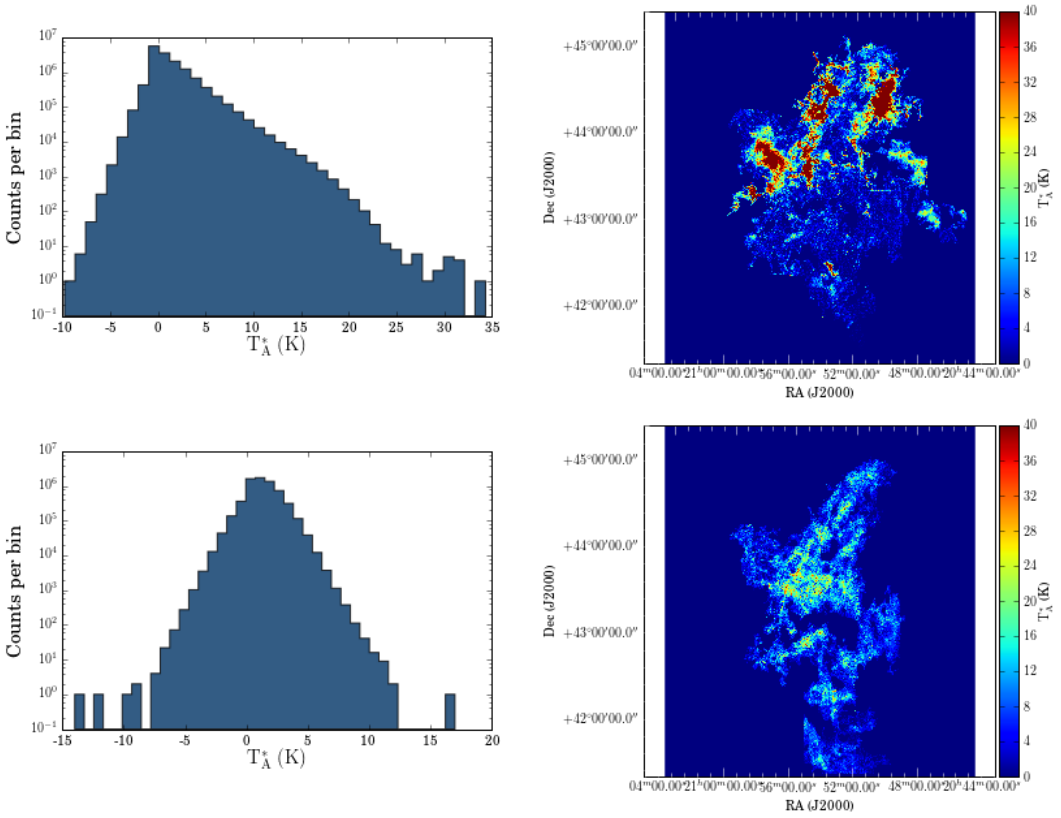

Figure 3.16: Brightness Distribution functions and masked maps showing the corresponding clouds for the bright (top) and faint (bottom) components.

no extended bright peaks across the surface of these clouds.

In the Cygnus X dataset, the low surface brightness gas accounts for 21% of the CO(3-2) luminosity of the region, and in the W80 region it accounts for 43% of the total luminosity. This is the total luminosity contribution of the faint gas to the region, not necessarily the mass contribution. I characterize the masses given in the analysis in the next chapter.

Chapter 4

Physical Conditions of Low Surface Brightness Gas

The focus of my work with molecular gas is to determine the physical conditions of the star forming and quiescent clouds in the Cygnus X region. Observations of these clouds in the low-lying levels of the CO molecule provide us with density and temperature probes of this gas. As ^{12}CO is the most abundant isotopologue of the molecule, even the ^{12}CO(3-2) molecule observable in the 325-375 GHz submillimetre band of JCMT remains optically thick. As a result, photons produced from the gas within this cloud do not readily escape. To constrain both the excitation temperature of the gas and the density of the molecular cloud, observations of both an optically thick and optically thin line need to be observed. We use observations of ^{13}CO(3-2) and C^{18}O(3-2) as optically thin tracers of the CO gas. Since a photon produced by an optically thin transition can escape the cloud, the column density of a region is the total emission along the line of sight. Physical conditions are determined through simultaneous fits of both the optically thin and optically thick CO lines to a known model. We include observations of the ^{12}CO(1-0) and ^{13}CO(1-0) lines to better constrain physical parameters.

The choice of using both ^{12}CO and ^{13}CO lines to obtain physical parameters

is affected by the $^{12}CO/^{13}CO$ intensity ratio. ^{12}C is the product of nucleosynthesis in early-type stars, whereas ^{13}C is a product of secondary processing[1] [80]. There may be correlation between regions where more dense molecular gas exists and a decrease in $^{12}CO/^{13}CO$ ratio [16]. The low temperatures within molecular clouds can lead to ^{13}C fractionation, by which ^{13}CO is preferentially produced from ^{12}CO. This would indicate that the $^{12}CO/^{13}CO$ ratio may be different for different types of molecular clouds. However, without further information, we assume the standard value of $\left[\frac{N_{12}{}_{CO}}{N_{13}{}_{CO}}\right] = 65$ [6].

In this Chapter, I will discuss the physical properties of the molecular gas in Cygnus X and the process of fitting the ^{12}CO(3-2) and ^{13}CO(3-2) molecular lines from a sample of bright and quiescent clouds in the Cygnus X complex. Data from the JCMT are fit using a CO line model constrained using RADEX parameters. A Markov Chain Monte Carlo approach implemented through the PYTHON package *emcee* [22] is used to fit the line to the observations. The purpose is to obtain physical parameters for a wide sample of clouds and present the first set of physical parameters for quiescent clouds in the Cygnus rift.

4.1 Cygnus X Dense Gas Tracers

Observations of ^{13}CO and $C^{18}O$ were made using the HARP/ACSIS on JCMT. The ^{13}CO and $C^{18}O$ observations were obtained In April and July of 2014. The initial proposal was allocated 10 hours of Band 2 weather conditions to observe 5 clouds in the W80 and Cygnus X region, with a total of 9 observations. Two of the larger more extended clouds were observed more than once. Given the extent of the clouds, I can justify only one or two observations per cloud because of the uniform brightness temperature across the surface. This implies that the physical conditions are not changing drastically and can be inferred

[1]The species is not a product of nucleosynthesis, but is created in chemical reactions of $^{13}C+$ with ^{12}CO within cold molecular gas.

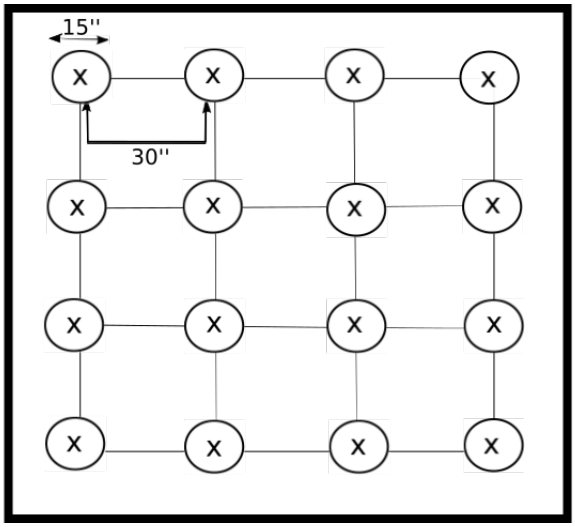

Figure 4.1: JCMT HARP 4×4 grid of receivers. The on-sky projected beam separation is $30''$, with a $15''$ beamwidth.

by one observation for the whole cloud. Targets were chosen for the Cygnus X region only, as previous W80 ^{12}CO raster maps were not yet analyzed for large scale structure at the time of observation. I note that there would be no obvious advantage to sampling clouds over a wider region. Band 2 weather conditions indicate an optical depth of 0.05-0.08 at 225 GHz. Due to poor weather conditions at the time of the July observation, I observed in Band 3 conditions at an optical depth of 0.08-0.12. The integration time was increased for each source observed at this time apart from the two clouds observed in April of 2014 in Band 2.

^{13}CO and C^{18}O data were obtained in grid position switch mode, meaning that the telescope is moved between source and background to subtract background sky emission during the observation. This is a standard procedure used for extended targets to ensure background is taken away from the source. The beam size is $15''$ and the receptors are spaced $30''$ apart, as shown in Figure 4.1.

The antenna temperature output from the telescope varies for each receiver. However, this antenna temperature is not the radiation temperature of the gas. As telluric lines interfere with observations of CO in the submillimetre

regime, the antenna temperature is corrected for atmospheric absorption and continuum opacity through the observation of a standard source. Atmospheric calibration is performed at JCMT during the observation, as the atmospheric optical depth measurement changes throughout the night. The corrected antenna temperature is given by Equation 4.1, where τ_A is the atmospheric optical depth at zenith and A is the airmass towards the target.

$$\mathrm{T}_A^\star \;=\; \mathrm{T_A} \exp(\tau_\mathrm{A} \mathrm{A}) \tag{4.1}$$

To determine the corrected radiation temperature, the corrected antenna temperature is then divided by the efficiency of the telescope. This includes losses due to spillover, or the ratio of the total power detected to the total incident power at the telescope, and any signal loss due to the telescope itself. The main beam efficiency η is measured regularly at JCMT from observations of Jupiter, Mars, the Moon, and Saturn. Main beam efficiency at 345.8 GHz has remained stable around 0.6 since 2007 measured. Therefore to convert ^{13}CO and C^{18}O corrected antenna temperature to radiation temperature, I divided each corrected antenna temperature by $\eta = 0.6$. For beam filling emission, the radiation temperature is equal to the main beam temperature.

Regions for observation in ^{13}CO and C^{18}O were selected using the observations of the Cygnus X region in ^{12}CO(3-2) from the pathfinder project [23]. The authors detected low surface brightness gas present in the $0 - 10$ km s^{-1} range of the Cygnus X region. By manually scanning through channels, I searched for large uniform, faint clouds. The brightness temperature of these clouds is less than 4 K as seen by [64], and most of this low surface brightness gas should exist around a temperature of $1 - 2$ K. These clouds have also been characterized as having narrow line widths, therefore targets were then selected by searching by eye for faint, uniform brightness clouds that are only present

within a couple channels of the dataset. Chosen target clouds with the HARP footprint superimposed are shown in Figure 4.2.

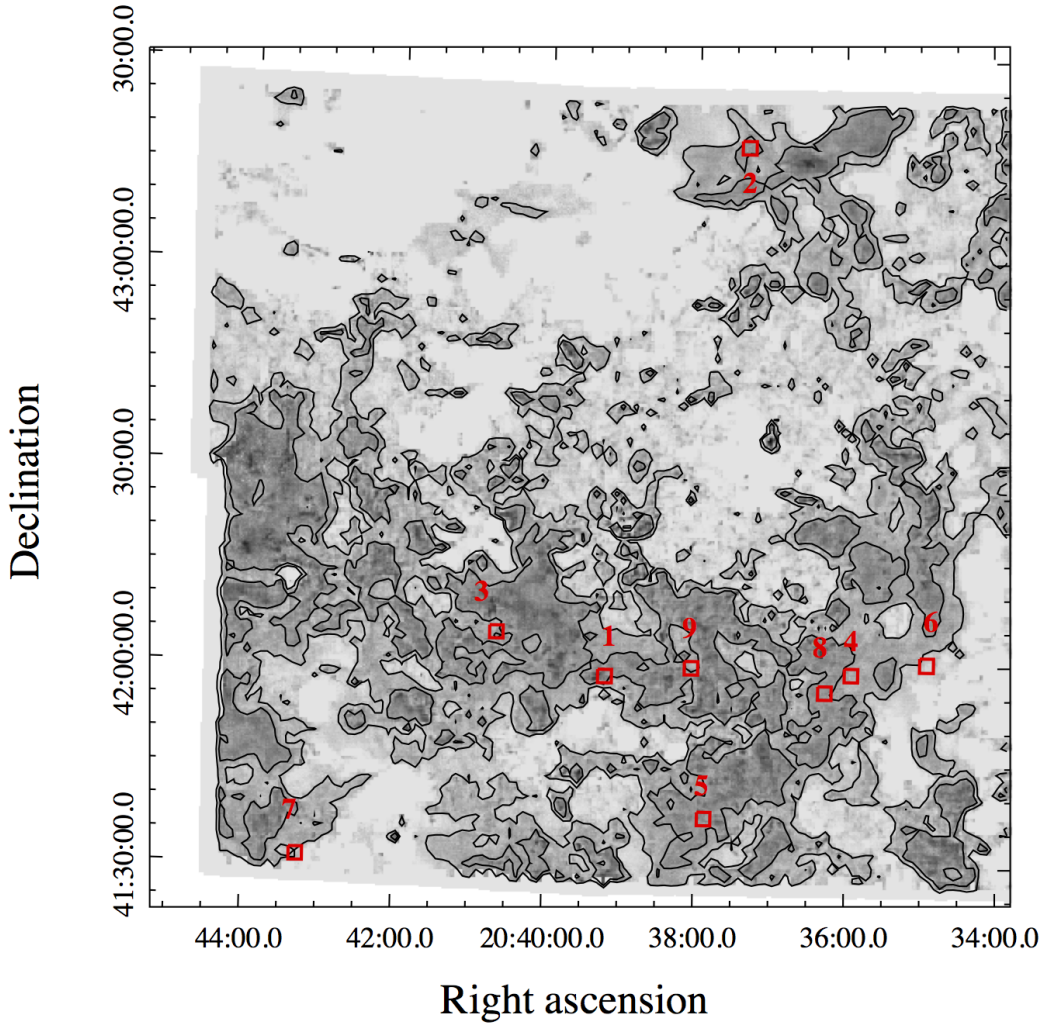

Figure 4.2: Integrated intensity map of faint clouds only showing HARP footprint for 9 dense gas observations in ^{13}CO and C^{18}O. Contours represent the approximate location of 1.0 K and 0.5 K CO gas assuming the faint gas component occupies 10 channels.

4.1.1 Data Processing and Reduction

The ^{13}CO, and C^{18}O data were reduced using data processing software *Starlink*, and packages KAPPA and SMURF supported by the Joint Astronomy Centre [13].

Table 4.1: $^{13}CO/C^{18}O$ HARP/ACSIS Observation Parameters

Source	Exp. Time (s)	$\langle T_{sys} \rangle$ (K)	RA (deg)	Dec (deg)	τ start/finish
Cyg X1	1200	434	309.794	41.98	0.073/0.077
Cyg X2	3600	405	309.328	43.286	0.065/0.078
Cyg X3	1800	868	310.158	42.086	0.106/0.095
Cyg X4	1800	718	308.973	41.986	0.107/0.095
Cyg X5	3360	575	309.460	41.620	0.095/0.1
Cyg X6	3600	546	308.722	42.004	0.101/0.103
Cyg X7	1800	535	310.812	41.517	0.101/0.099
Cyg X8	3240	906	309.061	41.934	0.107/0.1
Cyg X9	1800	612	309.507	41.993	0.097/0.101

The HARP/ACSIS detector timeseries data supplied to the observer shows receptor response over time. These data need to be gridded into a datacube of sky position and frequency. I did this using the SMURF command *makecube*. The function of *makecube* is to grid the data to an output cube using gnomonic or tangent plane projection to map the input pixel to the nearest pixel in the output map. I chose final pixel sizes to be the default values determined by *makecube* with respect to beam size. Projection parameters were not put in manually, but determined by *makecube* itself. During the period in which the observations were taken, there were two unresponsive receptors (receptors H13 and H14). These were automatically flagged in the calibrated dataset. Baselines[2] were removed by fitting regions free of emission in the spectral axis with a third order polynomial, and subtracting this fit from the original data. Most emission in this region occurs in the $0 - 10$ km s^{-1} channel range, with some higher velocity gas. I fit the channels from -100 to -20 km s^{-1} and 20 km s^{-1} to 100 km s^{-1} that show little to no emission in all spectra. Bad baselines show drastically varying receptor response from channel to channel. Throughout all observations, receptor 5 was flagged due to a poor baseline that could not be removed through a polynomial fit. After baseline removal, all observations were

[2]Baseline refers to the fluctuation in spectral response from calibrated background.

rebinned in their spectral axis to match the spectral resolution of the pathfinder ^{12}CO data at 0.424 km s^{-1} using *Starlink* package *sqorst*.

4.1.2 CO(1-0) Data

Data observed with the Five Colleges Radio Astronomy Observatory (FCRAO) Outer Galaxy Survey were kindly provided by Chris Brunt from the University of Exeter, who supplied CO(1-0) and ^{13}CO(1-0) for both the Cygnus X and W80 regions. The FCRAO data were taken on the 14-m Quabbin telescope using the SEQUOIA 16 element receiver array. Those data have a resolution of 45" and 50" for the ^{12}CO and ^{13}CO lines respectively. Chris Brunt provided a custom reduction that corrects the data cubes for stray radiation.

4.1.3 Gaussian Modelling

Prior to the fits of all lines using CO models, I fit all lines using Gaussian functions. Many of the lines were blended together in ^{12}CO, so this provided a means of modelling all other emission during the CO line modelling step that did not belong to the line of interest. Furthermore, this provided line centres for the ^{12}CO and ^{13}CO models, along with excellent prior values for the line width. Initially, peaks of spectral lines were determined, and Gaussian models were iteratively added to the spectrum until all lines were fit. During the later spectral fitting, the line of interest is removed from the Gaussian model of the full spectrum, and fit with the fitting code described below.

4.1.4 Spectrum Extraction

I extracted spectra from the datacubes in PYTHON using the package *Spectral-Cube*.

An array of world coordinates for each pixel of the ^{13}CO cube was obtained through the use of *SpectralCubes spatial_coordinate_map* feature, which uses

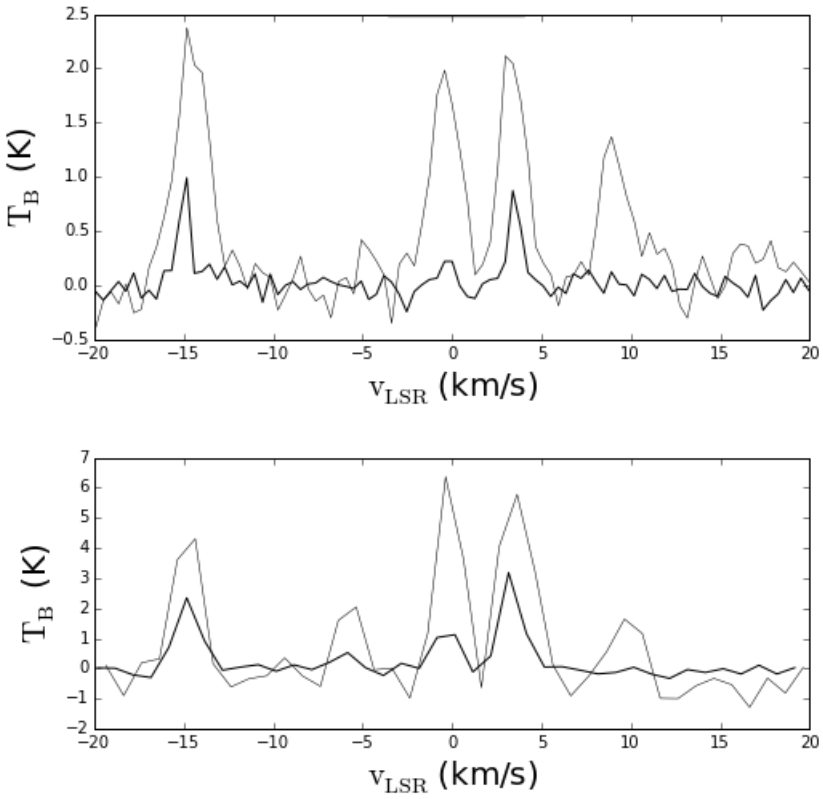

Figure 4.3: Sample spectrum observation Cyg X1. Top figure shows ^{12}CO$(3-2)$ and ^{13}CO$(3-2)$ lines and bottom plot shows the ^{12}CO$(1-0)$ and ^{13}CO$(1-0)$ lines at the same position. Thin lines represent the ^{12}CO spectral lines and thick lines represent the ^{13}CO data.

astrometric information from the telescope stored in the header file to map array indices to sky coordinates. The same process is repeated for the ^{12}CO datacube, and the pixel matching the ^{13}CO pixel position is selected for extraction.

The spectral axis of the datacube and temperature values were output as an array using SpectralCube. This is flattened into a 1D array producing the output spectrum. All spectra are truncated to the same -20 to 20 km s^{-1} velocity range for fitting. An example of spectra extracted from each set of line data for a given position is shown in Figure 4.3.

4.1.5 Models of CO Emission Lines

As each line represents a different molecular cloud with varying physical conditions, I fit each line separately. The model used is based on the material discussed in Chapter 2 for modelling the column density, volume density, kinetic temperature, optical depth, and excitation temperature of the gas. I take the background temperature of the gas to be 2.73 K, the value of the Cosmic Microwave Background (CMB). The brightness temperatures of the source and background are calculated from the transition energy ($E = h\nu$) and excitation temperature of the gas, $T_{\rm ex}$. The transition energy for ^{12}CO, ^{13}CO, and C^{18}O 3-2 transition lines are E/k = 33.19 K, 31.73 K, and 31.61 K respectively, whereas the lower energy 1-0 lines are 5.53 K, and 5.29 K for ^{12}CO and ^{13}CO. Brightness temperature values of the source and background are calculated as:

$$T_B = \frac{E/k}{\exp(E/T_{\rm ex}) - 1} \tag{4.2}$$

The excitation temperature and optical depth are calculated by RADEX [76] for input parameters of column density, collider density, kinetic temperature, and line-width. RADEX provides the optical depth at the line centre, but I model the total optical depth through the cloud with a Gaussian profile centred around τ_0 (Equation 4.3), where v_0 is the centre of the line in km s^{-1}, and σ_v is the standard deviation also in km s^{-1}:

$$\tau = \tau_0 \exp\left(-\frac{((v - v_0)^2)}{2\sigma_v^2}\right) \tag{4.3}$$

The temperature of the gas through the cloud accounting for radiative transfer is given by Equation 2.17, producing the line model for CO. Five models are produced for every step in the fit, three for the 3-2 lines and two for the

1-0 lines.

4.1.6 RADEX Parameter Grids

The ^{12}CO, ^{13}CO, and C^{18}O grids were built using molecular line data available from the LAMDA database [68][3], using the radiative transfer code RADEX [76]. RADEX uses the likelihood of a transition between lines to determine the emergent intensity assuming a given set of initial parameters (see Chapter 2). The required parameters are molecule column density, volume density, kinetic temperature, and line width, which was optimized using Bayesian MCMC as described in Chapter 2. To avoid long computation times when running RADEX at each step, I perform a series of RADEX calculations for a reasonable range of input parameters prior to fitting the data. The range of parameters used is given in Table 4.2. I then create grids of excitation temperature and optical depth and use a linear interpolation function to map values of $N_{\rm CO}$, $n_{\rm H_2}$, T_K, $v_{\rm FWHM}$ to values of $T_{\rm ex}$ and τ.

To calculate an output intensity, RADEX requires information about the species abundance relative to H_2, as well as the abundance of ortho- and para-species of the H_2 collider [76]. It is assumed that molecular lines are populated through CO-H_2 collisions, as molecular hydrogen is the dominant molecule in the ISM. As the ratio of ortho-to-para species in the Cygnus X region is unknown, the default is to assume that the species have a 3-to-1 ratio expected from standard H_2 formation on dust grains [76]. The CO to H_2 abundance ratio is taken to be 2×10^{-4}. ^{13}CO and C^{18}O abundance values were set to 1/65 and 1/500th that of ^{12}CO ([56]).

Parameter grids of excitation temperature and optical depth for each species of CO are created from a specified range of values given in Table 4.2.

From the observations of the Cygnus X region, there are 9 telescope pointings. These include 6 distinct low surface brightness clouds identified by eye

[3]http://home.strw.leidenuniv.nl/ moldata/CO.html

Table 4.2: Parameter Ranges for ISM Properties

Parameter	Units	Minimum	Maximum	Number of Points
$\log_{10} N_{^{12}\mathrm{CO}}$	cm^{-2}	13	18.5	21
$\log_{10} n_{\mathrm{H_2}}$	cm^{-3}	3	6	16
$\log_{10} T_{\mathrm{K}}$	K	0.9	2.0	9
v_{FWHM}	km s^{-1}	0.2	5	9

in the ^{12}CO pathfinder data cube. As clouds were extended, three clouds were observed at more than one position. All receptors were fit separately in order to search for small scale variation in cloud parameters. Five parameters are determined through the MCMC fitting routine: column density, hydrogen density, kinetic temperature, ^{12}CO line width, and ^{13}CO line width. The ^{12}CO column density is fit; to adjust the column density of ^{13}CO for the ^{12}CO/^{13}CO abundance ratio, I divided the value of $\mathrm{N}_{^{12}\mathrm{CO}}$ by 65.

4.1.7 Bayesian MCMC with emcee and RADEX

To fit each CO line, Bayesian inference by way of a Markov-chain Monte Carlo method was used. The premise of Bayesian analysis is to determine the probability of some hypothesis given a dataset and initial probability distributions for the parameters. The underlying theorem used is the Bayes theorem (see Equation 4.4: [25]). A best-fit value for each parameter is chosen first by calculating the total probability distribution for the model. In contrast to other methods of fitting data, a single value of a parameter is not given, but rather a probability distribution function from which a parameter value and uncertainty can be ascertained. One can quote the posterior mode, or most common value obtained, the posterior mean of the data, or quote a confidence range or probability content ([25]). In Equation 4.4, the total probability distribution is described in terms of the product of the probability of obtaining the data given the model and prior knowledge of your parameters ($p(D|H_i, I)$, where H_i represents parameters, I priors, and D data) and how probable the model is

given prior knowledge of the data ($p(H_i|I)$). $p(D|I)$ functions as a normalizing factor in this expression.

$$p(H_i|D,I) = \frac{p(H_i|I)p(D|H_i,I)}{p(D|I)} \tag{4.4}$$

A numerical method is typically used to determine the posterior distribution for a model. One such method is the Markov chain Monte Carlo method (MCMC). This process relies on a series of walkers to traverse parameter space as a random walk, recording their path as a chain. However, a walker's next step depends on the last step it took, so it is not entirely a randomized walk through space. The most common algorithm implemented for performing MCMC calculations is the Metropolis-Hastings (MH) Algorithm [25]. The first step for the MH algorithm is to choose a possible future position for a walker from a distribution of possible future positions. This is dependant on the walker's current position. A random deviate between zero and one is chosen. The posterior probability for the model is calculated for both the potential step and the last step. If the ratio of these two probabilities is less than the value of the random deviate chosen, the step is made. If not, the walker remains at its current position. This process is repeated until some level of convergence is reached. That is, that there is very little change in walker position from step to step. This process is performed using the PYTHON package *emcee* [22]. *Emcee* requires a model to fit to the data, and a log-probability function to judge the quality of the fit.

The code I have developed takes the line centres and spectra for the ^{12}CO and ^{13}CO lines, reads in appropriate Gaussian line models for the remaining (3-2) transition lines, and sets up Markov chain walkers in a Gaussian ball around the centre of the known parameter space. The method used is more robust than many CO studies, as normally extragalactic clouds are unresolved,

and therefore only integrated intensity is fit instead of a complete line model. RADEX is then used to fit the integrated intensity only to the known ^{12}CO spectra, instead of fitting full models to each line and multiple lines simultaneously. I have then built a wrapper to combine CO(1-0) and CO(3-2) line spectra and fit the 312 lines present in the data. The required input is a list of Gaussian models, a list of datafiles containing the spectra for each line transition, and parameter grids. The output from *emcee* is a sampler containing the Markov chains from the fitting process.

The log-probability function (see Equation 4.4) used is given by Equation 4.6. The probability of the data given the model, or $p(D|H_i, I)$ in this situation was defined as a product of χ^2 calculations for each line model and spectrum (see Equation 4.5, where d_i represents a CO spectrum and f_i is the model).

$$p(D|H_i, I) = \prod_N \frac{1}{\sigma\sqrt{2\pi}} \Sigma_j \exp\left(-\frac{(d_{i,j} - f_{i,j})^2}{2\sigma_i^2}\right) \tag{4.5}$$

Lognormal prior distributions were included for the column density and kinetic temperature based on the estimated molecular column density for the region calculated using dust and HI observations (see Chapter 5). A lognormal prior was included for the ^{12}CO line-width included from the initial Gaussian fits of each line. For the ^{13}CO line-width, I fit some fraction of the ^{12}CO line with knowledge that the ^{12}CO line-width will always be equal or greater than that of ^{13}CO. Therefore I include a uniform prior for fractional ^{13}CO line-width. Taking the log of the total probability function produces Equation 4.6, which

I use in my fits.

$$\begin{aligned}\mathfrak{L}(\mathrm{T}, \mathrm{n_{H_2}}, \mathrm{N_{CO}}, \mathrm{v_{FWHM}}, \mathrm{f_{13CO}}) \quad = \quad & \\ & -\sum \frac{(^{12}\mathrm{CO}(3-2)_{\mathrm{model}} - ^{12}\mathrm{CO}(3-2)_{\mathrm{data}})^2}{2\sigma^2_{^{12}\mathrm{CO}(3-2)}} \\ & -\sum \frac{(^{13}\mathrm{CO}(3-2)_{\mathrm{model}} - ^{13}\mathrm{CO}(3-2)_{\mathrm{data}})^2}{2\sigma^2_{^{13}\mathrm{CO}(3-2)}} \\ & -\sum \frac{(\mathrm{C}^{18}\mathrm{O}(3-2)_{\mathrm{model}} - \mathrm{C}^{18}\mathrm{O}(3-2)_{\mathrm{data}})^2}{2\sigma^2_{\mathrm{C}^{18}\mathrm{O}(3-2)}} \\ & -\sum \frac{(^{12}\mathrm{CO}(1-0)_{\mathrm{model}} - ^{12}\mathrm{CO}(1-0)_{\mathrm{data}})^2}{2\sigma^2_{^{12}\mathrm{CO}(1-0)}} \\ & -\sum \frac{(^{13}\mathrm{CO}(1-0)_{\mathrm{model}} - ^{13}\mathrm{CO}(1-0)_{\mathrm{data}})^2}{2\sigma^2_{^{13}\mathrm{CO}(1-0)}} \\ & +\mathrm{priors} \end{aligned} \tag{4.6}$$

The log of the probability function for the Markov-chain Monte-Carlo fitting routine calculates the χ^2 value of each model separately. Only one spectrum had $C^{18}O$ lines. Therefore for most lines observed in the data, the $C^{18}O$ spectrum was used as a constraint under the assumption of zero emission. $C^{18}O$ data was fit for the source Cyg X3 only. The optically thick 1-0 lines of CO are not useful in determining column or mass surface density, but ensure that all molecular material is being accounted for in the clouds, as the increased population of these lines ensures that I have a good calculation of excitation temperature.

4.2 Line Fitting

The final fitting algorithm was run with simultaneous fits for $^{12}\mathrm{CO}(3-2)$, $^{12}\mathrm{CO}(1-0)$, $^{13}\mathrm{CO}(3-2)$, and $^{13}\mathrm{CO}(1-0)$ with constraints from the $C^{18}O$ model for 312 lines with 100 walkers each. A 400 iteration burn-in phase was included, and the final product was fit with 1000 steps per walker. I verified convergence of the model graphically by examining the series of chains produced using only 20 walkers, then refit lines by increasing the number of

walkers to 100 to guarantee model convergence. When sampling the posterior parameter distributions, I quoted median, 85th and 15th percentile bounds to characterize the distribution without assuming the final distributions were Gaussian in nature. As the RADEX calculation itself relies on the relationship between column density and volume density, I notice bimodality in many fits, with one having a higher probability. The models will converge with either low column densities and high volume densities, or low volume densities and high column densities. I chose a log-probability cut of 5 from the maximum value obtained to remove lower probability fits with largely different parameter values. A sample of fit lines in CO(3-2) and CO(1-0) is shown in Figure 4.4. Fits of all lines for each receptor in CO(1-0) and CO(3-2) for each of the 9 pointed observations are given in the Appendix. I include a sample of bivariate contour plots in Figure 4.5 and a sample of the typical parameter flatchains sampled with the plot of the probability distribution for the parameter.

In Figure 4.6, I show parameter plots for all lines, with low surface brightness lines identified in red. Initial targets were chosen based on low surface brightness gas identified by eye. Low surface brightness lines were identified for each spectrum as lines with line centres and widths falling within the visually identified channel range. Since much more diffuse gas exists in the Cygnus X area than that directly observed, it is likely that other lines identified as bright may also belong to the quiescent gas category but lie outside of the range specified for a line. Alternatively, the lines may be blended with other brighter lines. Figure 4.6 shows all lines that were fit. There is a clear distinction in the plot of column density and peak ^{12}CO amplitude for faint lines, as we would expect based on their definition. We can see that the low surface brightness lines have a tendency towards higher column densities and lower kinetic temperatures indicating these clouds are denser and colder, as predicted by [23].

The unusual low column clouds also have the largest error bars in all points

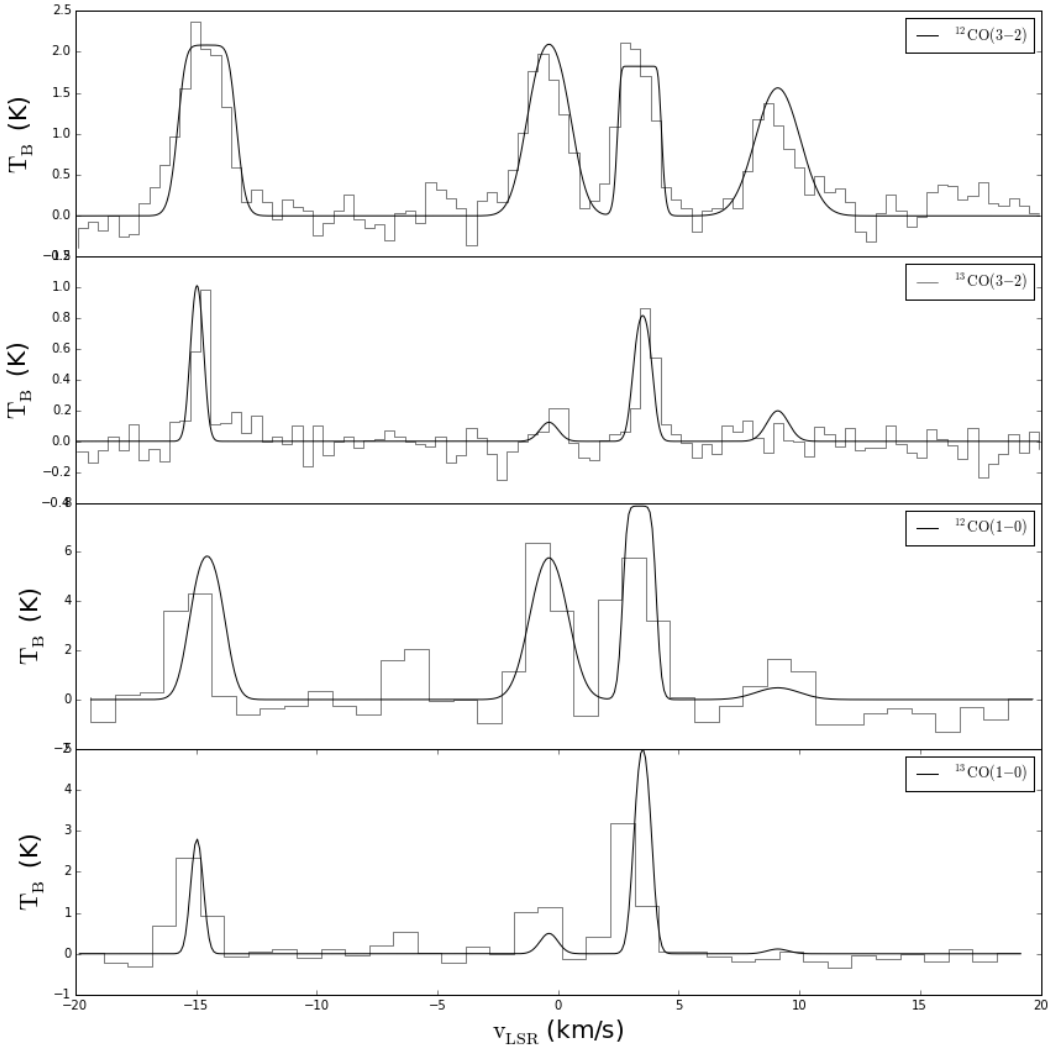

Figure 4.4: Sample spectra taken from observations of Cygnus X1 showing combined fits of each ^{12}CO and ^{13}CO 3-2 line (top two figures) and 1-0 line (bottom two figures).

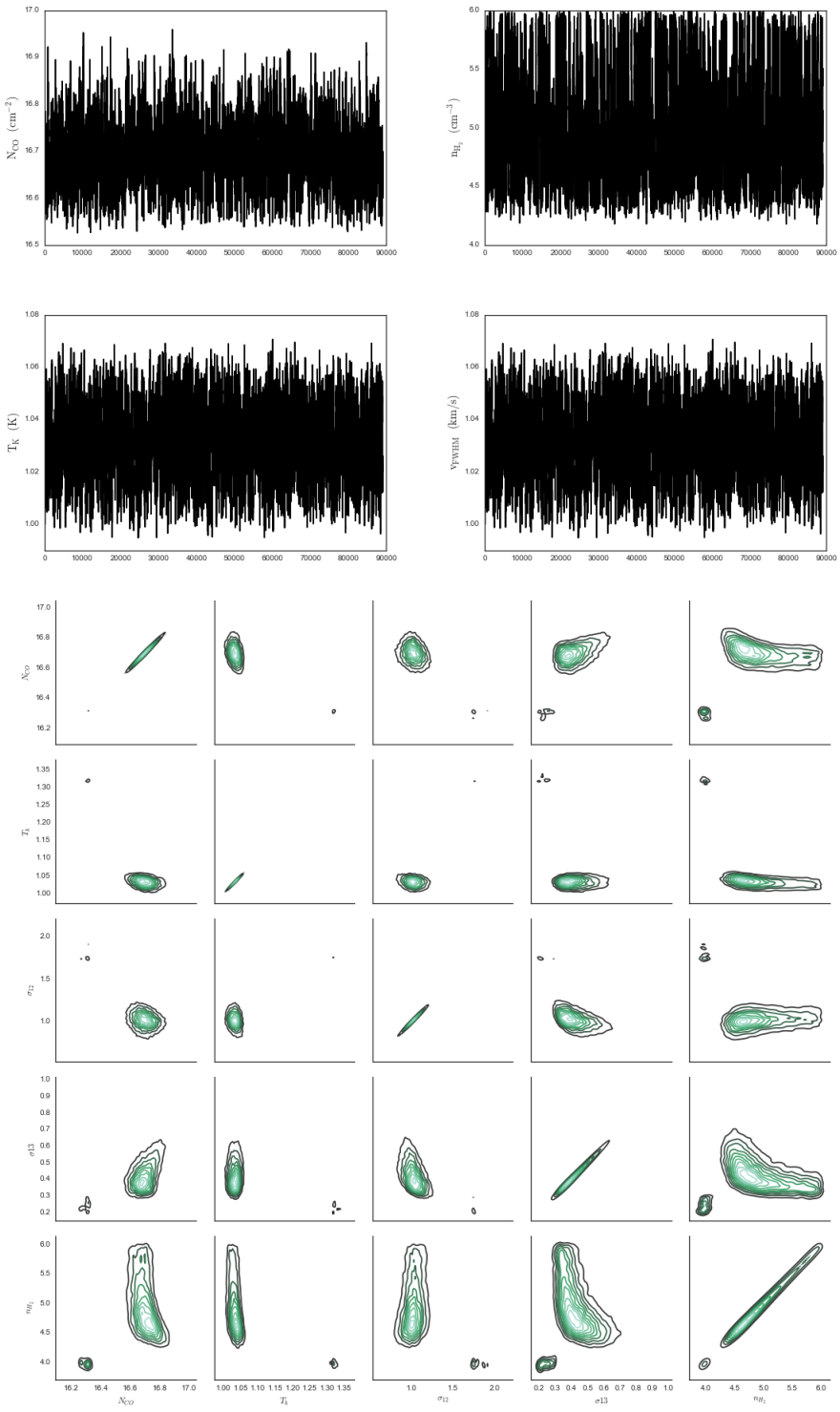

Figure 4.5: (top) Markov-chains for a fit of a spectral line after taking most probable solutions. (bottom) Sample parameter contour plot for the same fit, without the cutoff in logprobability. We see bimodality for some parameters, or locations of high density in more than one area of plots.

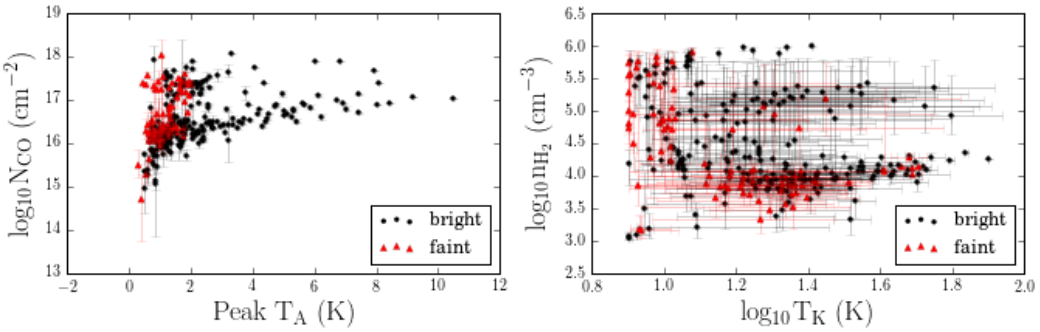

Figure 4.6: Model parameters for all 312 lines. The top two and centre left plots show fit parameter versus line width, the centre right plot shows column density vs volume density where the slope would be the length scale of the cloud, the bottom left plot shows column density as a function of kinetic temperature showing the characteristic cold temperatures of the low surface brightness clouds, and the bottom right plot shows the column density as a function of peak corrected antenna temperature.

below 10^{17} cm^{-3}. I examined channel maps along the line of sight of these particular lines, and found that these lines are often not a part of a bright cloud at all, but an anomalous area of bright noise that may have been mistaken for a line during the initial Gaussian fitting process. Many of them were also not present in the CO(1-0) line data, which have a much lower resolution. This is aphysical as large clouds should still contain the emission. To test the hypothesis that these lines are anomalous bright noisy patches, I smoothed the ^{12}CO data to 45″ resolution to match the CO(1-0) data and resampled spectra at the same location. Most of these anomalous lines disappeared. Due to the nature of this problem, the line width for the ^{12}CO and ^{13}CO data were often drastically different, which should not be the case for true extended structure. I therefore excluded data points for which the fitted line widths differed by more than 0.5 km s^{-1} in ^{12}CO and ^{13}CO. This constraint alone removed most of the anomalous data. The lowest column density lines present in the plots belong to lines that were not detected in ^{13}CO. I fit the ^{13}CO spectra for these non-detections to eliminate the possibility that a faint line was present but not

detected by eye. The plots in Figure 4.7 show only lines with both a ^{12}CO and ^{13}CO(3-2) detection and differences in line widths within 0.5 km s^{-1}, and applying a column density lower limit of $10^{16.8}$ cm^{-2}.

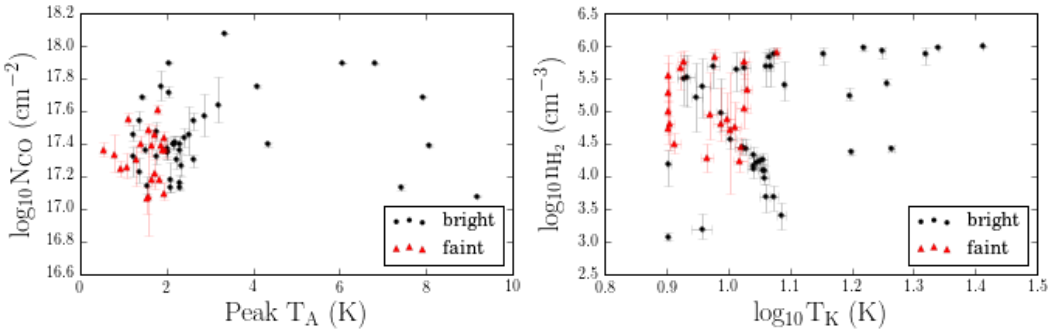

Figure 4.7: Model parameters for lines after constraints were applied. Plots contain no lines where the ^{12}CO and ^{13}CO lines widths differ by more than 0.5 km s^{-1}, and no lines where no ^{13}CO is detected. The plot on the left shows the volume density as a function of kinetic temperature, demonstrating the characteristic cold temperatures of the low surface brightness clouds. The bottom right plot shows the column density as a function of peak corrected antenna temperature.

The molecular hydrogen volume densities observed are within expected ranges for this region, as ^{12}CO and ^{13}CO(3-2) require densities of at least 10^3 to excite. In regions of high density molecular material densities of 10^4 are expected[4]. I further calculated an expected column density for the region using estimates from Herschel [55] and CGPS [74] surveys along the line of sight of one of the observations closest to DR21. The dust column density from Herschel provides us an estimate of total hydrogen mass of the region using a dust-to-gas ratio. The total amount of hydrogen is 7×10^{21} cm^{-2}. To determine what fraction of this we would expect from the molecular component, I determined the atomic component using HI line emission data from archival CGPS observations. Atomic hydrogen column density can be determined from producing a background subtracted absorption spectrum along the line of sight

[4]Based on calculations of critical density, $n_{CR} = A/\gamma$, with A and γ representing Einstein coefficients obtained from [68].

of a bright background continuum source. As DR21 is close in proximity to the ^{13}CO observations and is background to most of the emission along the line of sight, I used it as the continuum source. Integrating the source and background emission spectrum using $N_H = \int \tau[1 - \exp^{-\tau}]^{-1} T dv$ over the velocity range of the clouds provides us with a good estimate of atomic gas column of 6×10^{21} cm^{-2}. Subtracting this from the total dust column and dividing by two gives an estimate of 1×10^{17} cm^{-2} for the molecular material. This measurement is consistent with our determination from CO lines.

4.2.1 Mass Determination

To determine the mass of each cloud complex from the column density, I match individual lines to clouds in the object identification maps made for the bright and faint gas components. For each spectral line, I formed a subcube from one of the three object maps (bright gas at negative velocities, bright gas at positive velocities, and low surface brightness gas) with spatial limits set by the HARP footprint, and spectral limits defined by the line centre after adding and subtracting σ_v in the spectral axis. Any numbered clouds within this region are associated with a particular spectral line.

As there are many associations with the same cloud, and in particular the clouds that occupy the largest surface area, I take the mean of the column density of all lines associated with it to represent the column density of each cloud. Any clouds without an observation are assigned a mean column density from all other clouds observed within the boundaries of the object map. For each cloud identified, I also calculated a surface area in pixels by first masking all other emission in the dataset apart from the cloud in question, summing over the spectral axis, and counting the number of non background pixels. As we have approximate distances for each of the three cloud components, I can convert square pixel area to square parsec area for 7.5″ pixels. The mass of any individual cloud is then simply the multiplication of the column density, the

CO abundance ratio, the mean particle mass in molecular gas ($\mu = 2.4\ m_H$), and the surface area of the cloud.

In Figure 4.8 and Figure 4.9 , I show surface density maps for each component. The surface density of a cloud was added to each pixel within the boundaries of the cloud defined by its area on a 2D map. Pixels with multiple overlapping clouds have a summed surface density value. These images show the variation in mass over the Cygnus X region.

Mass estimates for extragalactic star formation rate will also be given using the standard mass-to-light ratio known as X_{CO} discussed in Chapter 2. Using this method, integrated intensity values are converted directly into column density. Usually this is the method used for extragalactic sources where individual clouds are not resolved.

In Table 4.3, I show the total mass calculated for each gas component calculated using the column densities and surface areas fit in the analysis above as well as the traditional method of using the total integrated intensity from the moment maps of each region and the standard value of X_{CO}. The uncertainty values for masses include statistical uncertainty only, therefore are quite small as I used maser distance values to two of our regions that are very certain.

In Table 4.4, I show the total mass component of W80 calculated for the bright and faint gas. Faint gas is 43 percent of the total gas mass of the region.

In Table 4.3 the total mass of faint gas is much less than that of bright gas. However distance plays a huge factor in this calculation. As the low surface brightness gas is much closer, we survey a smaller surface area of the sky. I therefore calculated the total surface density of each component and scaled this density by an area of 500 pc^2 for each component. In a 500 pc^2 region of space, faint gas makes up $8.4 \times 10^3\ M_\odot$, whereas the combined mass of all the gas is $37.8 \times 10^3\ M_\odot$ indicating the low surface brightness clouds make up 22% of the mass component of the Cygnus X region as calculated from the spectral fit results. Performing the same calculation using the masses derived using the

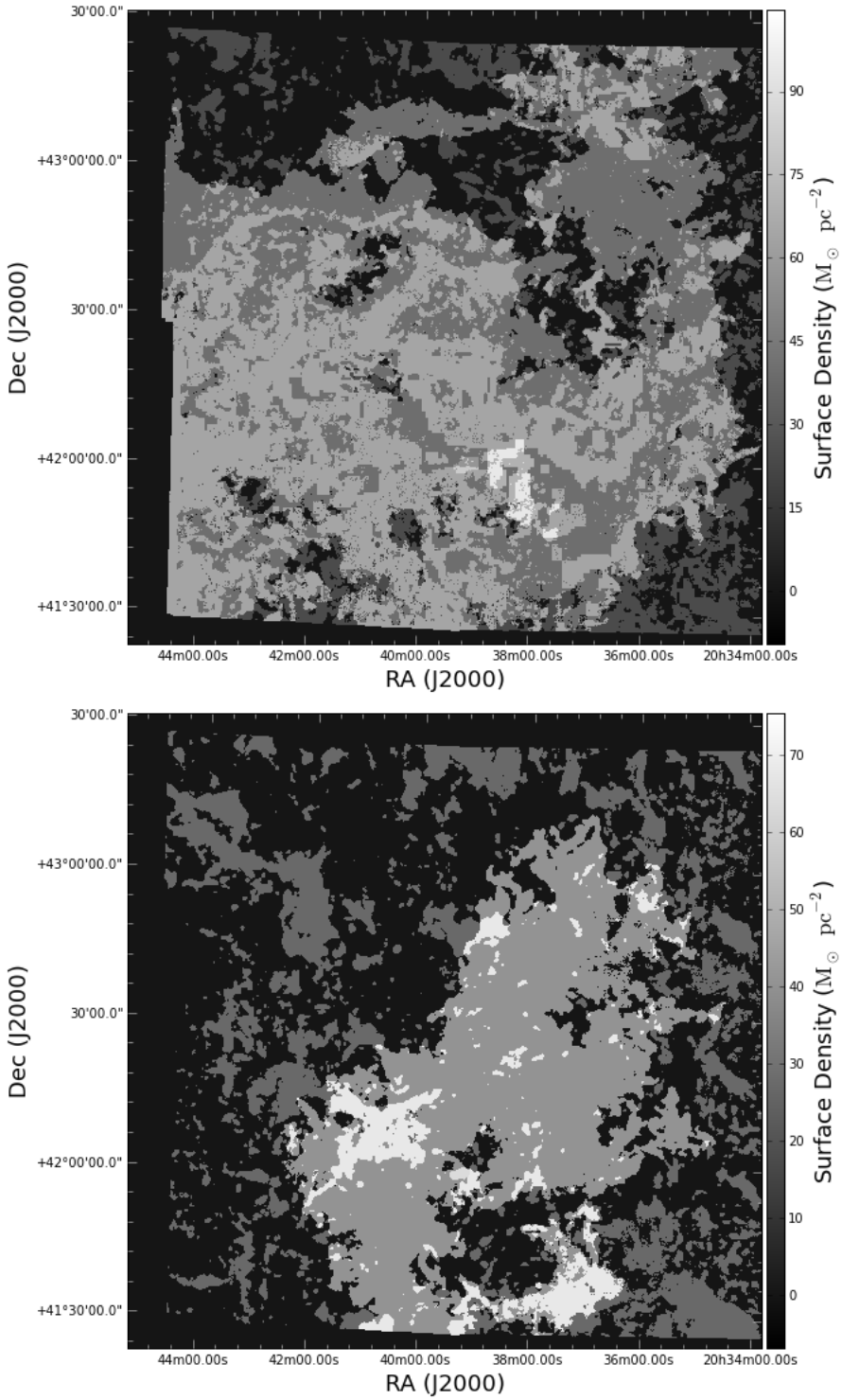

Figure 4.8: Cygnus X surface density maps for bright gas at positive (top) and negative (bottom) velocities creating using masses derived from CO line models.

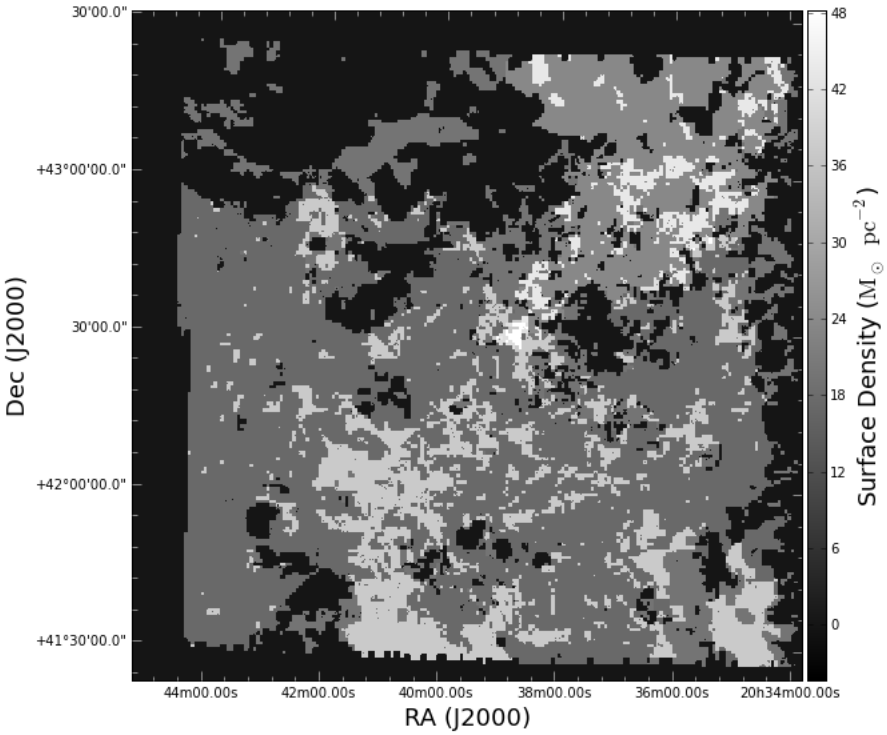

Figure 4.9: Cygnus X surface density maps for faint gas using masses derived from CO line models.

Table 4.3: Total masses of cloud regions calculated using X_{CO} and through spectral fitting of lines for Cygnus X.

Component	Method	Mass (10^3 M$_\odot$)	σ_M (10^3 M$_\odot$)	Area (pc^2)	Distance (kpc)	σ_D (kpc)
Faint	Spec Fit	9.4	2.5	559	0.65	0.15
Positive	Spec Fit	82.2	0.2	2082	1.30	0.07
Negative	Spec Fit	53.4	0.3	2772	1.50	0.08
Faint	X_{CO}[a]	11.968	0.015	559	0.65	0.15
Positive	X_{CO}[a]	89.796	0.054	2082	1.30	0.07[b]
Negative	X_{CO}[a]	80.688	0.058	2772	1.50	0.08[b]
Faint	X_{CO}[c]	7.420	0.010	559	0.65	0.15
Positive	X_{CO}[d]	46.696	0.049	2082	1.3	0.07[b]
Negative	X_{CO}[d]	41.960	0.064	2772	1.50	0.08[b]

[a]Standard value of X_{CO} corrected from 3-2 to 1-0 line using intensity ratio for respective lines of 0.4.

[b]Statistical error only.

[c]$X_{CO(3-2)} = 3.1 \times 10^{20}$ calculated in section 4.2.2 for faint gas.

[d]$X_{CO(3-2)} = 2.6 \times 10^{20}$ calculated in section 4.2.2 for bright gas.

Table 4.4: Total masses of W80 cloud regions calculated using X_{CO}. Uncertainties include statistical errors only.

Component	Method	Mass (10^3 $M_\odot$)	σ_M (10^3 $M_\odot$)	Area (pc^2)	Distance (kpc)	σ_D (kpc)
Faint	X_{CO} [a]	10.965	0.009	1205	0.6	0.2
Bright	X_{CO} [a]	23.279	0.011	1205	0.6	0.2
Faint	X_{CO} [b]	6.798	0.006	1205	0.6	0.2
Bright	X_{CO} [c]	12.105	0.008	1205	0.6	0.2

[a] Standard value of X_{CO} corrected from 3-2 to 1-0 line using intensity ratio for respective lines of 0.4.

[b] $X_{CO(3-2)} = 3.1 \times 10^{20}$ calculated in Section 4.2.2 for faint gas.

[c] $X_{CO(3-2)} = 2.6 \times 10^{20}$ calculated in Section 4.2.2 for bright gas.

integrated intensity maps and X_{CO}, we see the faint gas component makes up 23% of the final mass calculation. The same calculation for the bright and faint gas in the W80 region yields a far different result. The W80 region shows that 43% of its mass is in a low surface brightness component. Much of this may be due to distance assumptions for the gas, as the bright gas in Cygnus X is located in the background of the region and is not directly interacting with the low surface brightness component, whereas in the W80 region the bright and faint gas is assumed to be located at the same distance. The latter would make the contribution of the faint cloud component higher. The fractions of luminosity are much lower (Chapter 3) indicating low surface brightness gas makes up a smaller luminosity fraction than mass fraction. This fits with their nature of extended, faint, high density clouds.

4.2.2 Conversion Factor

In Figure 4.10 I plot column density versus integrated flux for the lines defined as $W(^{12}CO(3-2)) = \int T_{MB}\, dv$, which is frequently used to calculate column density and mass as described in Chapter 2. The slope of this line is the CO-to-H_2 conversion factor in Equation 2.1. The standard Galactic value is $X_{CO} = 2 \times 10^{20}$ cm^{-2}(K km/s)$^{-1}$ for the 1-0 transition of CO [7]. In Fig-

ure 4.10, the lines showing the calculated value of $X_{\rm CO}$ are calculated for the faint and bright gas from the median ratio of $N_{\rm H2}$ and $W_{\rm CO}$.

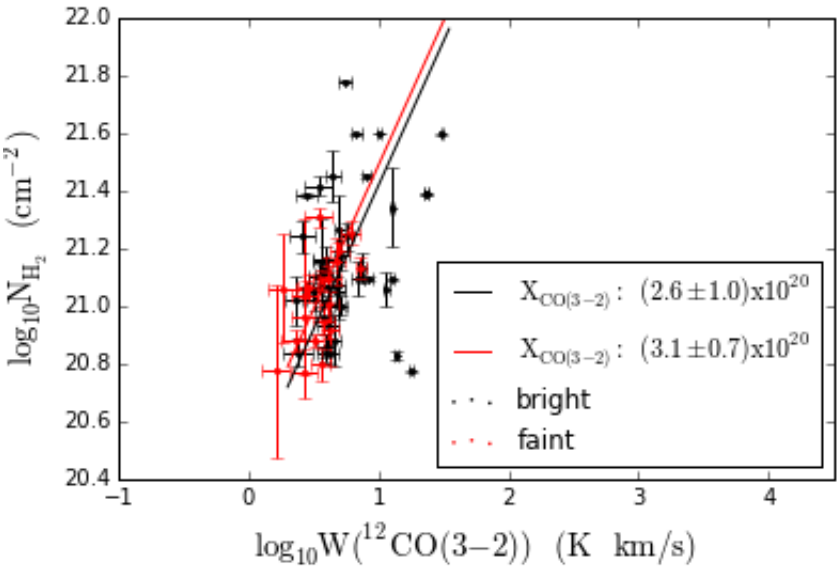

Figure 4.10: Calculation of CO-to-H_2 conversion factor in bright (black) and faint (red) clouds. The bright clouds are a combination of gas at positive and negative velocities. Error bars shown are 1σ values quoted for each parameter. Uncertainty in $X_{\rm CO}$ is the median absolute deviation.

The conclusion that we can draw from these values is that there is not a significant difference in physical conditions between the low surface brightness clouds and the rest of the gas and that they are a relatively low mass fraction.

Chapter 5

The Contribution of the Faint Gas Component to the Star Formation Law

In this chapter, I discuss the calculation of the star formation rate, as well as the relationship between star formation rate and the surface density of molecular gas for both the W80 and Cygnus X region. The star formation rate is the mass of stars formed per square kiloparsec per year projected on the sky, and is difficult to quantify. Young stellar objects (YSOs) are typically embedded in dense, dusty molecular clouds obscuring them from view, even within the Milky Way [31]. This makes any sort of measurement of star formation rates from counting the number of YSOs in all but the nearest regions impossible. High mass stars, such as O and B type stars, ionize the region around them, and blow out a cavity in the interstellar medium. These are referred to as HII regions, and can extend to sizes of several hundred parsecs if multiple stars were formed together. These regions are bright and visible even in distant galaxies in H_α (656.3 nm, Balmer series $n = 3$ to $n = 2$ transition). From models of the initial mass function, or the number of stars produced as a function of mass, observations of HII regions as tracers of high mass star formation rate can be

used to calculate the total star formation mass in a region. We also know the amount of time stars of certain masses will spend in each stage of formation, with the formation of HII regions only representing the very last stages of high mass star formation. I can therefore infer the rate of star formation from the intensity of emission from HII regions, as described below. For nearby star forming regions, star formation rates can be calculated using the more direct method of counting YSOs. YSOs are observable in infrared for all stages of star formation. Since the tracer of star formation (e.g., H_α intensity vs YSO counting) may be a factor driving the differences observed in Galactic and extragalactic clouds, and therefore we explore both tracers used in Galactic and extragalactic studies for the Cygnus X region, and tracers of Galactic star formation for W80.

5.1 Extragalactic Star Formation Rate

The extragalactic star formation rate is derived using a combination of H_α maps from the Wisconsin H_α Mapper Survey [27], and the Virginia Tech Spectral-Line Survey (VTSS) [17] after having been corrected for continuum sources. Using this method, we assume that all emission is coming from ionizing photons produced from recent high mass star formation [43], and that a known initial mass function allows us to extrapolate this to all star formation in the region. Dust along the line of sight will absorb some of the ionizing photons, and therefore the star formation rates calculated from H_α needs to be corrected for extinction. This can be done using infrared emission at 24 microns as described by [43]. I use 24 micron emission from *Spitzer* to calibrate the data. Light in this wavelength represents star formation not represented in Hα due to extinction. The equation that describes the method I use for producing a star formation rate from a linear combination of 24 micron and H_α maps is given by Equation 5.1 [43]. The relationship between star formation rate and

H_α emission is derived using models of stellar IMF in [8] and [50].

$$\Sigma_{SFR} \quad = \quad 634\ I_{H\alpha}[\mathrm{erg\ s^{-1}sr^{-1}}] + 0.0032\ I_{24\mu m}[\mathrm{MJy\ sr^{-1}}] \tag{5.1}$$

For the Cygnus X region, the H_α and Spitzer 24 (hereafter S24) micron images are given in Figure 5.1. Both the S24 image and the H_α image were resampled to match the CO data using the *Starlink* tool *wcsalign*. This tool takes in the world coordinate system (WCS) information from a supplied reference image, in this case the pathfinder integrated intensity map. The default sampling method uses a 'sincsinc' kernel to resample pixels from the input image. The result is a cut from the original image that will be a pixel-to-pixel match of the output image in the same coordinate system. As I am sampling over large areas and the H_α image is a blend of two different resolution images, I did not smooth the three images to a common resolution.

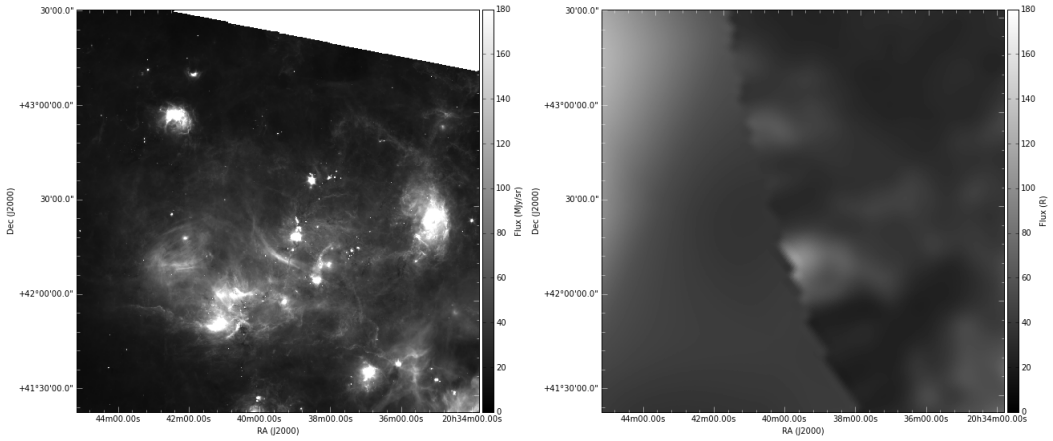

Figure 5.1: Spitzer MIPS 24 μm cutout matching CO(3-2) pathfinder map (left) and WHAM Hα map of same region.

5.2 Galactic Star Formation Rate

The Galactic star formation rate calculation is direct, as we count the number of YSOs of Class 0/I and flat spectral index in both regions. Class 0/I YSOs show a characteristic 'rising' sed. Flat spectrum YSOs are the stage in evolution between Class I and Class II represented by a 'flat' sed. Catalogues of YSOs are provided by [36] and [26] for Cygnus X and W80 respectively. Both authors define Class using the infrared excess of each YSO, by which they identify 'rising' spectrum SEDs as $\alpha > 0.3$ and 'flat' spectrum SED as $-0.3 < \alpha < 0.3$. These are the two earliest stages of star formation, both of which contain envelopes with in falling material onto the central YSO.

It is not possible to have a uniform sample of stars from all parts of the initial mass function, so an assumption has to be made about the mass and lifetimes of the stars being observed. The calculation I use follows Equation 5.2 (e.g., [31]). The mean rate of star formation is equal to the number of YSOs of a certain age, multiplied by the mean star mass and dividing by the time the stars spend in the stage being considered. I use a standard assumption of $\langle M_* \rangle = 0.5\ M_\odot$ from IMFs (Salpeter).

$$\langle \dot{M}_* \rangle \quad = \quad \frac{N(\mathrm{YSOs}) \langle M_* \rangle}{t} \tag{5.2}$$

I use an elapsed time t for Class 0/1/flat YSOs of 0.98 Myr, the average calculated using the range in lifetimes for the clouds of the Gould belt [19].

I derive the Galactic star formation rate using a published list of protostars with their given classification of Class 0/I, flat, or II protostars. To compare these YSO populations to those of W80 for which no list of Class II YSO is readily available, I use Class 0/I and flat YSOs only.

5.2.1 Cygnus X

I identified all protostars associated with clouds in the Cygnus X region. The region itself extends for a significant portion of the galaxy, and therefore I did not make the assumption that all protostars were located at the same distance. Each protostar was matched with clouds of all three cloud regions along its line of sight. I determined associations of YSOs with Bolocam Galactic Plane Survey (BGPS) [59] point sources with known velocity peaks[1] to improve cloud association as most YSOs could be identified with multiple clouds in all three datasets. I also looked at the correlation between the published YSOs and coordinates for outflows listed by [23]. This allowed for definitive cloud association for 26 of the published YSOs. The remaining YSOs were weighted by the number of clouds they could be identified with, and this fraction was assigned to each cloud. I was able to produce YSO count maps for Class 0/I and flat YSOs separately for each of the three regions at different distances as well as star formation rate maps weighed by cloud area for a direct comparison to the surface density carbon monoxide map. This allows for an easier study of variation in Class 0/I and flat star formation rate throughout the region.

Class 0/I and flat YSO maps are shown in Figures 5.2 through 5.3. The surface density calculation uses Equation 5.3, which compares the number of YSOs per unit area A divided by the lifetime of Class 0/I and flat $T_{0/I}$ and flat t_f YSOs.

$$\Sigma_{\rm SFR}\ (\rm M_\odot\ yr^{-1}\ kpc^{-2}) \quad = \quad \frac{N_{\rm YSO}}{t_{0/I/f}\ Area}(0.5 M_\odot) \tag{5.3}$$

The expression is then multiplied by 0.5 $\rm M_\odot$ for a typical YSO in Class 0/I or flat sed. The result is a rate of YSO production from a count of Class 0/I and flat YSOs per unit area. The cloud YSO surface density plots were made

[1]Peak matching completed by Tomas Robinson.

by taking the total number of YSOs for a cloud and dividing by the surface area of the cloud. The area is determined by the number of pixels in a region multiplied by a conversion factor to turn a square pixel value into a square kiloparsec value depending on the distance. All protostars and clouds in the same cloud region are assumed to be at the same distance for simplicity.

In Figure 5.2 and Figure 5.3, I show the moment maps of all three regions with YSOs identified by Class. YSOs marked with an X are those that had no positive Bolocam or outflow identification, and those with diamonds have a positive identification. One of the concerning features of these maps is the high probability of association of protostars with the low surface brightness clouds. The reason for this comes back to the nature of the faint gas itself. If a YSO has no association with a dust source, it has to be assigned to every cloud along that line of sight. By definition, the diffuse clouds have a high surface area, but extend through only a few spectral channels. Therefore it is more likely for a YSO to be spatially identified with a low surface brightness cloud, even if the true association is unlikely. From the few YSOs with definite cloud associations, we see that only 3 belong to the low surface brightness clouds, and do not overlap the main faint gas component. From the pattern of the Class 0/I YSOs, it seems likely that most of the unidentified sources belong to the bright gas associated with DR21. I use the known and total YSO population plots as lower and upper limits on the Galactic star formation rate.

5.2.2 W80

In Figure 5.4 I present a complete map of all [26] YSOs overlapping the bright and faint gas, and in Figure 5.5 and Figure 5.6, I show YSOs associated with specific clouds of W80 separated by Class 0/I and flat spectrum YSOs for the bright and faint gas moment maps.

The star formation rate is calculated using Equation 5.3. Unlike the Cygnus X region, there is no evidence of a separation of the bright and faint gas in

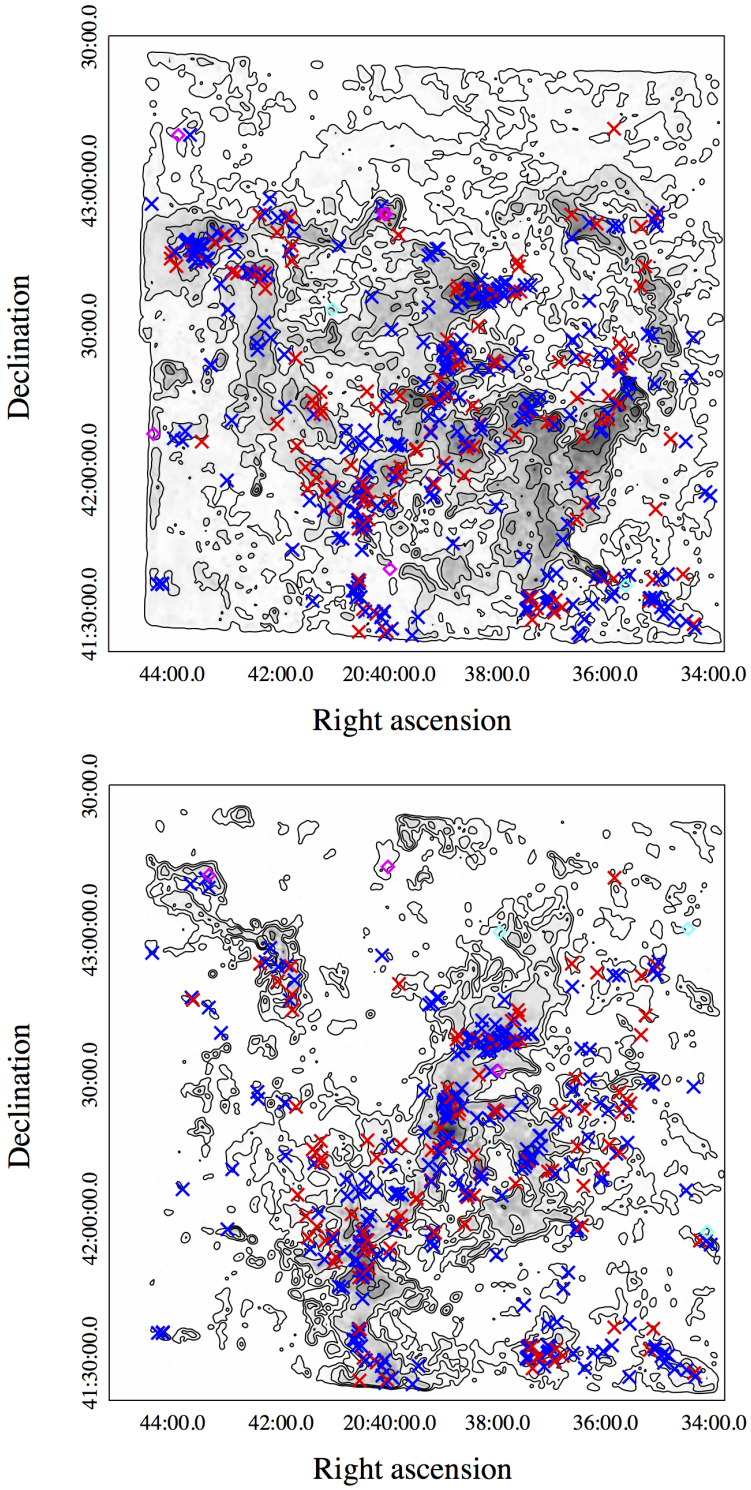

Figure 5.2: Integrated intensity maps showing overlapping YSOs for the bright positive (top) and bright negative gas (bottom). Diamond shapes indicate YSOs identified with dust peaks with magenta representing flat spectrum sources and cyan representing Class 0/I sources. Diagonal crosses indicate YSOs with multiple possible clouds associations with red representing flat sources and blue representing Class 0/I sources.

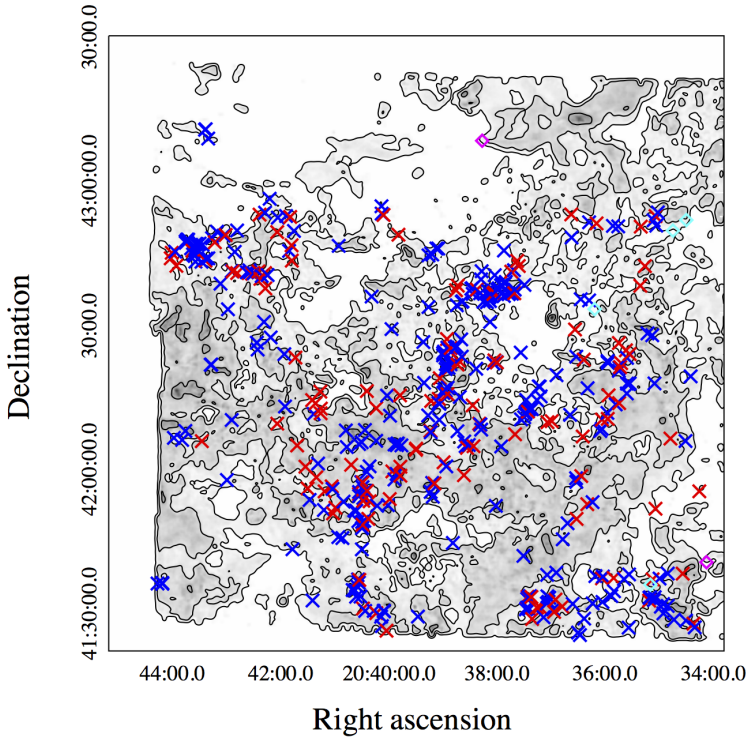

Figure 5.3: Integrated intensity maps showing overlapping YSOs for the diffuse gas. Diamond shapes indicate YSOs identified with dust peaks with magenta representing flat spectrum sources and cyan representing Class 0/I sources. Diagonal crosses indicate YSOs with multiple possible clouds associations with red representing flat sources and blue representing Class 0/I sources.

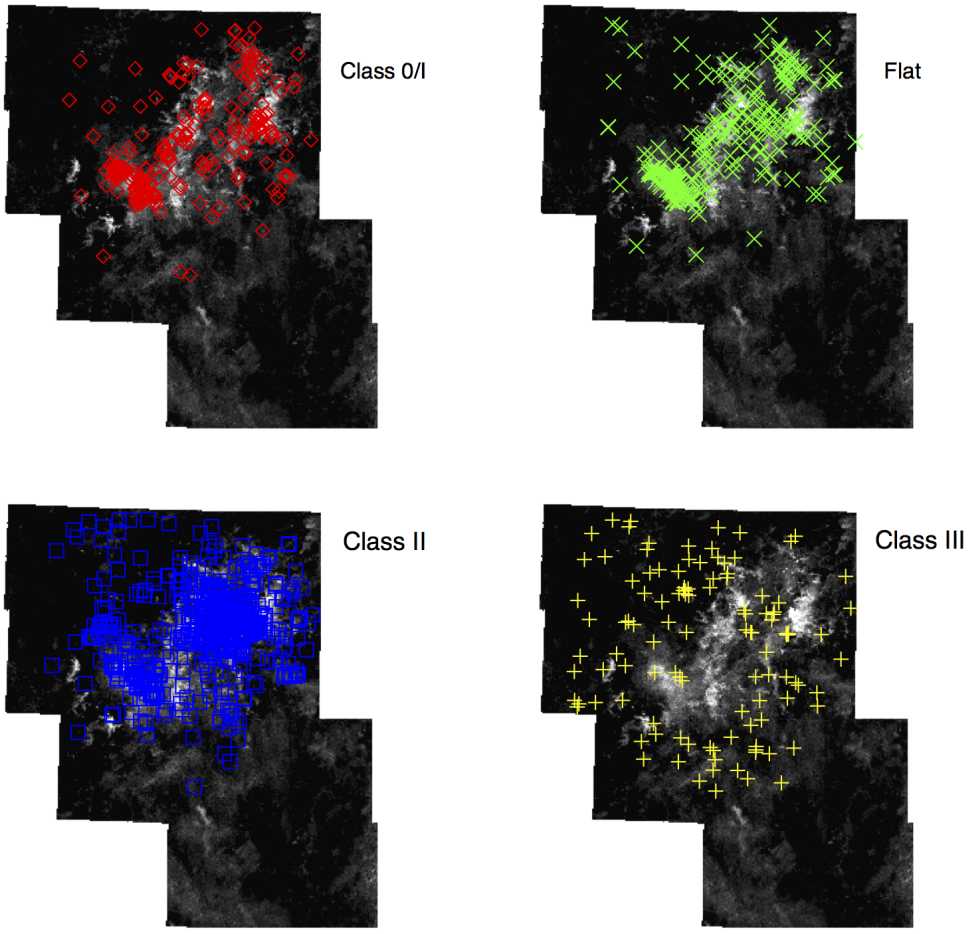

Figure 5.4: Distribution of YSO objects in the clouds of W80. Markers are plotted on the moment 0 map of all gas in region.

velocity space and therefore I assign all gas a common distance of 600 pc and calculate surface area accordingly.

5.3 Comparing Tracers of Star Formation for Bright and Faint Gas

I present the plots of star formation rate and molecular gas surface density using Galactic and extragalactic tracers in Figure 5.7. Because we have no 24 μm map of W80, extragalactic plots show the Cygnus X region only, but Galactic

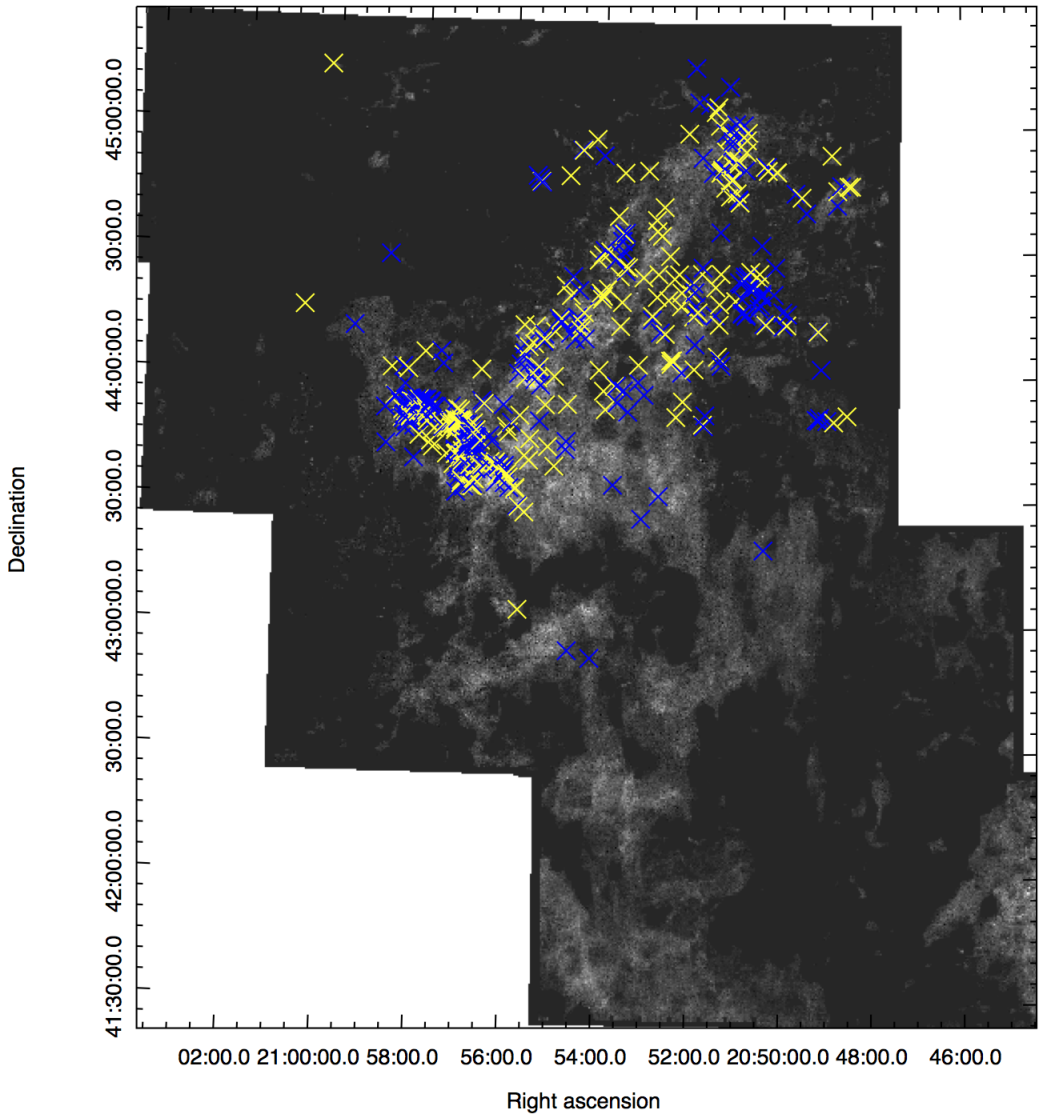

Figure 5.5: Distribution of Class 0/I and flat spectrum YSOs on the moment 0 maps of faint gas of the W80 region. These maps show YSOs that are known to be associated with the region (diamonds) and those which have a possible association with the clouds of the region (diagonal crosses). Blue and cyan represent flat sed sources, while red and yellow represent Class 0/I objects.

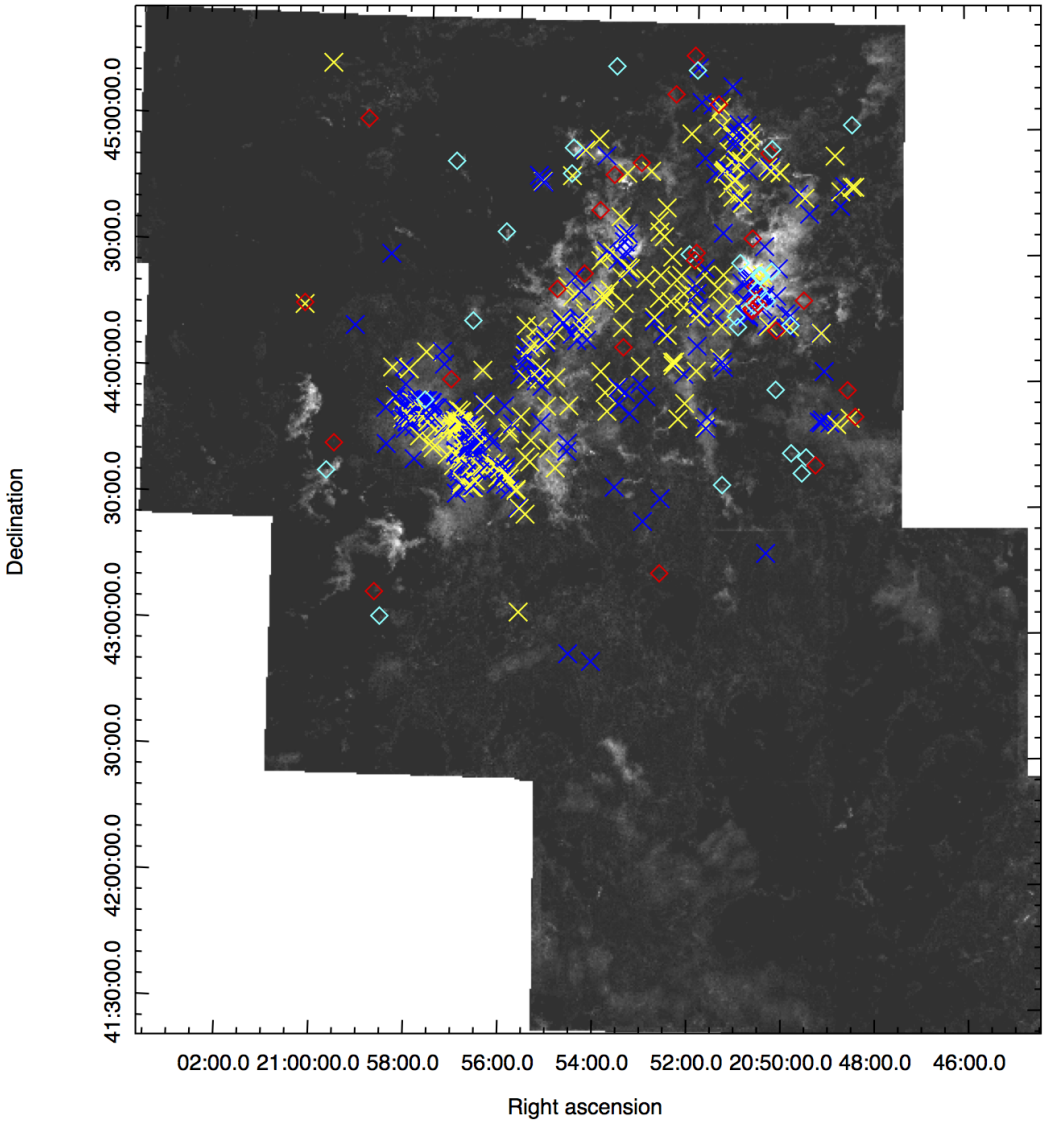

Figure 5.6: Distribution of Class 0/I and flat spectrum YSOs on the moment 0 maps of bright gas of the W80 region. These maps show YSOs that are known to be associated with the region (diamonds) and those which have a possible association with the clouds of the region (crosses). Blue and cyan represent flat sed sources, while red and yellow represent Class 0/I objects.

star formation rate plots shows both W80 and Cygnus X data. Plots show bright star forming clouds only, and the effect of adding low surface brightness gas to the equation. From these plots we see that the inclusion of low surface brightness gas provides a closer fit to the Kennicutt relation, but still is not enough to completely match the data to what is seen in extragalactic systems. Both the Galactic and extragalactic plots are quite far from the [44] relation describing molecular gas instead of the Kennicutt-Schmidt relation for both molecular and atomic gas. I note that the KS relation was calculated here without the HI gas component.

It is immediately clear that the two star formation tracers are not equivalent, with the Galactic star formation tracer showing consistently higher star formation rates than its extragalactic counterpart. In Figure 5.8 I show the two tracers plotted against each other to show this large (factor of 3) discrepancy. This indicates that the deviation between star formation rate and molecular gas mass may be more closely tied with the tracer used than previously thought.

5.3.1 Effects of Sampling

To ensure that the sampling area is not affecting the overall calculation of star formation rate, I split both the map of star formation rate and the map of surface density into grids of different sizes. I sampled on images split into $2^\circ \times 2^\circ$, $1^\circ \times 1^\circ$, $30' \times 30'$, and $15' \times 15'$ square regions. Within each box, the mean surface density star formation rate and mass surface density are calculated. This is done for the bright gas component alone, then the sum of the bright and faint gas components. I included lines representing the Kennicutt-Schmidt relation defined by the Equation $\sum_{\rm SFR} = 2.5 \times 10^{-4} \sum_{H_{\rm gas}}^{1.4}$ [32] assuming minimal contribution from atomic gas such that $\sum_{\rm H_2} = \sum_{\rm gas}$, and the relation $\sum_{\rm SFR} = 4.54 \times 10^{-4} \sum_{\rm H_2}^{1.0}$ from [44]. Plots for each combination of tracer are included.

For the Galactic star formation rate, I used the same mass surface density

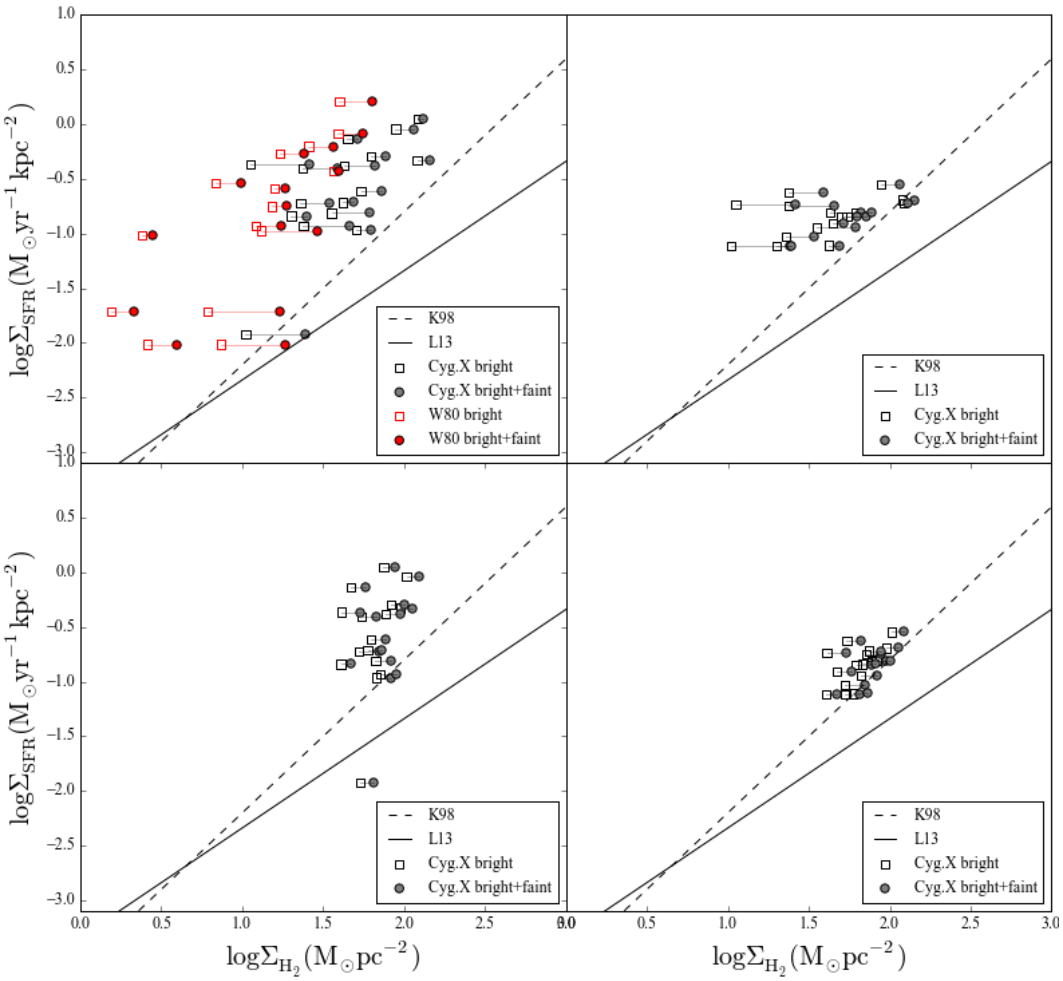

Figure 5.7: Calculation of Galactic star formation rate (top left) and extragalactic star formation rate (top right) using X_{CO} values calculated from spectral fit values in Chapter 4. Lower plots show Galactic (left) and extragalactic (right) star formation rate with mass calculated using cloud surface density maps created from spectral fits and cloud associations. W80 points are included for Galactic plot only. Kennicutt-Schmidt relation is shown by the dashed line following [32], and Leroy solid line refers to molecular gas fit given in [44].

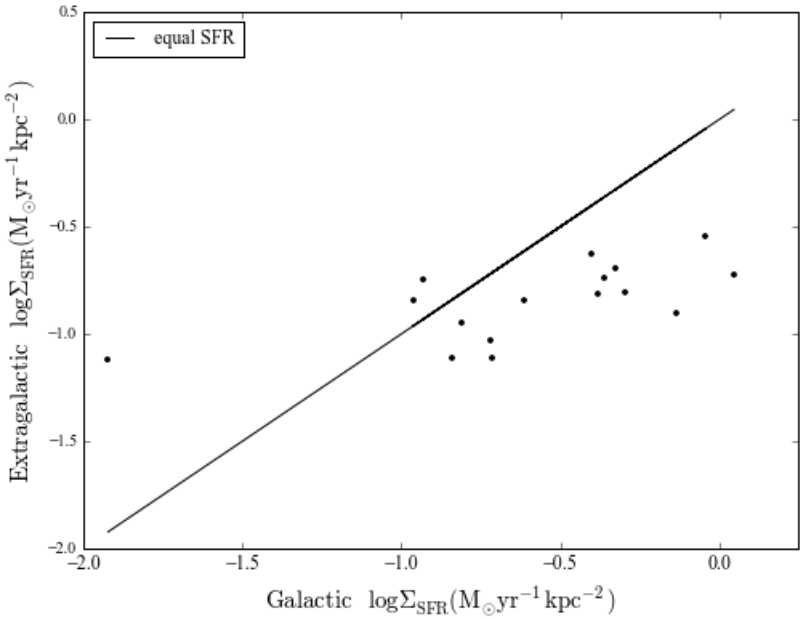

Figure 5.8: Comparison of Galactic and extragalactic star formation tracers for Cygnus X.

plots and maps of YSO position to derive the surface density of star formation. I sample both images with 1×1, 2×2, 4×4, and 8×8 box sizes and use Equation 5.3 to calculate the surface density of star formation. The final results are given in Figure 5.11.

5.4 Discussion of Star Formation Rates

The inclusion of faint gas corrects the plots of star formation rate versus molecular gas surface density towards the Kennicutt-Schmidt relation for both extragalactic and Galactic tracers. Thus, we can confirm the low surface brightness gas as a significant contributor of mass in Galactic and extragalactic studies. However, a discrepancy still remains between the derived SFRs. The difference in Galactic and extragalactic tracers shows that the star formation rate is on average over 2 times higher using Galactic rather than extragalactic tracers for

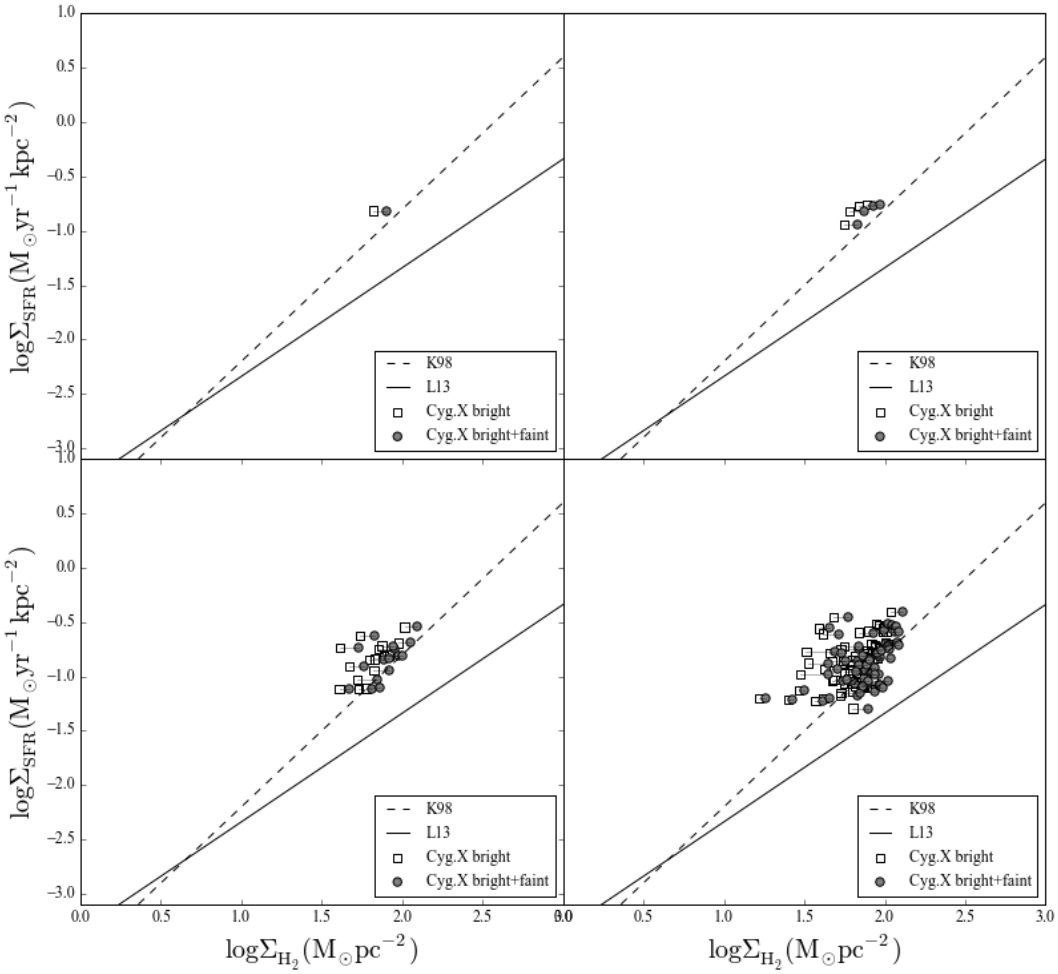

Figure 5.9: Rate of star formation and mass surface density relation for bright gas only (boxes) and bright and faint gas (circle). Plots are made using extragalactic tracers of star formation rate. The mass is calculated using the surface density plots created from spectral fits. The dashed black line shows the Kennicutt-Schmidt relation [32]with a power law index of 1.4, and the solid line shows the relation from [44] with an index of 1. Surface density images were split into a $2^\circ \times 2^\circ$ box (top left), $1^\circ \times 1^\circ$ boxes (top right), $30' \times 30'$ boxes (bottom left), and $15' \times 15'$ square boxes (bottom right) and mean surface densities were calculated for each box.

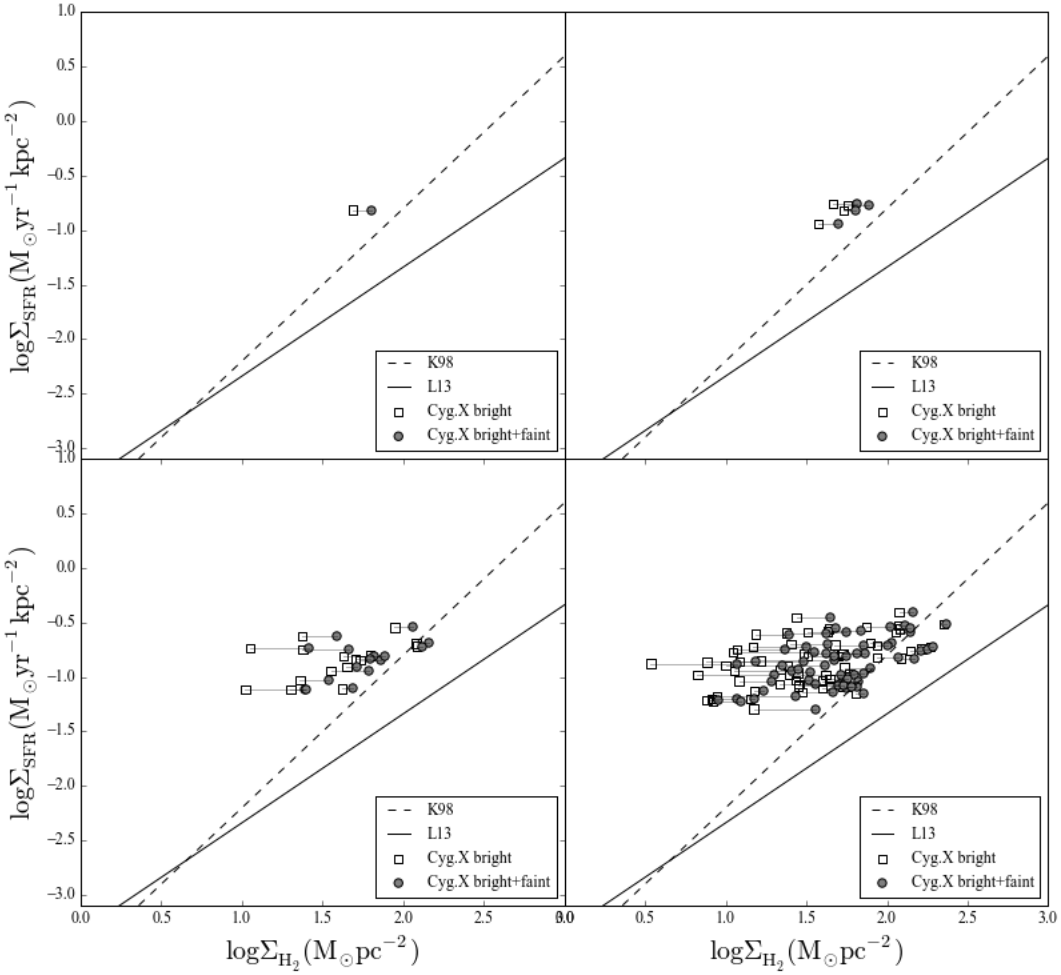

Figure 5.10: Rate of star formation and mass surface density relation for bright gas only (boxes) and bright and faint gas (circles). Plots are made using extragalactic tracers of star formation rate and molecular gas mass is derived using integrated intensity maps and the fit values of CO to H_2 conversion factor. The dashed black line shows the Kennicutt-Schmidt relation [32] with a power law index of 1.4, and the solid line shows the relation from [44] with an index of 1. Surface density images were split into a $2^\circ \times 2^\circ$ box (top left), $1^\circ \times 1^\circ$ boxes (top right), $30' \times 30'$ boxes (bottom left), and $15' \times 15'$ square boxes (bottom right) and mean surface densities were calculated for each box.

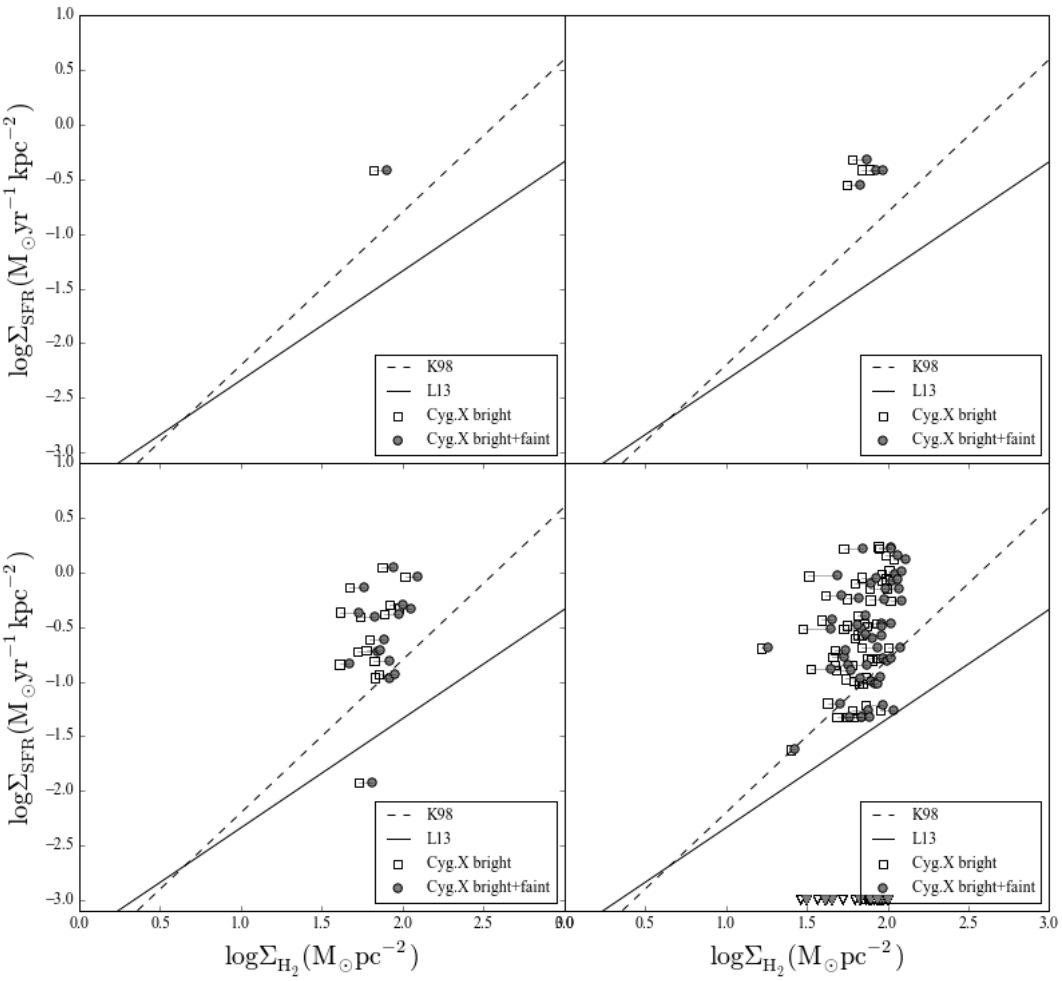

Figure 5.11: Rate of star formation and mass surface density relation for bright gas only (boxes) and bright and faint gas (circles) using Galactic tracers. These plots show the total star formation rate, counting all YSOs. The dashed black line shows the Kennicutt-Schmidt relation [32] with a power law index of 1.4, and the solid line shows the relation from [44] with an index of 1. Markers at the bottom of the plot indicate locations where the star formation rate was zero, and therefore the points are not visible. Surface density images were split into a $2^\circ \times 2^\circ$ box (top left), $1^\circ \times 1^\circ$ boxes (top right), $30' \times 30'$ boxes (bottom left), and $15' \times 15'$ square boxes (bottom right) and mean surface densities were calculated for each box.

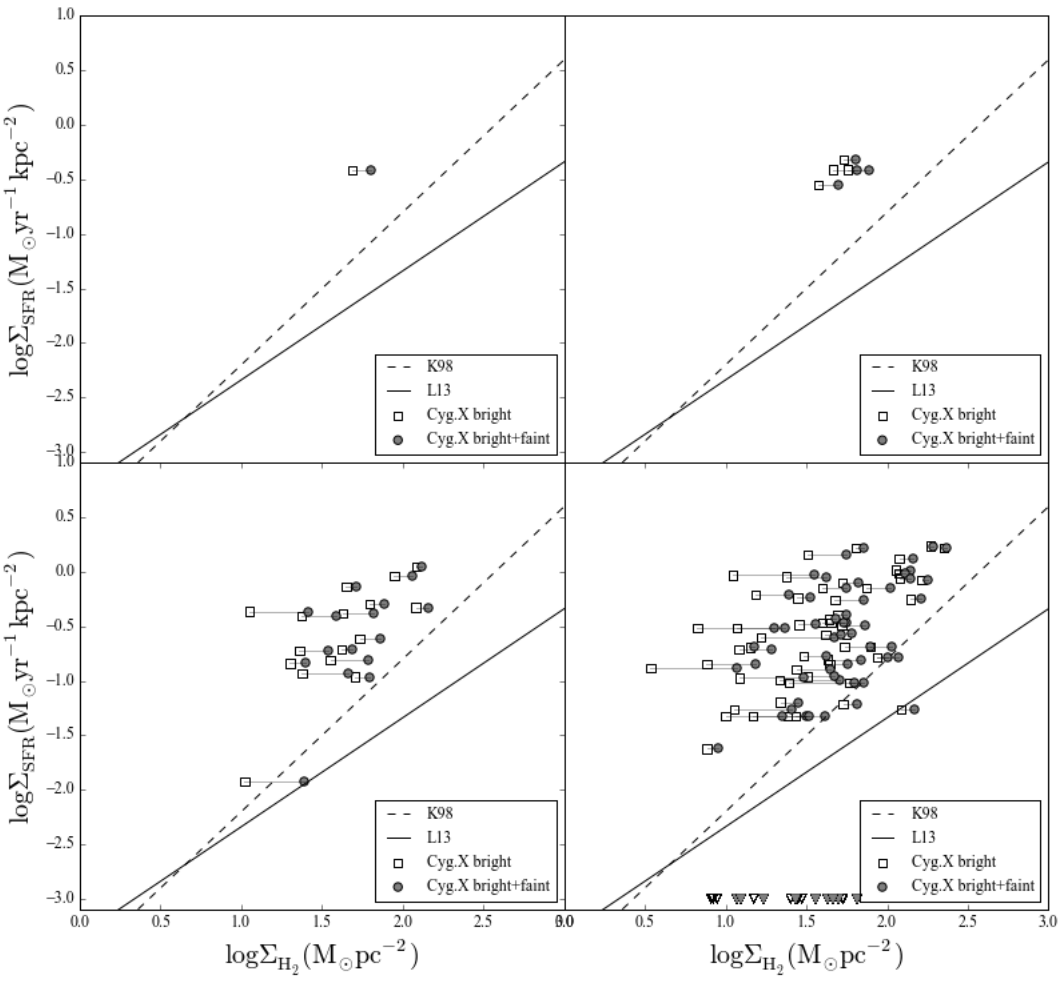

Figure 5.12: Rate of star formation and mass surface density relation for bright gas only (boxes) and bright and faint gas (circles) using Galactic star formation tracers. Gas densities were calculated using integrated intensity maps and X_{CO}, normally used for extragalactic calculations. The dashed black line shows the Kennicutt-Schmidt relation [32] with a power law index of 1.4, and the solid line shows the relation from [44] with an index of 1. Markers at the bottom of the plot indicate locations where the star formation rate was zero, and therefore the points are not visible on the plot. Surface density images were split into a $2^\circ \times 2^\circ$ box (top left), $1^\circ \times 1^\circ$ boxes (top right), $30' \times 30'$ boxes (bottom left), and $15' \times 15'$ square boxes (bottom right) and mean surface densities were calculated for each box.

the same region. I have also shown that sampling area plays a significant role in determining the relationship between star forming region and the surface density of molecular gas, which is expected, as star formation rate varies over areas where there are regions of active star formation (such as DR21), or areas where there are no signs of active formation. The low density tails present when we have small sampling areas are also hidden when averaging over larger areas. We see that averaging over larger areas provides a closer fit to known star formation laws, which is consistent with the process of calculating star formation rate and surface densities in other galaxies such as was done in [32], [44], [28], and [43] among others.

The star formation rate was consistently higher than predicted for H_2 gas by [44] for extragalactic and galactic measurements. This means that even using the same tracers as extragalactic studies for a region that is an ideal analog for extragalactic studies within the Milky Way, we still see a discrepancy. The KS relation provides a much closer fit, even though our measure of total gas column does not explicitly include atomic gas.

Chapter 6

Summary and Conclusion

The Cygnus X region is an ideal analog for the evolved star forming regions identified in extragalactic surveys. In this thesis, I explored two of the potential resolutions to the problem of increased efficiency of molecular clouds observed in local clouds. Primarily, I looked to determine the influence and distinguishing properties of the diffuse gas present in the Cygnus X region that comprises the Cygnus Rift. Furthermore I looked to test the sensitivity of the star formation rate to the tracer used as another possible explanation for the increase efficiency.

I present the highest resolution CO observations of the W80 region to date, using a Fourier transform based method to remove scan noise in the presented mosaic. I identify regions of low surface brightness gas present in the mosaic.

I developed a method of separating bright from faint clouds in both the Cygnus X and W80 datasets using a brightness distribution ratio of bright to faint gas. Using a rolling calculation of this ratio, faint clouds, which have no bright regions over large uniform areas, were uniquely identified with brightness ratios of zero. Bright-and-faint clouds were further separated into individual cloud structures that were connected spatially and spectrally. Due to the confusing nature of the region, this resulted in one large structure and multiple small clumps per datacube. Brightness distribution functions, or histograms of brightness temperature, were calculated for the largest clouds in

each dataset, and showed the lognormal and lognormal with power law tail distribution shapes [64] associated with faint and bright gas respectively.

With the packages *emcee* and RADEX in python, I used a robust method of modelling line profiles of resolved molecular clouds. From the obtained spectra, 312 lines were fit in ^{12}CO(3-2), ^{12}CO(1-0), ^{13}CO(3-2), ^{13}CO(1-0), and C^{18}O(3-2) to determine physical parameters for a series of bright and faint clouds. I found bright and faint clouds have similar physical parameters, with low surface brightness clouds showing high column densities and low kinetic temperatures relative to high surface brightness clouds.

I calculated the X factor for CO(3-2) lines from the median ratio of column density and integrated intensity for both bright and faint gas and found X factors to be indistinguishable to the type of cloud within the range of uncertainty, indicating that the molecular ratios are the same for both bright and faint gas. This is consistent with the fits of physical parameters.

I determined the mass contribution of both the bright and faint cloud components for the Cygnus X regions using two separate methods. Masses calculated directly from spectral fits of molecular clouds using maser distances from [61] for bright gas, and a faint gas distance from [23]. The total mass of the molecular gas in the portion of the Cygnus X North Cloud observed was found to be $(1.1 - 1.5) \times 10^5$ M$_\odot$ (the range arises from calculations using line fitting and X factor respectively), compared to the masses calculated in [67] of 2.8×10^5 M$_\odot$. W80 gas mass was determined using the same X factors for bright and faint gas from Cygnus X with a total mass of 2.7×10^4 M$_\odot$. From the total mass component derived for both Cygnus X and W80 it appears that faint gas comprises between 23% and 43% of the molecular ISM. This is quite different from the observations of the Sagitarius arm by [64], that showed diffuse gas dominating the molecular gas in their observation. The study of the Cygnus X and W80 molecular clouds confirms low surface brightness clouds are a contributing factor to the calculation of mass surface density, although

the extent of this is highly dependant on the distance of the cloud. Despite the close distance of the W80 and Cygnus X gas, the assumption that all gas of the W80 region is located at the same distance has large implications for both the influence of low surface brightness gas and the evolutionary state of these clouds. Assuming a closer distance for all bright gas would mean we are observing a smaller area of gas, thus limiting the contribution of the bright component to the total luminosity of the region. We conclude that the mass in Cygnus X is not dominated by a cold dark component that would close the gap in the star formation law.

Known Spitzer class 0/I and flat YSOs in the Cygnus X and W80 complex provided by [36] and [26] respectively were used to make maps of SFR surface density. YSO catalogues were cross-correlated with dust sources from Bolocam and outflows from [23] for the Cygnus X region to match YSOs with individual clouds. I note a lack of YSOs with a definite association with low surface brightness gas. From the W80 observations, we see correlation of prestellar cores with regions of low surface brightness gas indicating an earlier stage of star formation. As we can assume the low surface brightness gas of W80 and Cygnus X has similar properties based on our method of identification, not all low surface brightness gas is as quiescent as previously thought. Lack of evolved star formation in the form of class II and III YSOs associated with low surface brightness gas could be an indication of an earlier stage of star formation.

With the availability of both galactic SFR tracers through YSO catalogues provided by [36] and H_α and 24 μm extragalactic tracers, I used the Cygnus X region to compare the SFR calculated by each method. There is a striking difference between the galactic star formation rate and the extragalactic star formation rate, with the galactic star formation rate being a factor of 3 higher than its extragalactic counterpart. The extragalactic measurements match closely with the Kennicutt-Schmidt law, which is unexpected as the KS law includes both atomic and molecular gas. We would expect molecular gas

only measurements to more closely follow the Leroy [44] relation. The lower SFR calculated using extragalactic tracers may indicate that observations of late stage star formation alone do not properly sample the IMF of star forming regions on small scales.

6.1 Further Work

Further analysis with other dense gas tracers would be required to further constrain physical parameters of the Cygnus X and W80 region, as I was not able to detect emission from faint gas using $C^{18}O$. Since W80 clouds were not observed targeting dense gas tracers, which would allow the comparison of physical parameters between both regions, with unique populations of low surface brightness gas. An additional caveat is that I assumed beam filling emission, but further work would involve allowing the filling factor to vary, for smaller clouds.

I did not present an extragalactic star formation rate for the W80 region, as the Spitzer Cygnus X Legacy Survey did not cover most of the W80 region observed. The next step would be to use available WISE 22 micron data to create extragalactic star formation maps for W80. The H_α data available from WHAM is also very low resolution, so further analysis should use a mosaic of higher resolution images from surveys such as IPHAS.

The calculation of column density has a strong dependance on the CO-to-H_2 conversion factor, using a dust calibrated X factor would go a long way in mass calibration.

Bibliography

[1] Aguirre, J. E., Ginsburg, A. G., Dunham, M. K., et al. 2011, ApJS, 192, 4

[2] André, P., Di Francesco, J., Ward-Thompson, D., et al. 2014, Protostars and Planets VI, 27

[3] Andre, P., Ward-Thompson, D., & Barsony, M. 1993, ApJ, 406, 122

[4] Bally, J., Ginsburg, A., Probst, R., et al. 2014, AJ, 148, 120

[5] Bally, J., & Scoville, N. Z. 1980, ApJ, 239, 121

[6] Binney, J., & Merrifield, M. 1998, Galactic Astronomy

[7] Bolatto, A. D., Wolfire, M., & Leroy, A. K. 2013, ARA&A, 51, 207

[8] Calzetti, D., Kennicutt, R. C., Engelbracht, C. W., et al. 2007, ApJ, 666, 870

[9] Chabrier, G. 2003, PASP, 115, 763

[10] Choi, Y., van der Tak, F. F. S., Bergin, E. A., & Plume, R. 2014, A&A, 572, L10

[11] Comerón, F., & Pasquali, A. 2005, A&A, 430, 541

[12] Crutcher, R. M. 2010, Highlights of Astronomy, 15, 438

[13] Currie, M. J., Berry, D. S., Jenness, T., et al. 2014, in Astronomical Society of the Pacific Conference Series, Vol. 485, Astronomical Data Analysis Software and Systems XXIII, ed. N. Manset & P. Forshay, 391

[14] Dame, T. M. 2011, ArXiv e-prints, arXiv:1101.1499

[15] Dame, T. M., Ungerechts, H., Cohen, R. S., et al. 1987, ApJ, 322, 706

[16] Davis, T. A. 2014, MNRAS, 445, 2378

[17] Dennison, B., Simonetti, J. H., & Topasna, G. A. 1999, in Bulletin of the American Astronomical Society, Vol. 31, American Astronomical Society Meeting Abstracts, 1455

[18] Draine, B. T. 2011, Physics of the Interstellar and Intergalactic Medium

[19] Dunham, M. M., Allen, L. E., Evans, II, N. J., et al. 2015, ArXiv e-prints, arXiv:1508.03199

[20] Emerson, D. T., & Graeve, R. 1988, A&A, 190, 353

[21] Feldt, C. 1993, A&A, 276, 531

[22] Foreman-Mackey, D., Hogg, D. W., Lang, D., & Goodman, J. 2013, PASP, 125, 306

[23] Gottschalk, M., Kothes, R., Matthews, H. E., Landecker, T. L., & Dent, W. R. F. 2012, A&A, 541, A79

[24] Greene, T. P., Wilking, B. A., Andre, P., Young, E. T., & Lada, C. J. 1994, ApJ, 434, 614

[25] Gregory, P. C. 2005, Bayesian Logical Data Analysis for the Physical Sciences: A Comparative Approach with 'Mathematica' Support (Cambridge University Press)

[26] Guieu, S., Rebull, L. M., Stauffer, J. R., et al. 2009, ApJ, 697, 787

[27] Haffner, L. M., Reynolds, R. J., Tufte, S. L., et al. 2003, ApJS, 149, 405

[28] Heiderman, A., Evans, II, N. J., Allen, L. E., Huard, T., & Heyer, M. 2010, ApJ, 723, 1019

[29] Johnson, K. E., Leroy, A. K., Indebetouw, R., et al. 2015, ApJ, 806, 35

[30] Jones, E., Oliphant, T., Peterson, P., et al. 2001–, SciPy: Open source scientific tools for Python, [Online; accessed 2015-08-20]

[31] Kennicutt, R. C., & Evans, N. J. 2012, ARA&A, 50, 531

[32] Kennicutt, Jr., R. C. 1998, ApJ, 498, 541

[33] Knödlseder, J. 2000, A&A, 360, 539

[34] Kothes, R., Landecker, T. L., Foster, T., & Leahy, D. A. 2001, A&A, 376, 641

[35] Kroupa, P., Tout, C. A., & Gilmore, G. 1993, MNRAS, 262, 545

[36] Kryukova, E., Megeath, S. T., Hora, J. L., et al. 2014, AJ, 148, 11

[37] Lada, C. J., Forbrich, J., Lombardi, M., & Alves, J. F. 2012, ApJ, 745, 190

[38] Lada, C. J., & Lada, E. A. 2003, ARA&A, 41, 57

[39] Lada, C. J., Lombardi, M., & Alves, J. F. 2010, ApJ, 724, 687

[40] Larson, R. B. 1981, MNRAS, 194, 809

[41] Laugalys, V., & Straižys, V. 2002, Baltic Astronomy, 11, 205

[42] Leahy, D. A., & Green, K. S. 2012, ApJ, 760, 25

[43] Leroy, A. K., Bigiel, F., de Blok, W. J. G., et al. 2012, AJ, 144, 3

[44] Leroy, A. K., Walter, F., Sandstrom, K., et al. 2013, AJ, 146, 19

[45] Leung, H. O., & Thaddeus, P. 1992, ApJS, 81, 267

[46] Lynds, B. T. 1962, ApJS, 7, 1

[47] Mangum, J. G., & Shirley, Y. L. 2015, PASP, 127, 266

[48] Matthews, H. E., & Goss, W. M. 1980, A&A, 88, 267

[49] McKee, C. F., & Ostriker, E. C. 2007, ARA&A, 45, 565

[50] Murphy, E. J., Condon, J. J., Schinnerer, E., et al. 2011, ApJ, 737, 67

[51] Myers, P. C. 2009, ApJ, 700, 1609

[52] Passot, T., Pouquet, A., & Woodward, P. 1988, A&A, 197, 228

[53] Pérez, F., & Granger, B. E. 2007, Computing in Science and Engineering, 9, 21

[54] Piddington, J. H., & Minnett, H. C. 1952, Australian Journal of Scientific Research A Physical Sciences, 5, 17

[55] Pilbratt, G. L., Riedinger, J. R., Passvogel, T., et al. 2010, A&A, 518, L1

[56] Pineda, J. E., Caselli, P., & Goodman, A. A. 2008, ApJ, 679, 481

[57] Press, W. H., Teukolsky, S. A., Vetterling, W. T., & Flannery, B. P. 2002, Numerical recipes in C++ : the art of scientific computing

[58] Rosolowsky, E. 2005, PASP, 117, 1403

[59] Rosolowsky, E., Dunham, M. K., Ginsburg, A., et al. 2010, ApJS, 188, 123

[60] Rosolowsky, E. W., Pineda, J. E., Kauffmann, J., & Goodman, A. A. 2008, ApJ, 679, 1338

[61] Rygl, K. L. J., Brunthaler, A., Sanna, A., et al. 2012, A&A, 539, A79

[62] Salpeter, E. E. 1955, ApJ, 121, 161

[63] Sawada, T., Hasegawa, T., & Koda, J. 2012, ApJ, 759, L26

[64] Sawada, T., Hasegawa, T., Sugimoto, M., Koda, J., & Handa, T. 2012, ApJ, 752, 118

[65] Schmidt, M. 1959, ApJ, 129, 243

[66] Schnee, S., Mason, B., Di Francesco, J., et al. 2014, MNRAS, 444, 2303

[67] Schneider, N., Bontemps, S., Simon, R., et al. 2006, A&A, 458, 855

[68] Schöier, F. L., van der Tak, F. F. S., van Dishoeck, E. F., & Black, J. H. 2005, A&A, 432, 369

[69] Skrutskie, M. F., Cutri, R. M., Stiening, R., et al. 2006, AJ, 131, 1163

[70] Sobolev, V. V. 1957, Soviet Ast., 1, 678

[71] Solomon, P. M., Sanders, D. B., & Scoville, N. Z. 1979, ApJ, 232, L89

[72] Spitzer, L. 1998, Physical Processes in the Interstellar Medium

[73] Stahler, S. W., & Palla, F. 2005, The Formation of Stars

[74] Taylor, A. R., Gibson, S. J., Peracaula, M., et al. 2003, AJ, 125, 3145

[75] Uyanıker, B., Fürst, E., Reich, W., Aschenbach, B., & Wielebinski, R. 2001, A&A, 371, 675

[76] van der Tak, F. F. S., Black, J. H., Schöier, F. L., Jansen, D. J., & van Dishoeck, E. F. 2007, A&A, 468, 627

[77] van Dishoeck, E. F., & Blake, G. A. 1998, ARA&A, 36, 317

[78] Westerhout, G. 1958, Bull. Astron. Inst. Netherlands, 14, 215

[79] Wilson, T. L., Rohlfs, K., & Hüttemeister, S. 2013, Tools of Radio Astronomy, doi:10.1007/978-3-642-39950-3

[80] Wilson, T. L., & Rood, R. 1994, ARA&A, 32, 191

[81] Zhang, S. B., Yang, J., Xu, Y., et al. 2011, ApJS, 193, 10

Appendix A

Description of Packages

Below I have included the list of published packages used in this research with a brief description and version number.

A.1 Python

All packages listed below were used with python version 2.7. This research made use of IPython version 3.0.0 [53].

- astropy (v.1.0.3): astronomy package containing core operations. Primarily used for handling FITS data format and converting coordinates.
- SpectralCube(v.0.2.2): package for handling statistics and analysis of three dimensional datasets.
- numpy (v.1.9.2): Python package for handling mathematical functions and arrays.
- scipy (v.0.15.1): Python mathematics statistics packages [30].
- skimage (v.0.11.2): mathematical image analysis package.
- emcee (v.0.11.2): Markov-Chain monte carlo implementation.

A.2 Starlink

Starlink is software developed by the Joint Astronomy Centre for astronomical data processing. Currently supported by the East Asian Observatory, access to code can be found at `http://starlink.eao.hawaii.edu/starlink`.

- kappa (v.2.0.9): image process and data analysis.
- smurf (v.1.5.0): submillimetre data reduction package.
- convert (v.1.7): convert between FITS and NDF file format.

Appendix B

Spectral Fits

Each spectrum shown in the figures below contain models for the lines that were included in the final analysis.

Faint Clouds CO(3-2) Spectrum: Cygnus X1

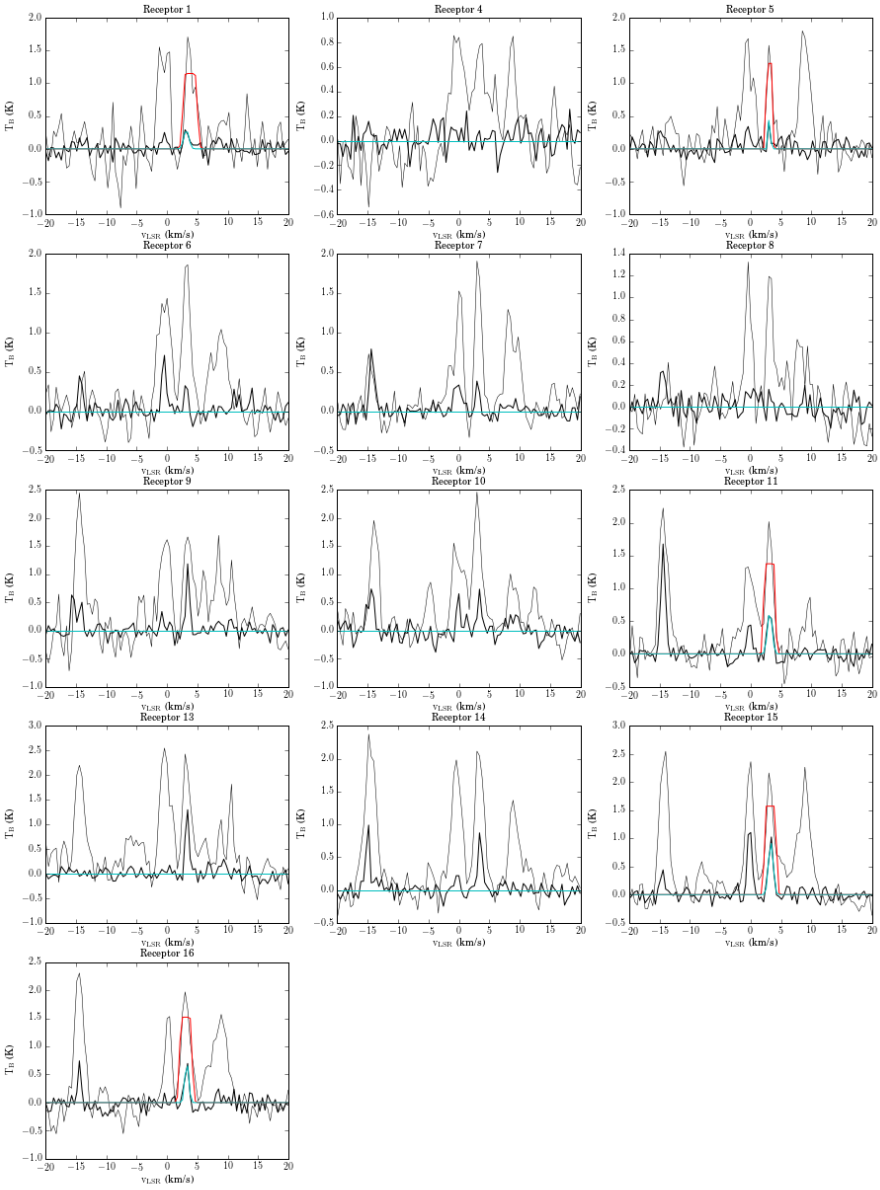

Faint Clouds CO(3-2) Spectrum: Cygnus X2

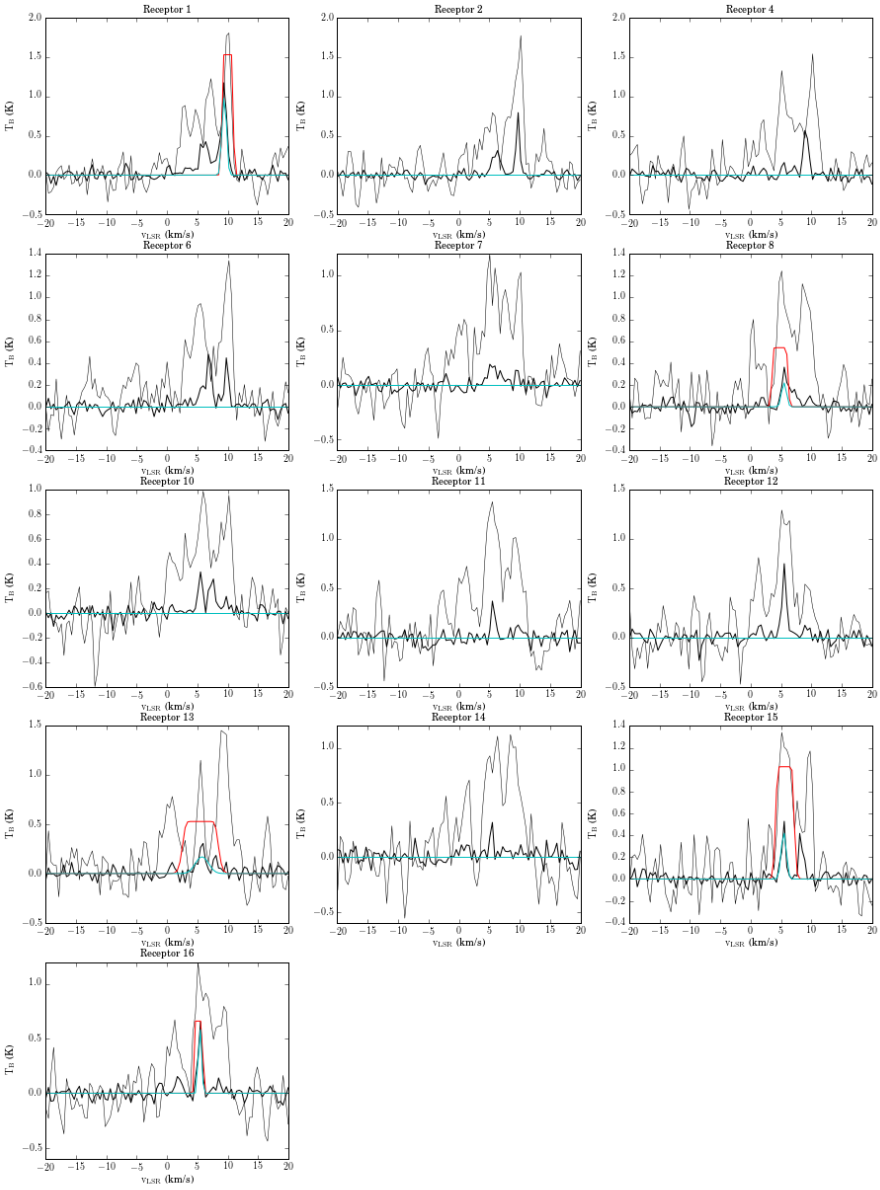

Faint Clouds CO(3-2) Spectrum: Cygnus X3

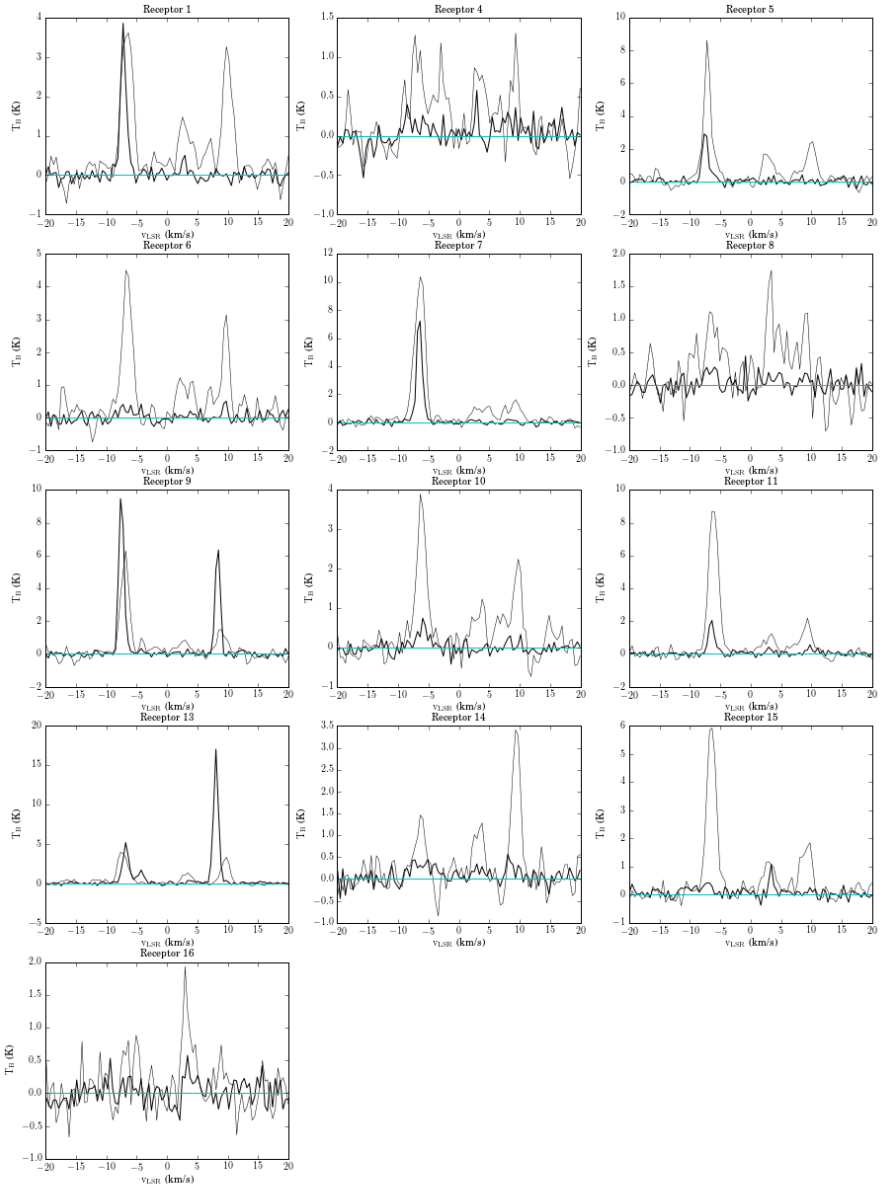

Faint Clouds CO(3-2) Spectrum: Cygnus X4

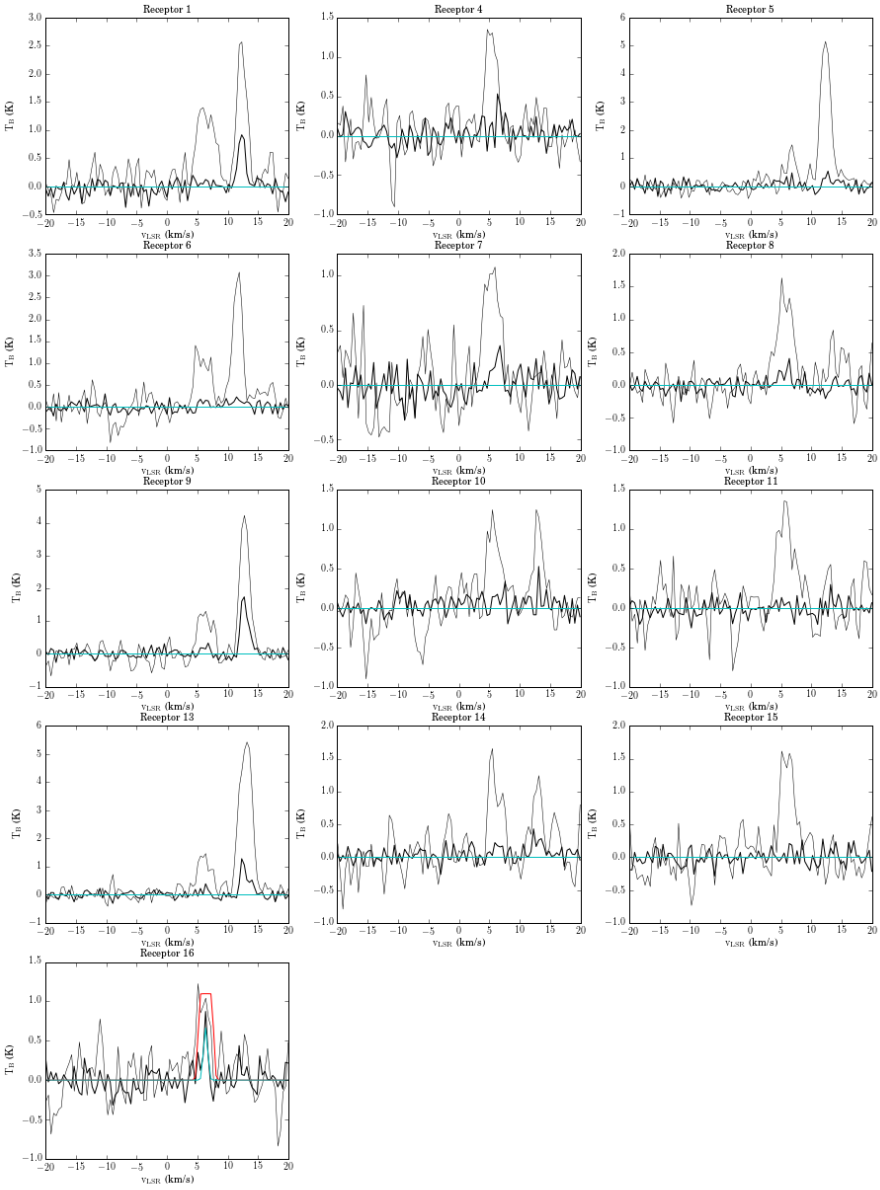

Faint Clouds CO(3-2) Spectrum: Cygnus X5

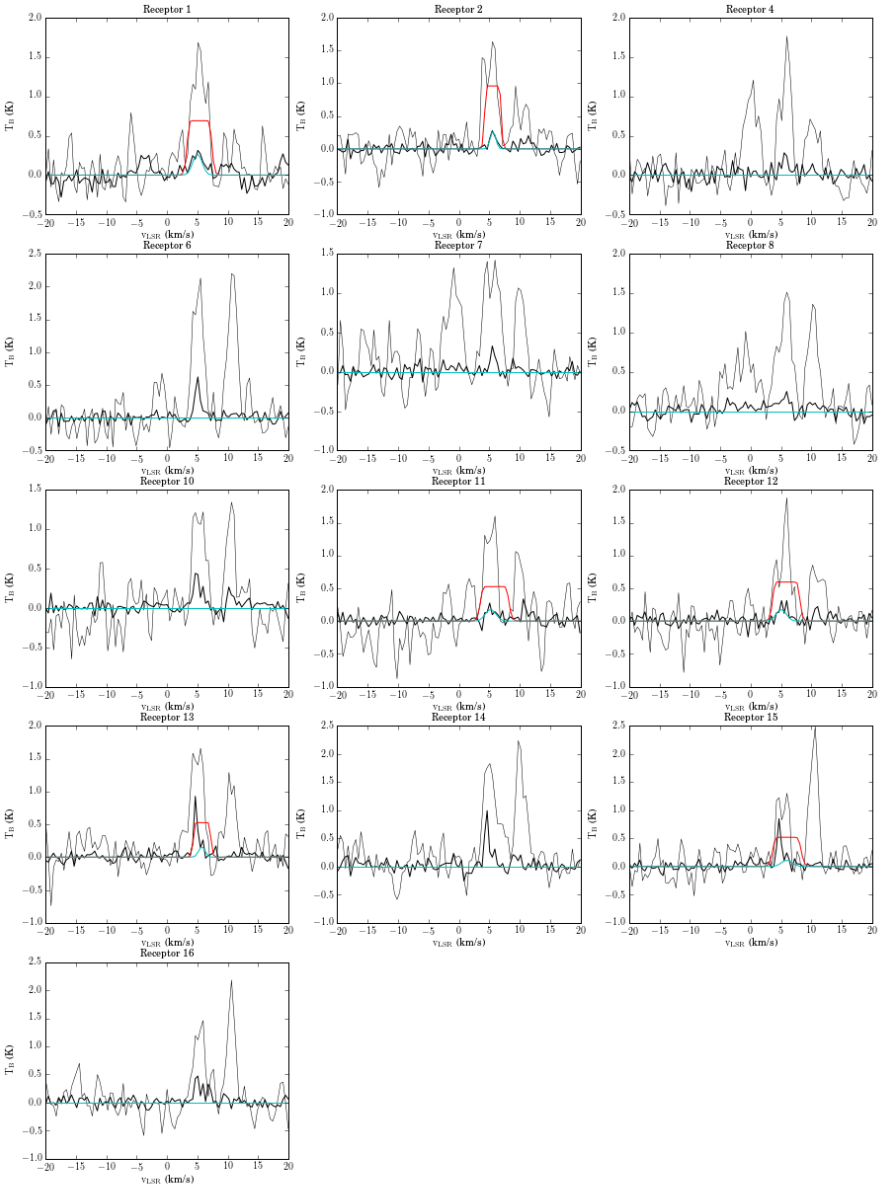

Faint Clouds CO(3-2) Spectrum: Cygnus X6

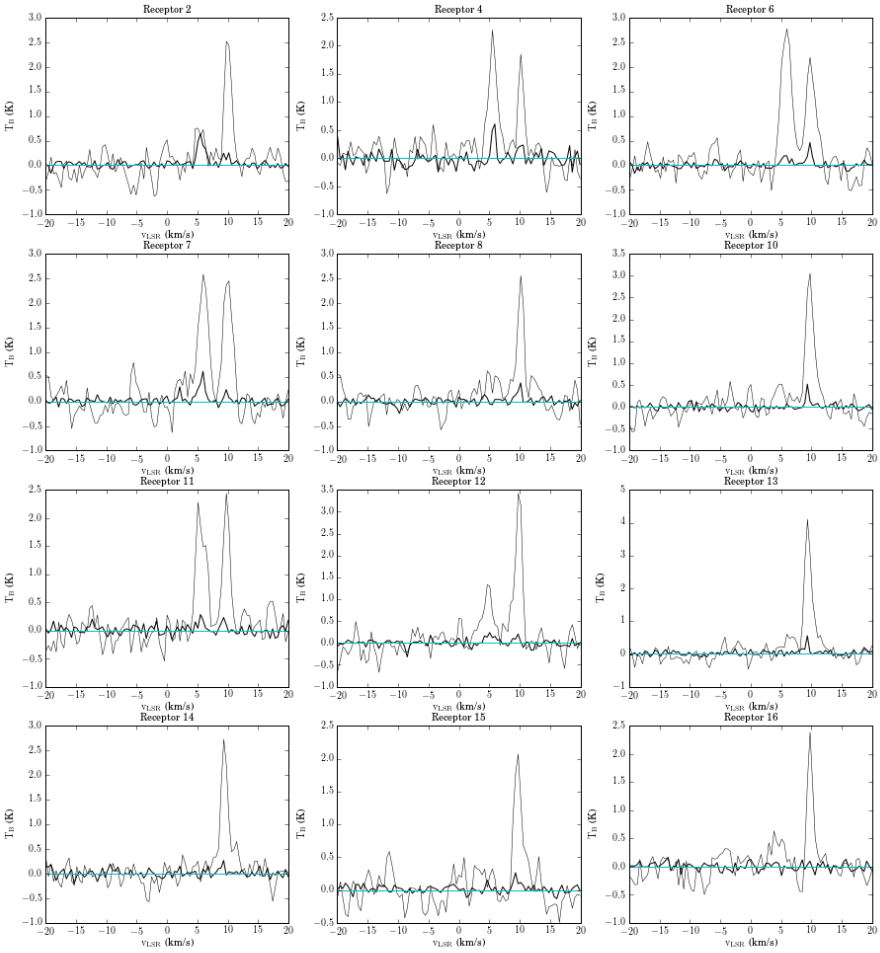

Faint Clouds CO(3-2) Spectrum: Cygnus X7

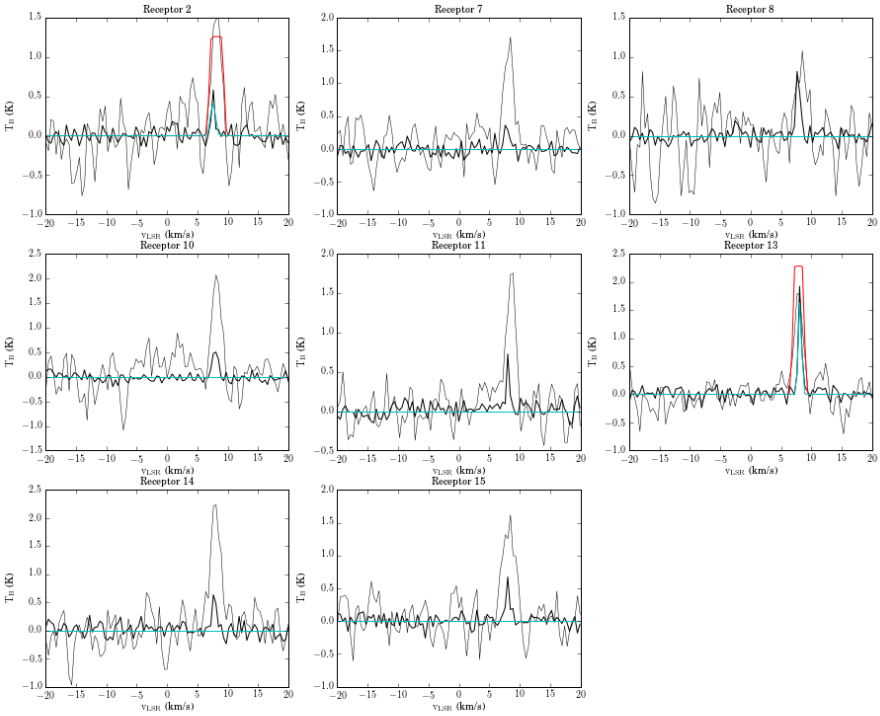

Faint Clouds CO(3-2) Spectrum: Cygnus X8

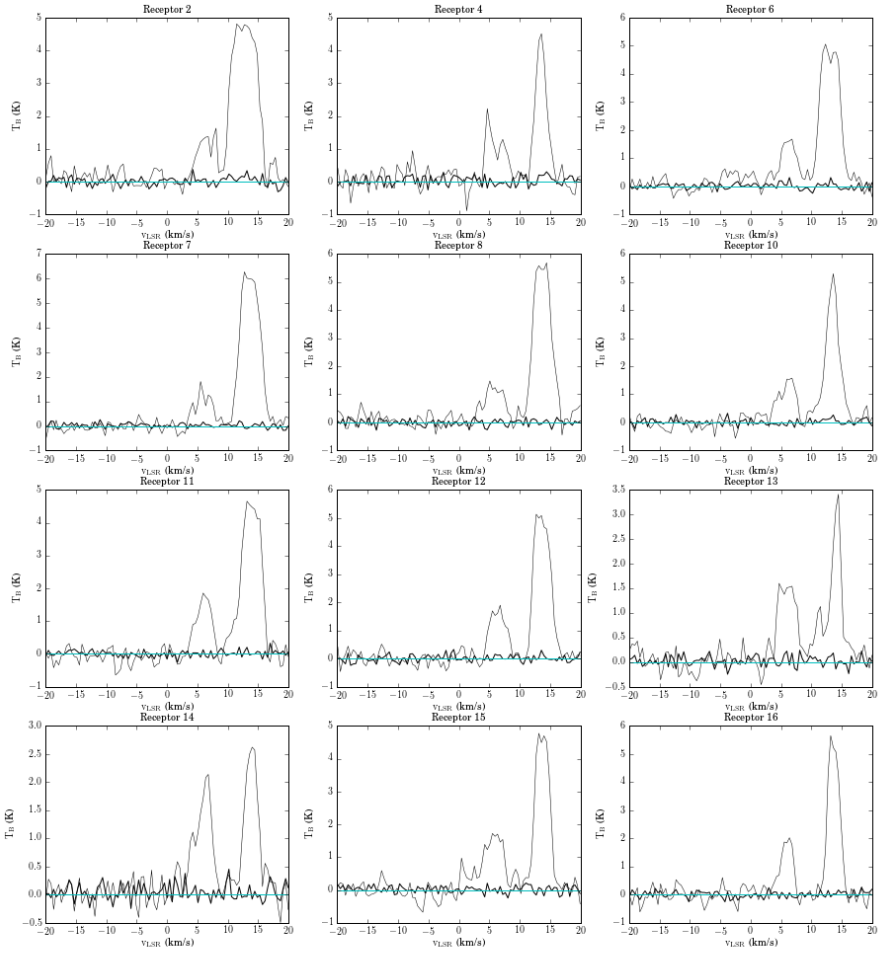

Faint Clouds CO(3-2) Spectrum: Cygnus X9

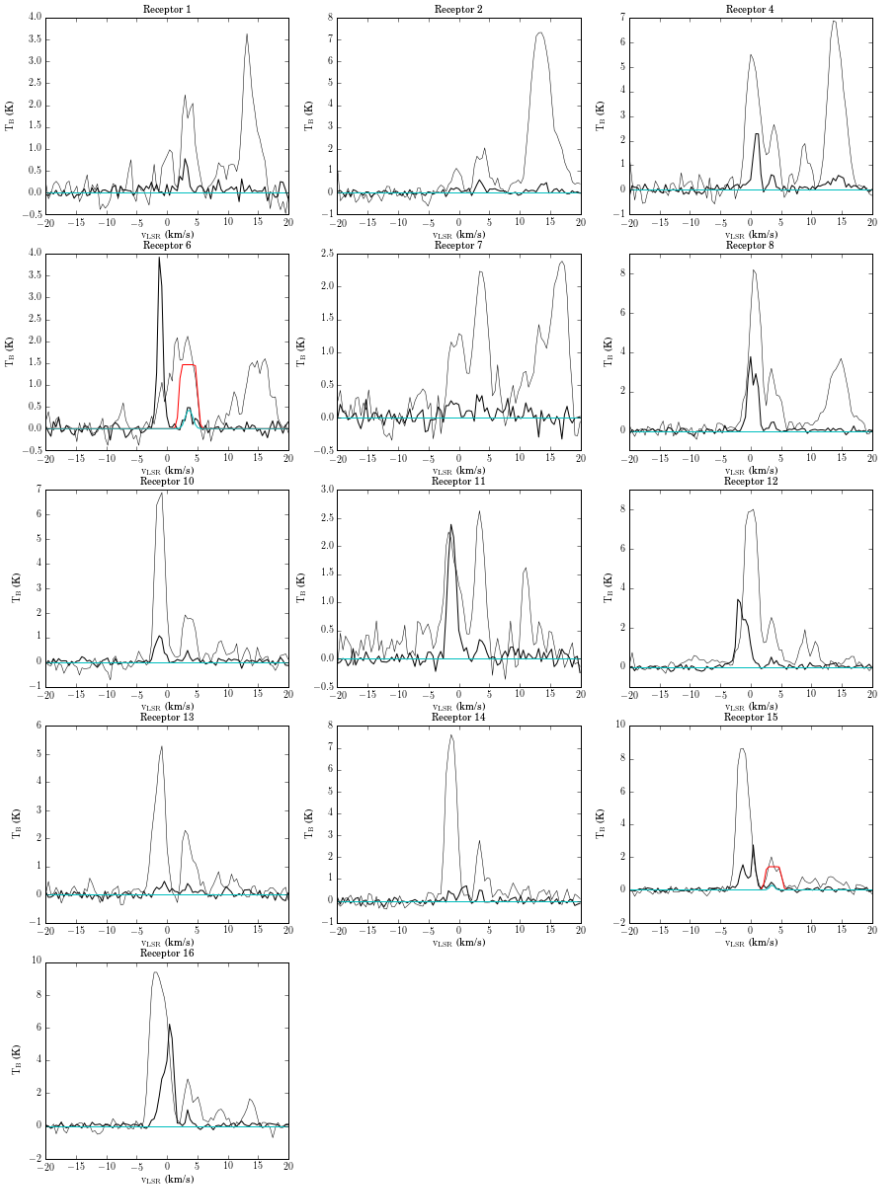

Bright Clouds CO(3-2) Spectrum: Cygnus X1

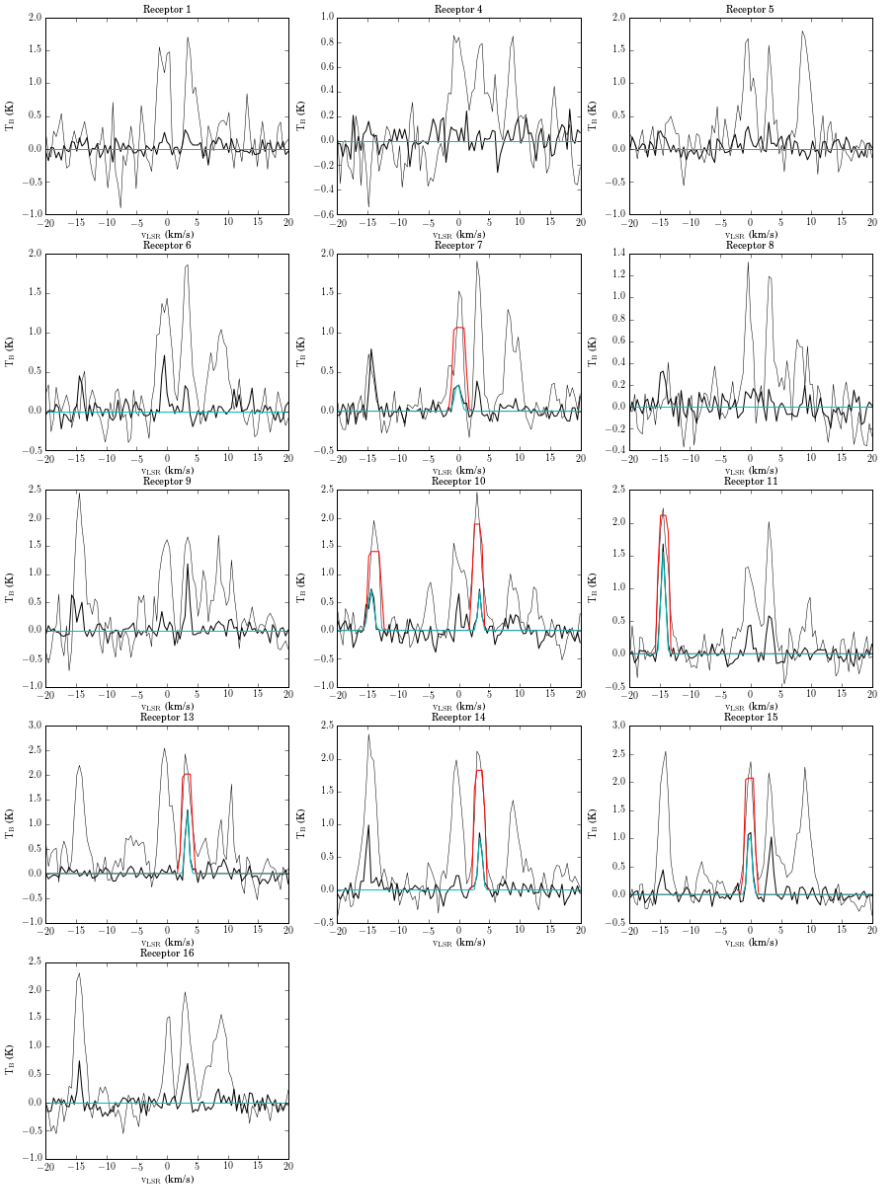

Bright Clouds CO(3-2) Spectrum: Cygnus X2

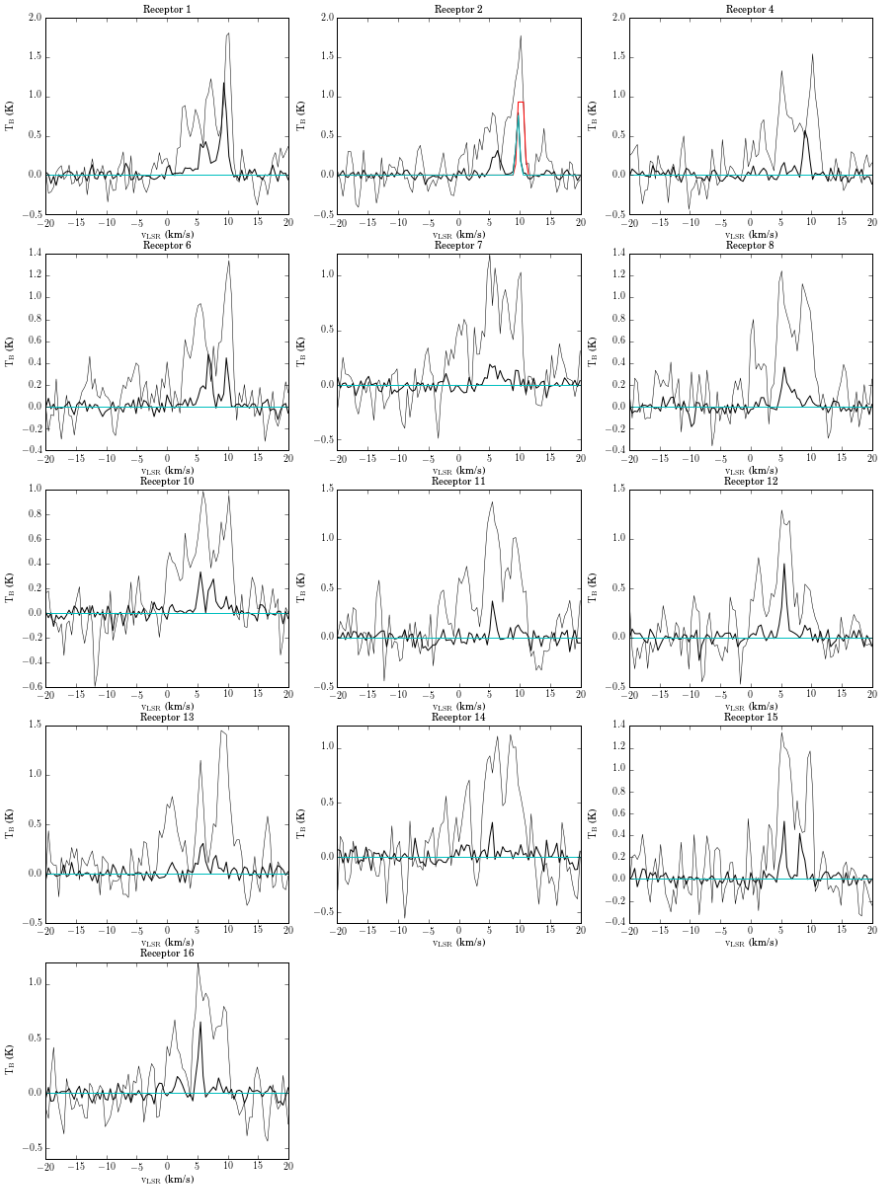

Bright Clouds CO(3-2) Spectrum: Cygnus X3

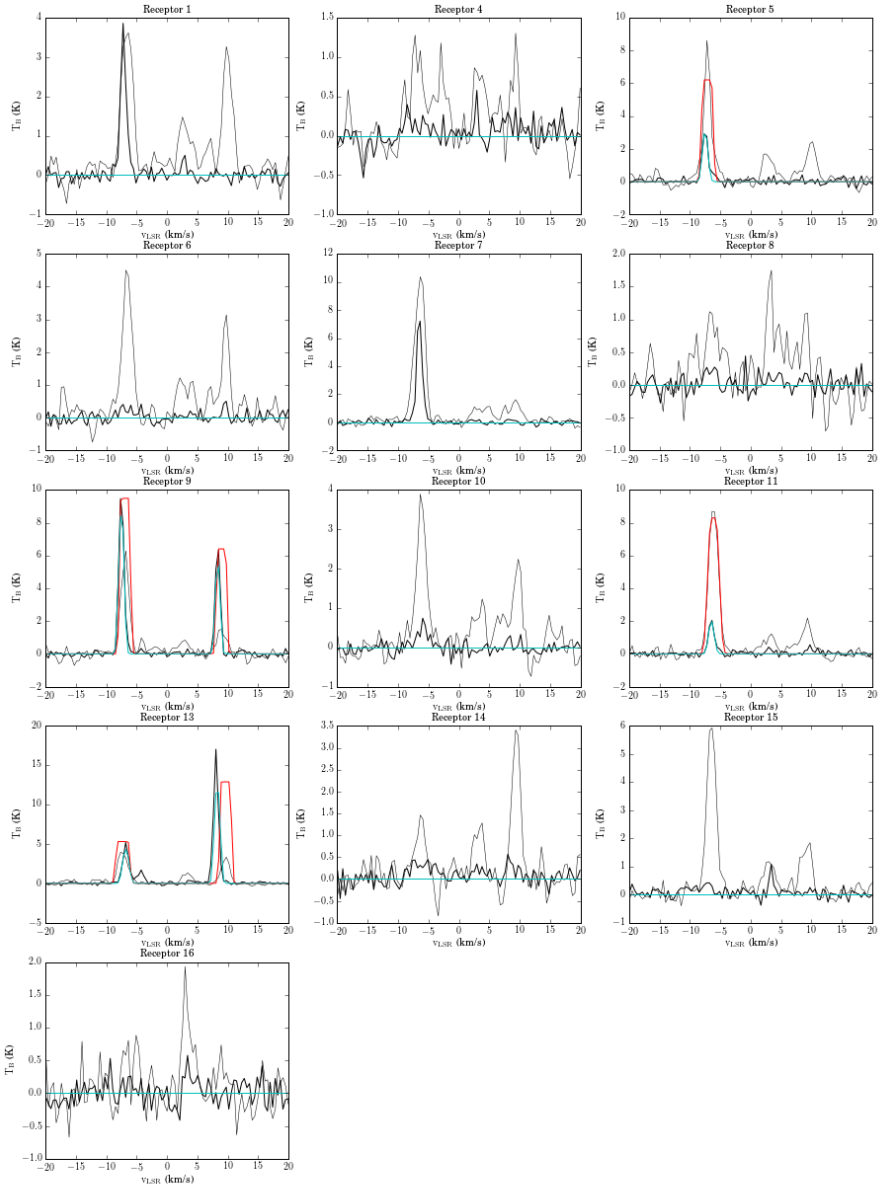

Bright Clouds CO(3-2) Spectrum: Cygnus X4

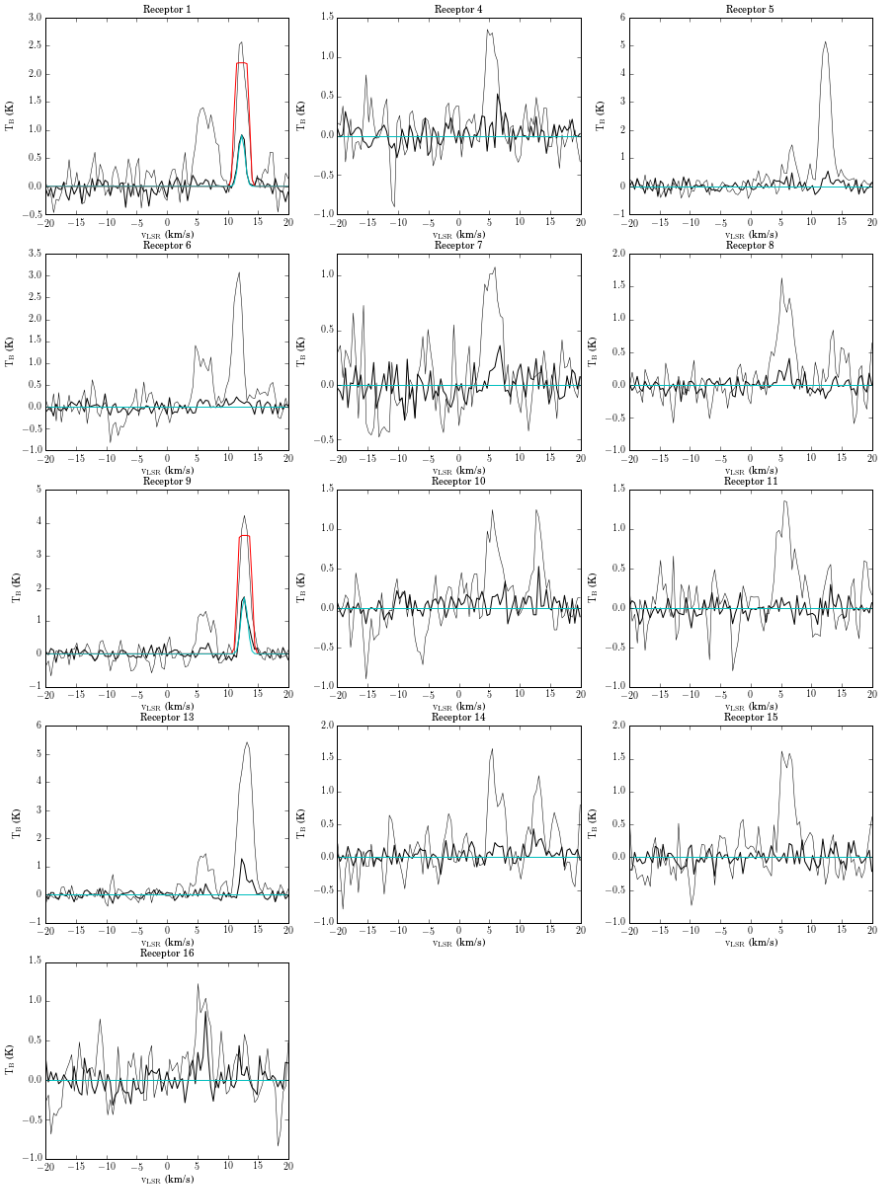

Bright Clouds CO(3-2) Spectrum: Cygnus X5

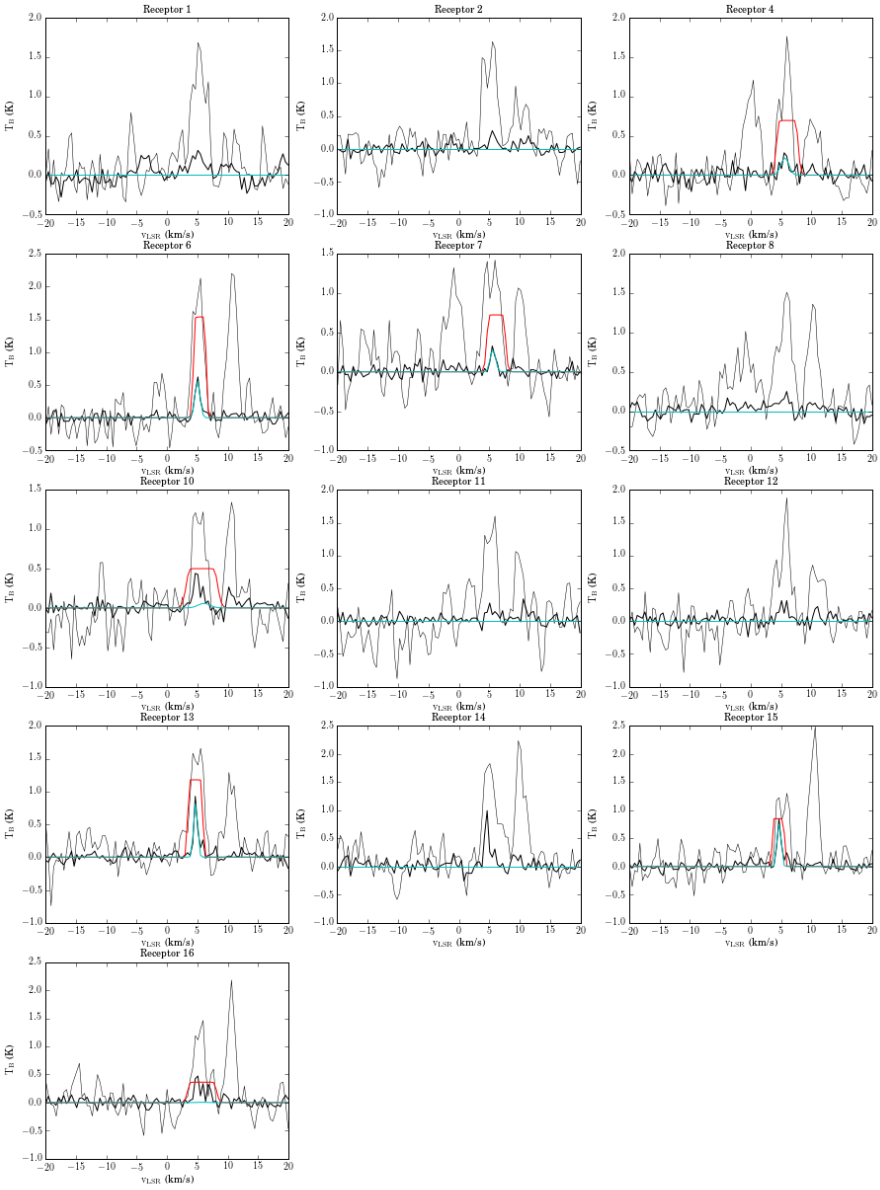

Bright Clouds CO(3-2) Spectrum: Cygnus X6

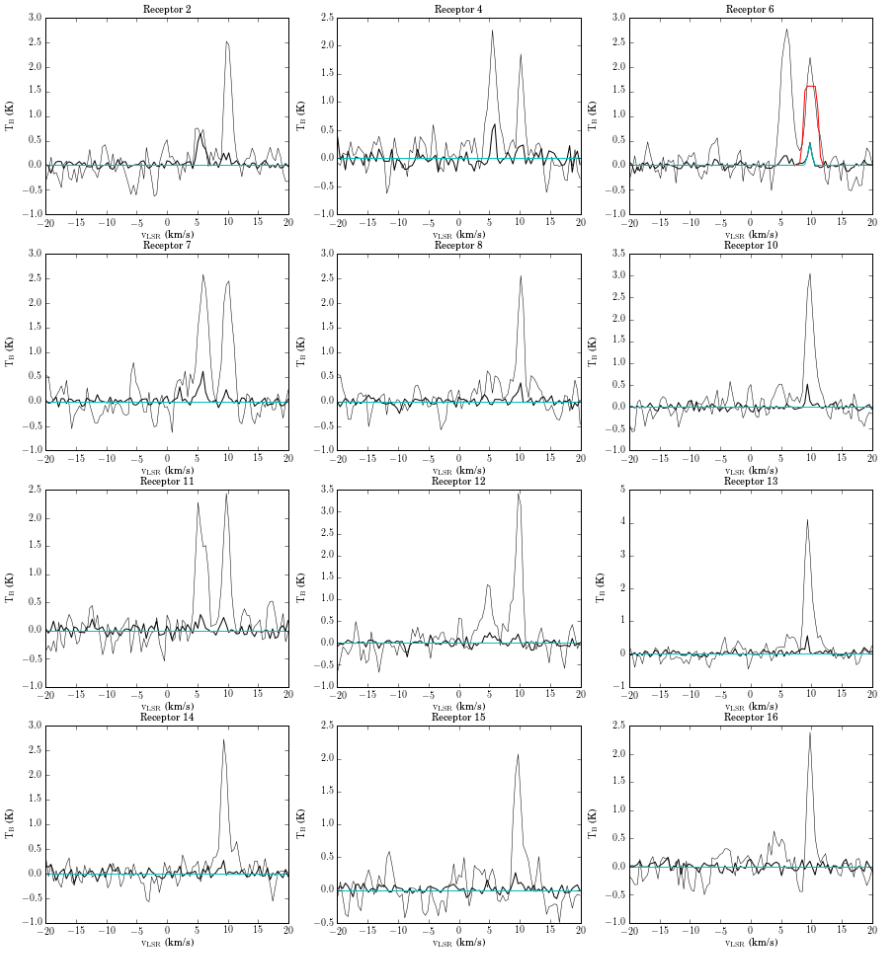

Bright Clouds CO(3-2) Spectrum: Cygnus X7

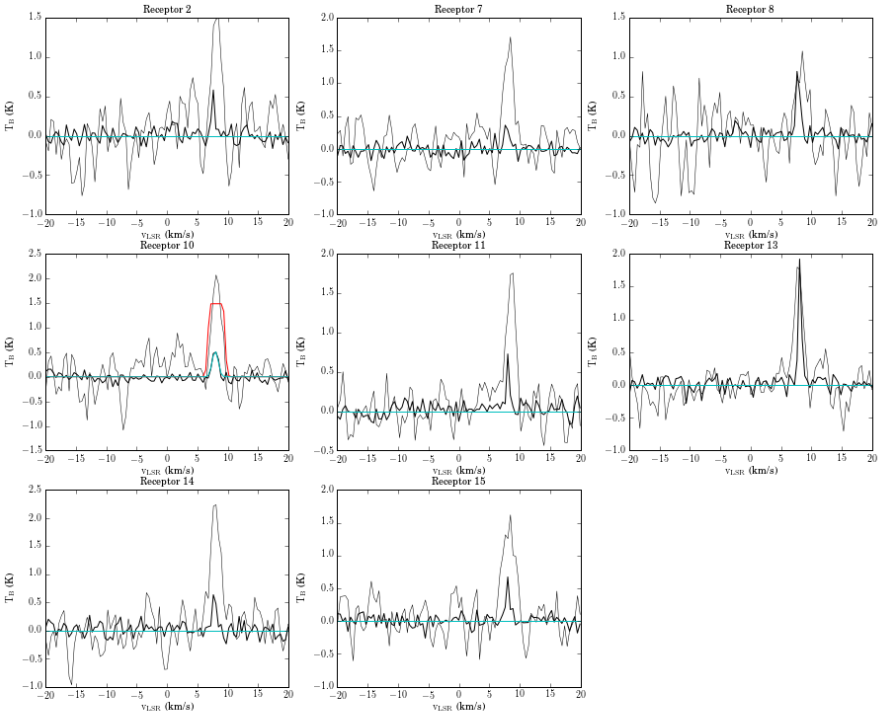

Bright Clouds CO(3-2) Spectrum: Cygnus X8

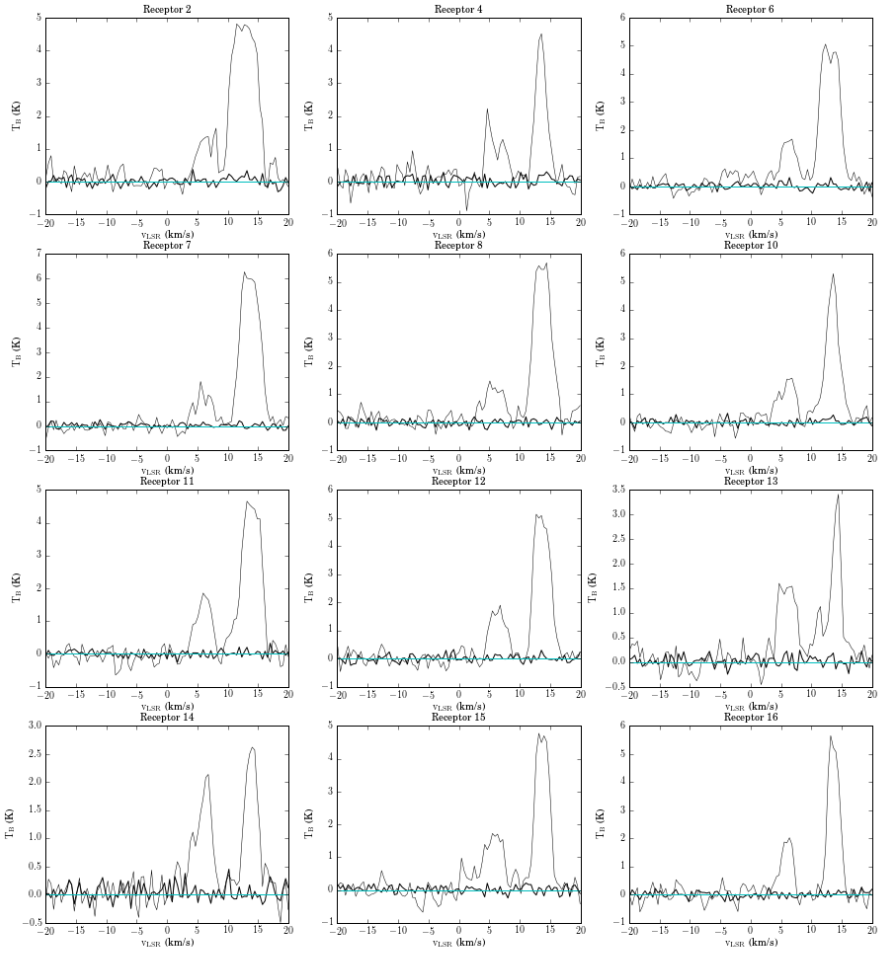

Bright Clouds CO(3-2) Spectrum: Cygnus X9

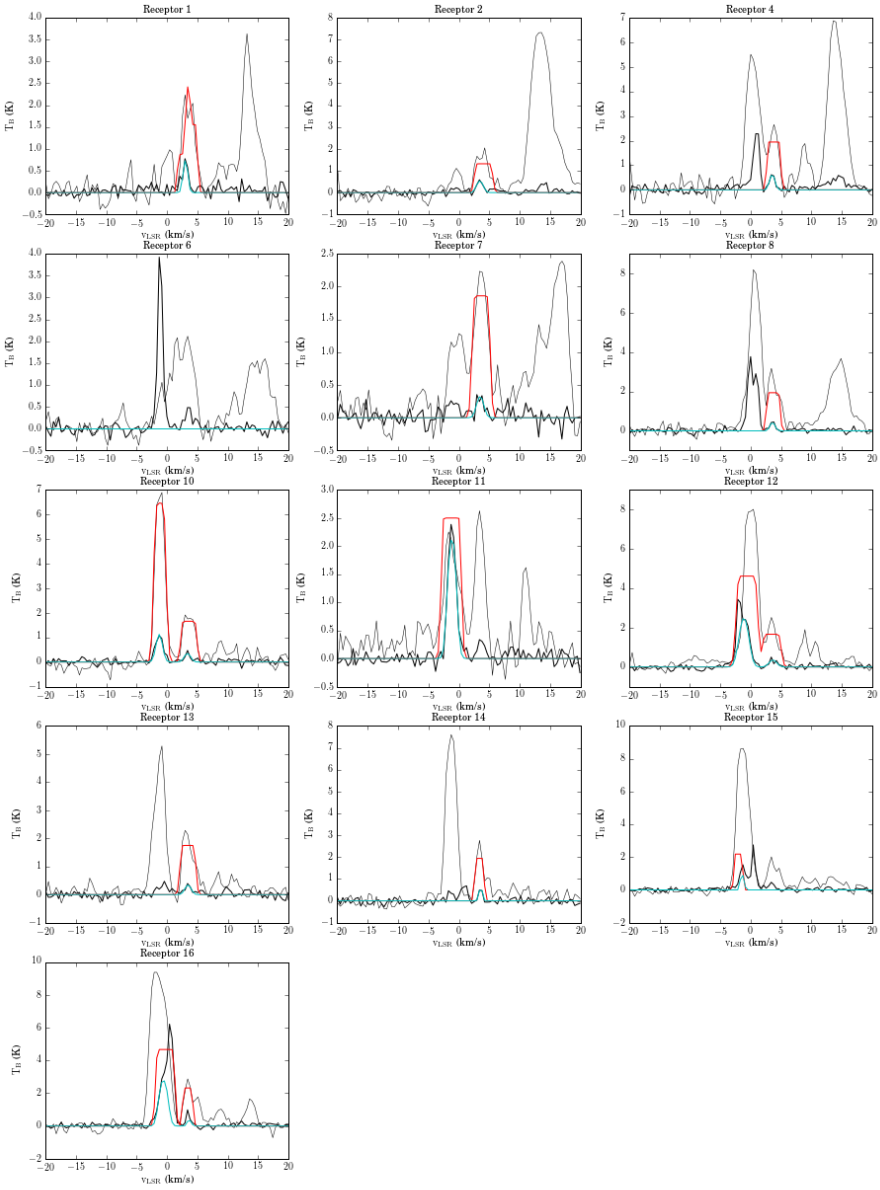

Faint Clouds CO(1-0) Spectrum: Cygnus X1

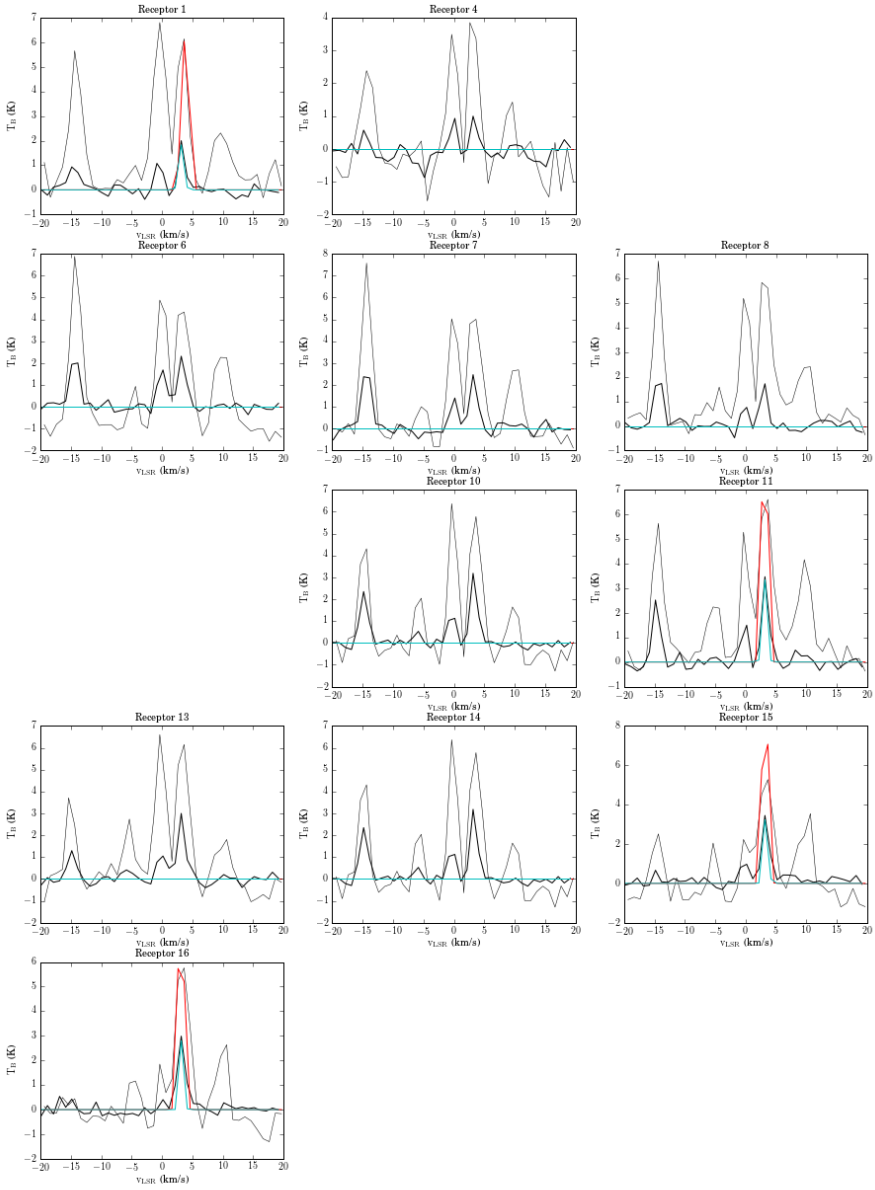

Faint Clouds CO(1-0) Spectrum: Cygnus X2

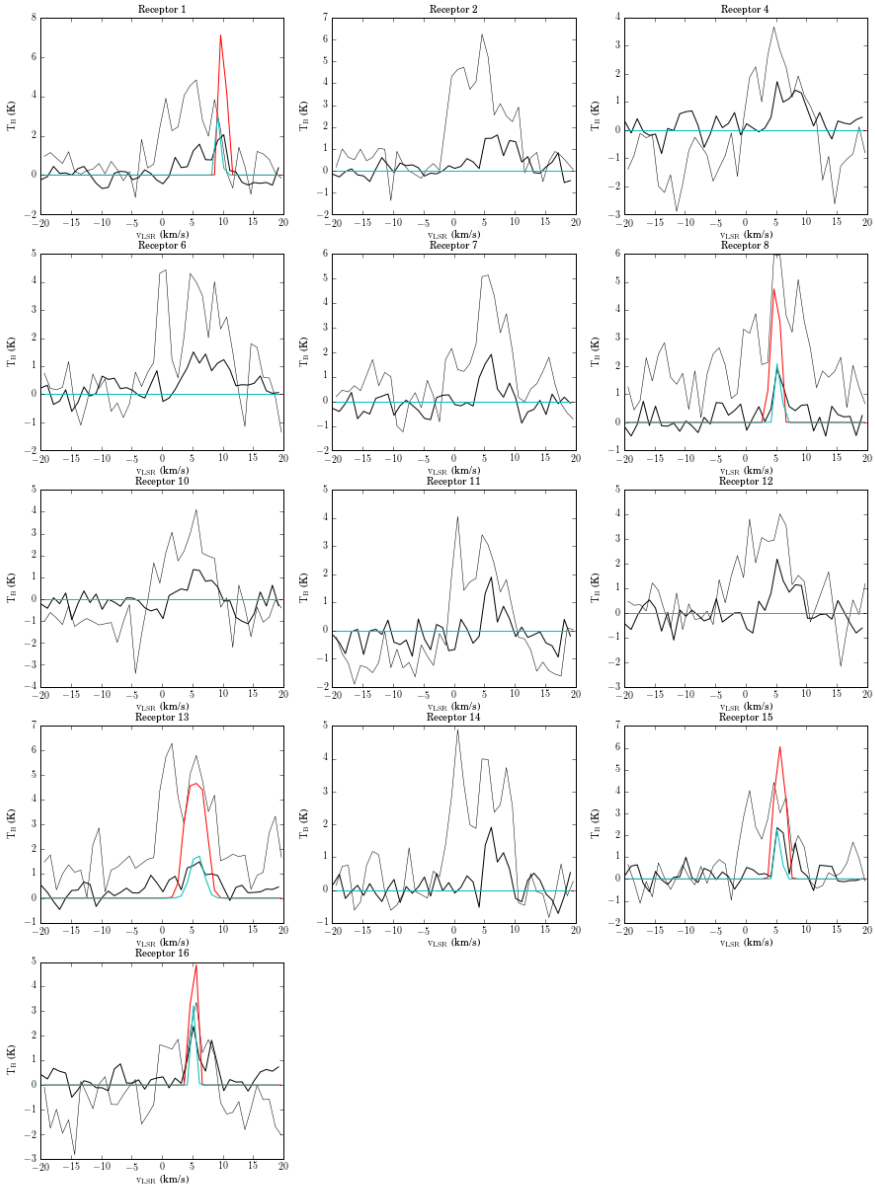

Faint Clouds CO(1-0) Spectrum: Cygnus X3

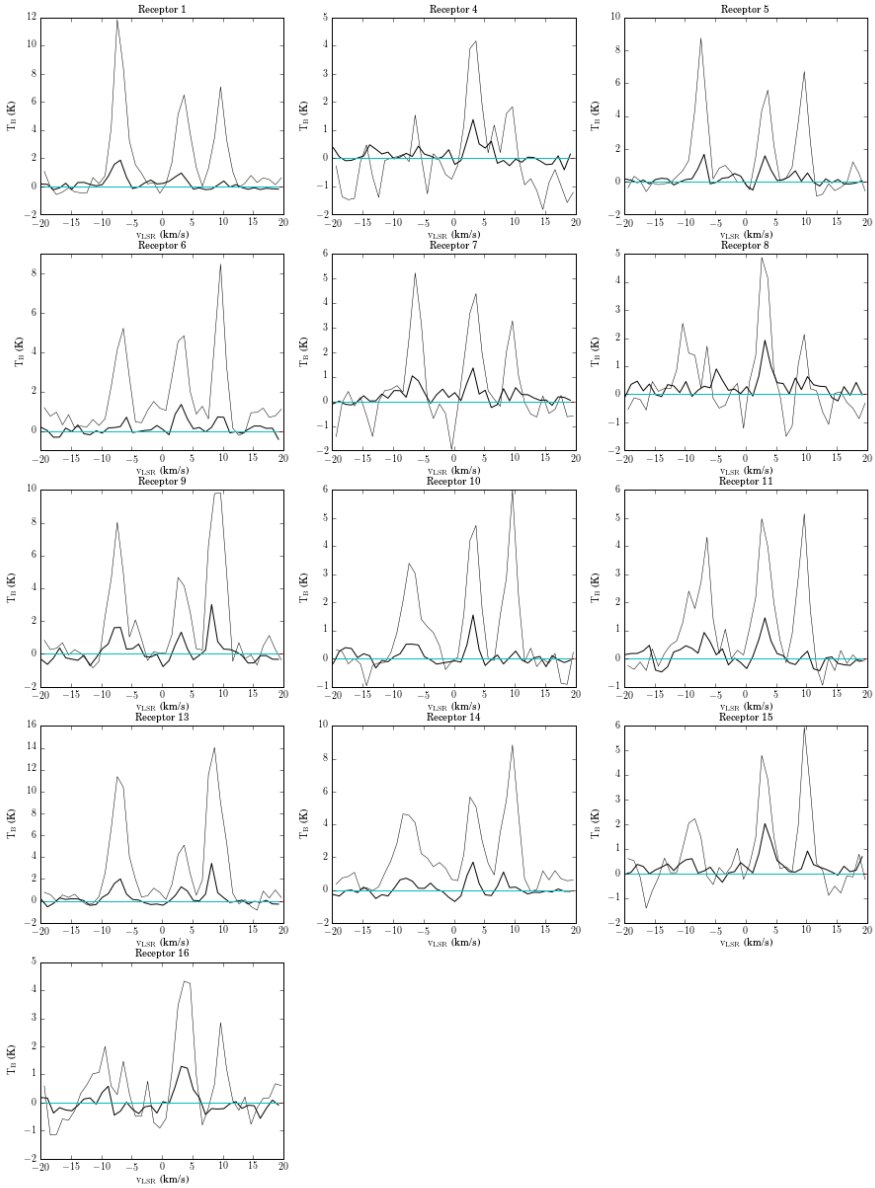

Faint Clouds CO(1-0) Spectrum: Cygnus X4

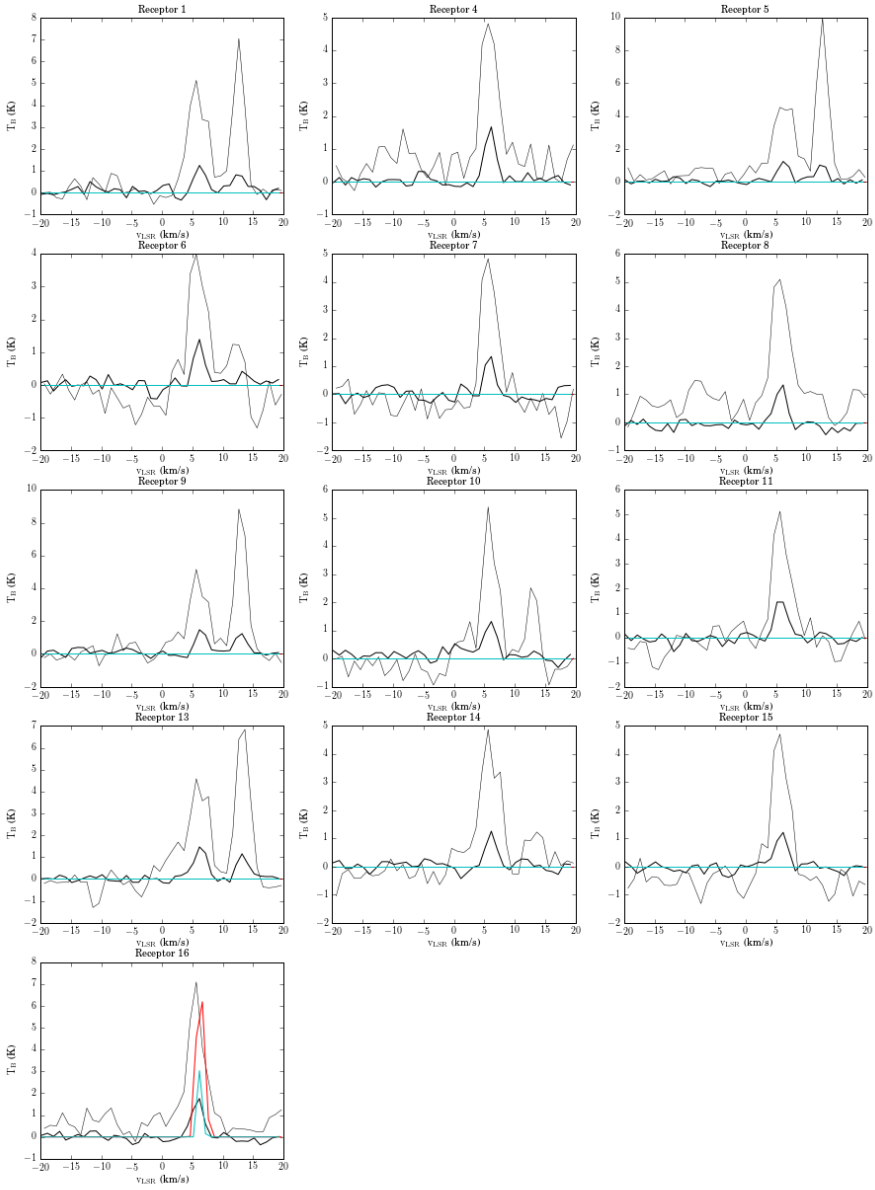

Faint Clouds CO(1-0) Spectrum: Cygnus X5

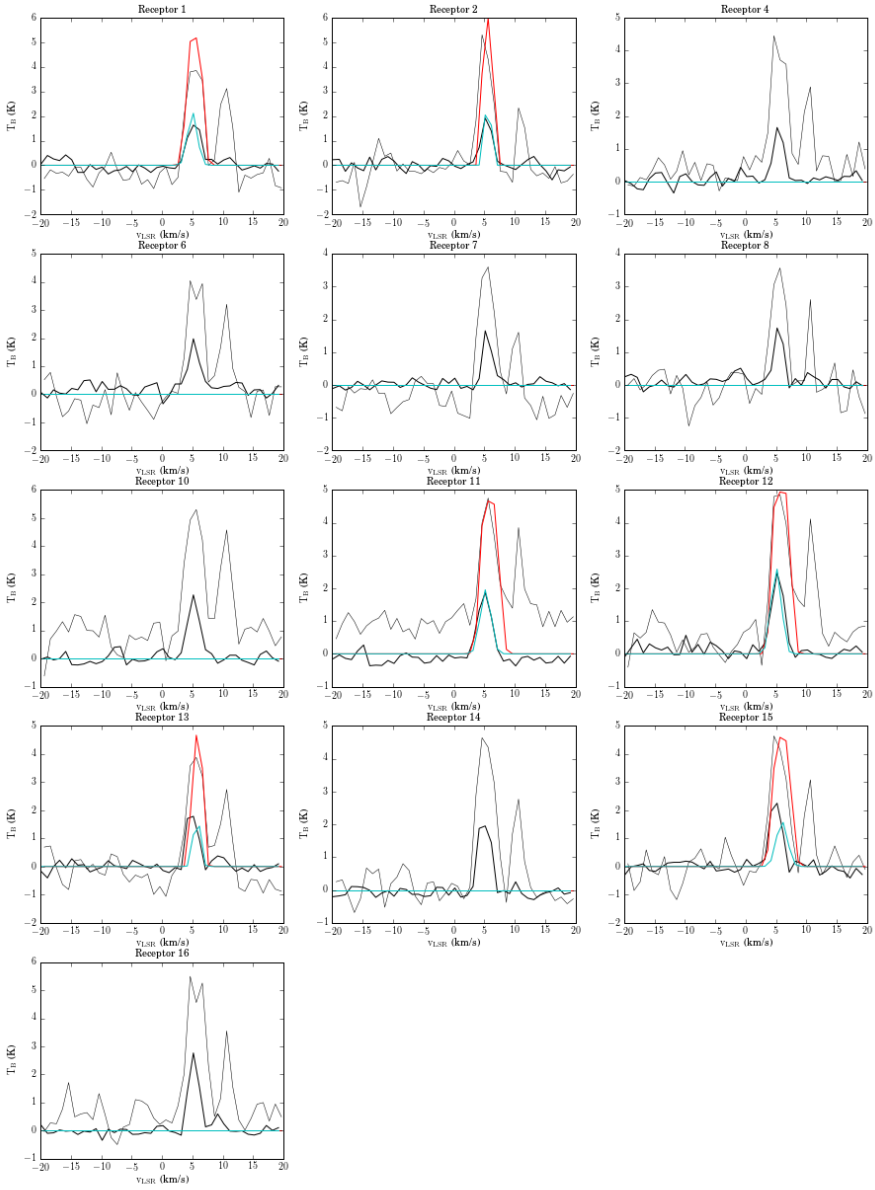

Faint Clouds CO(1-0) Spectrum: Cygnus X6

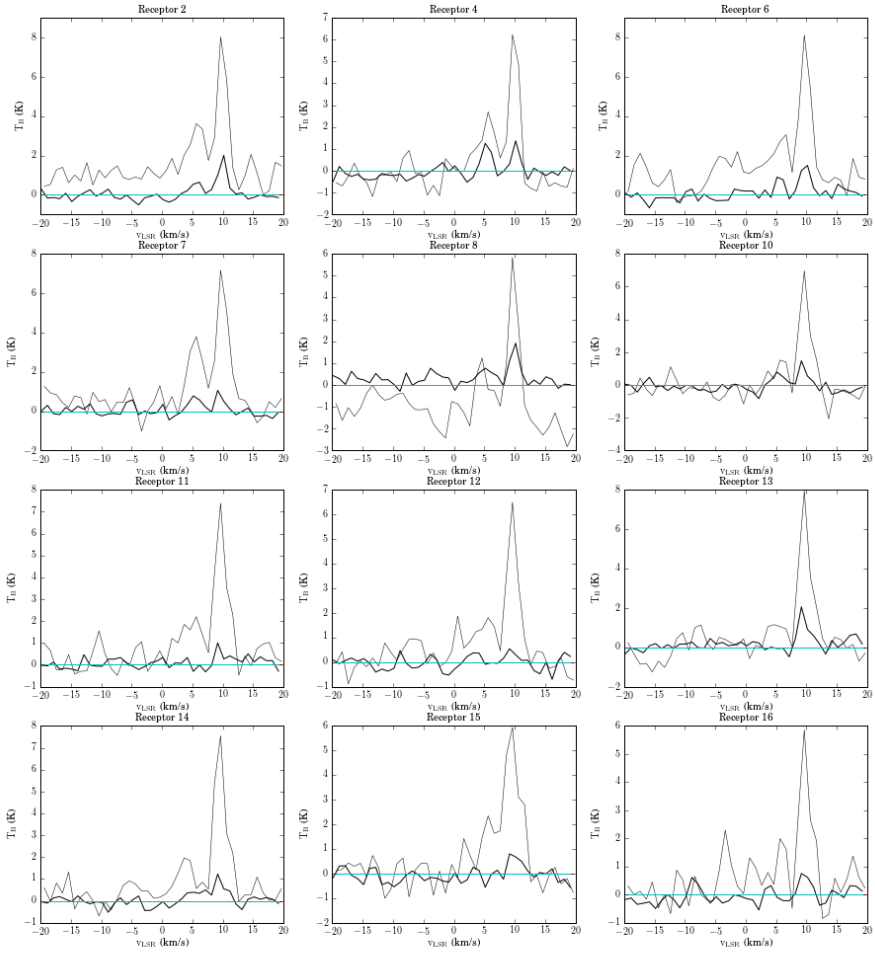

Faint Clouds CO(1-0) Spectrum: Cygnus X7

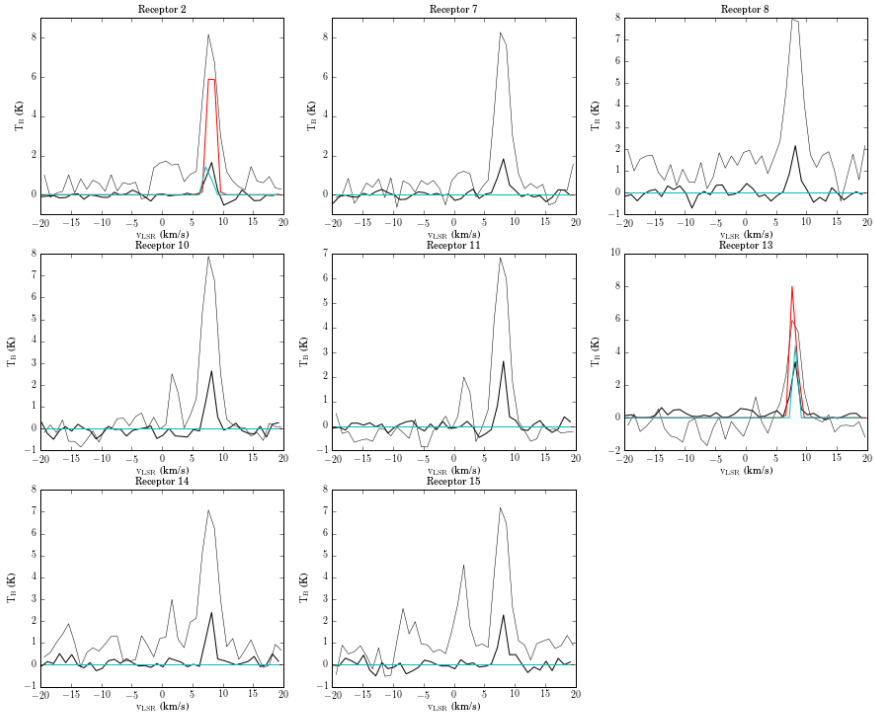

Faint Clouds CO(1-0) Spectrum: Cygnus X9

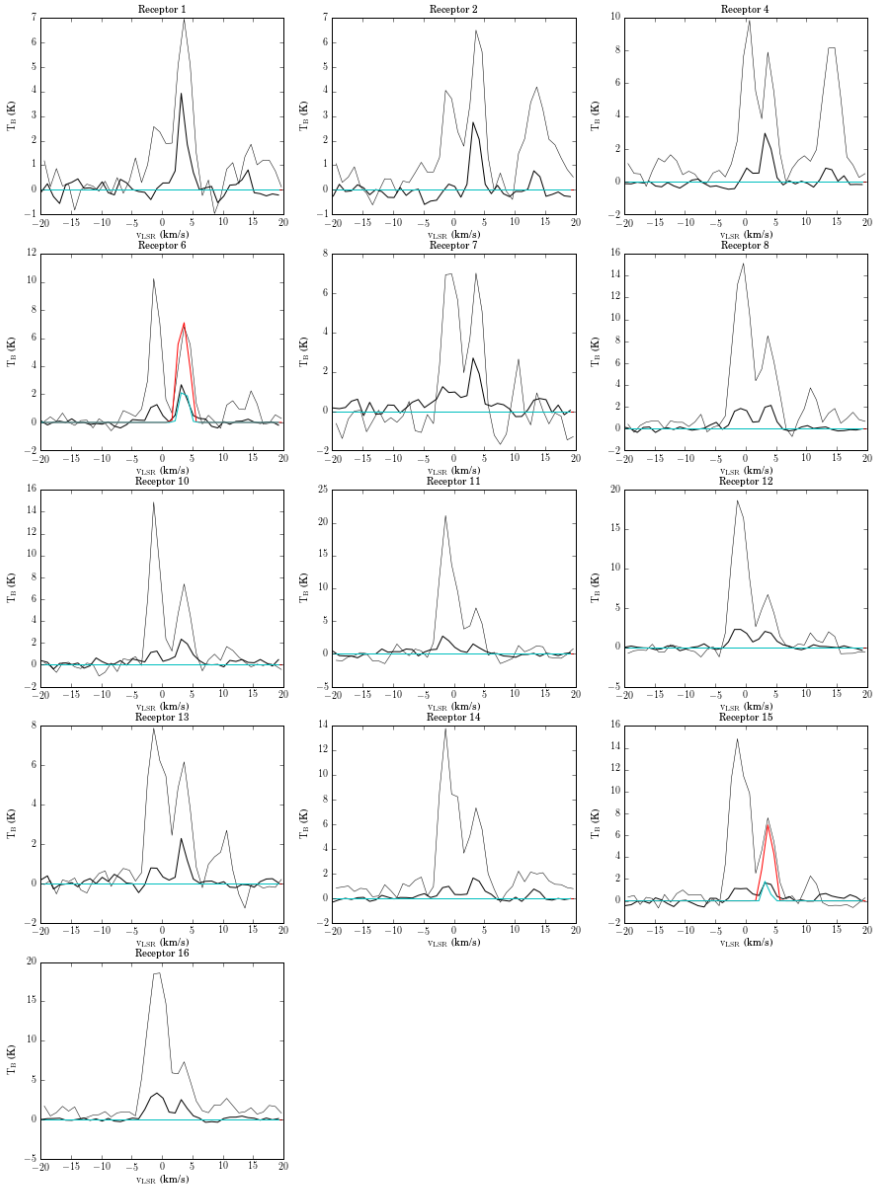

Bright Clouds CO(1-0) Spectrum: Cygnus X1

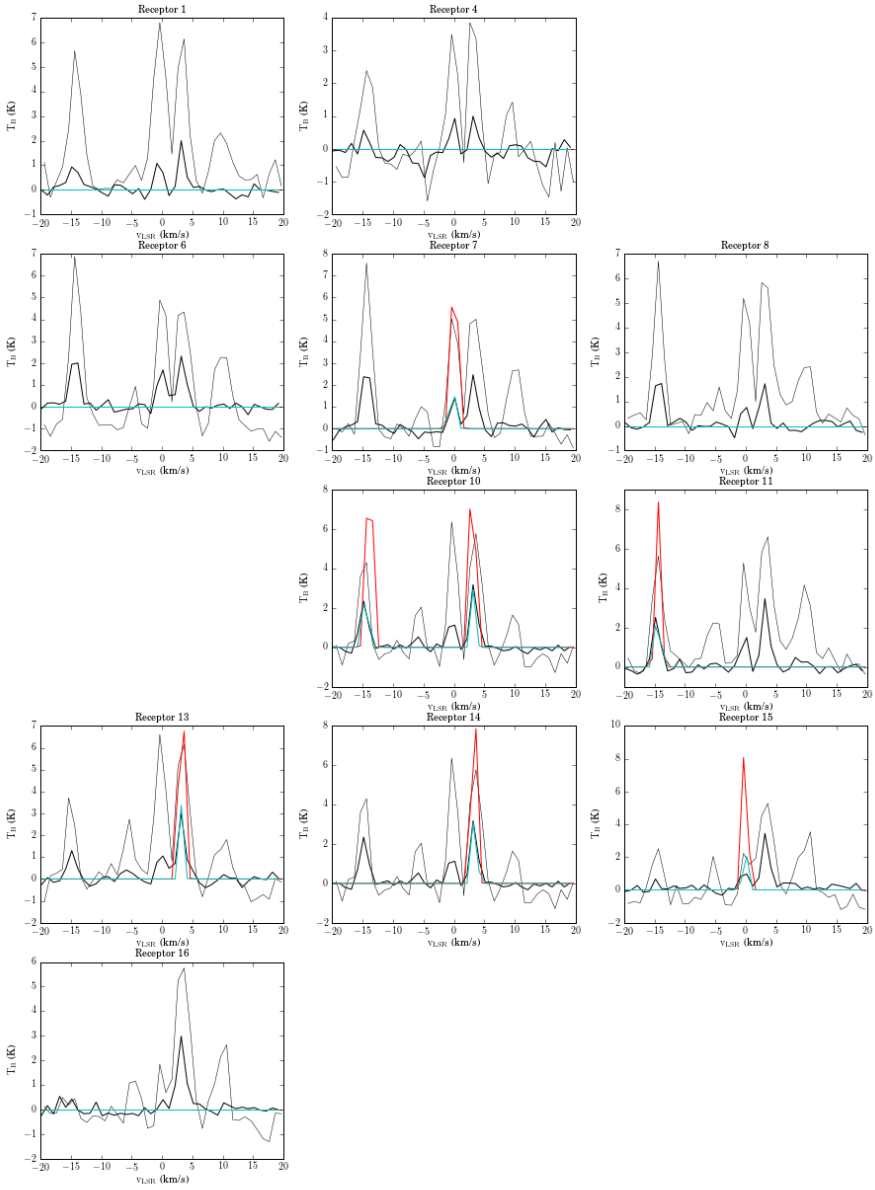

Bright Clouds CO(1-0) Spectrum: Cygnus X2

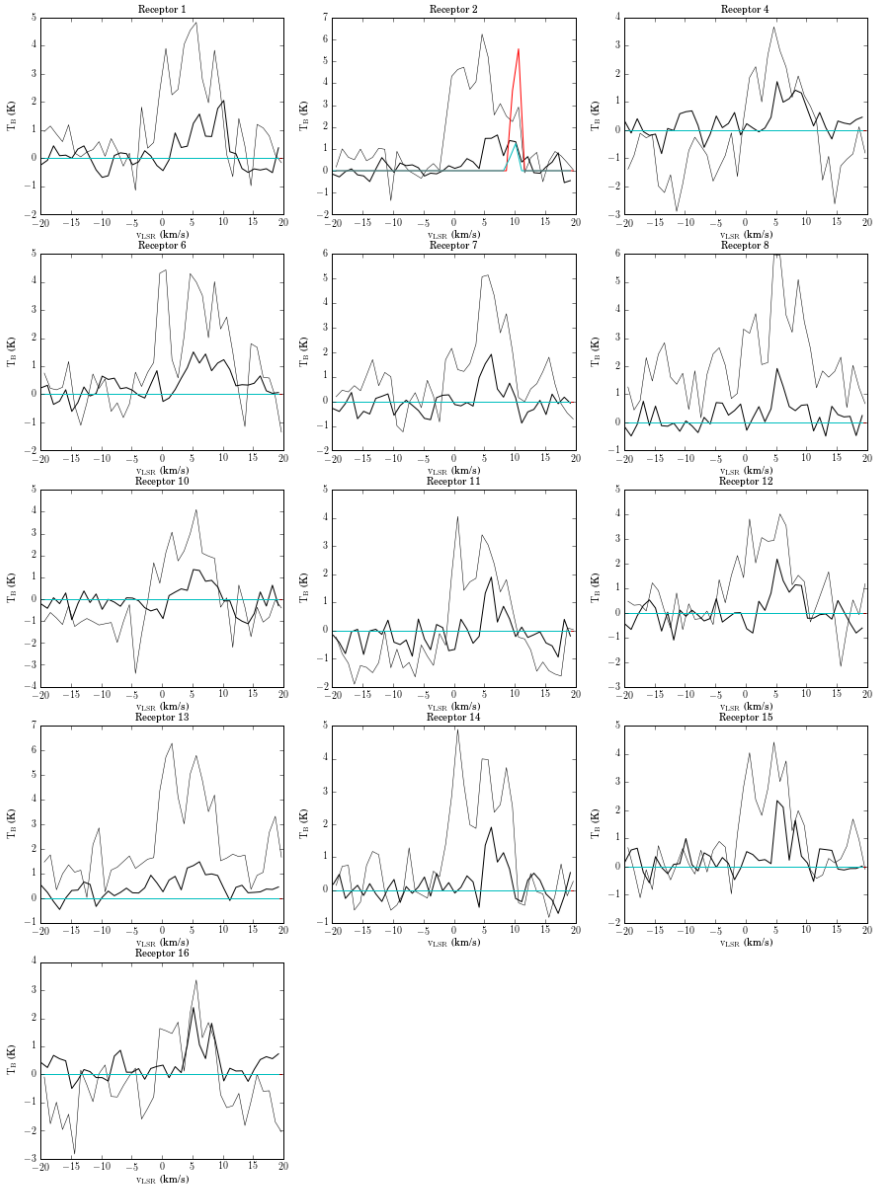

Bright Clouds CO(1-0) Spectrum: Cygnus X3

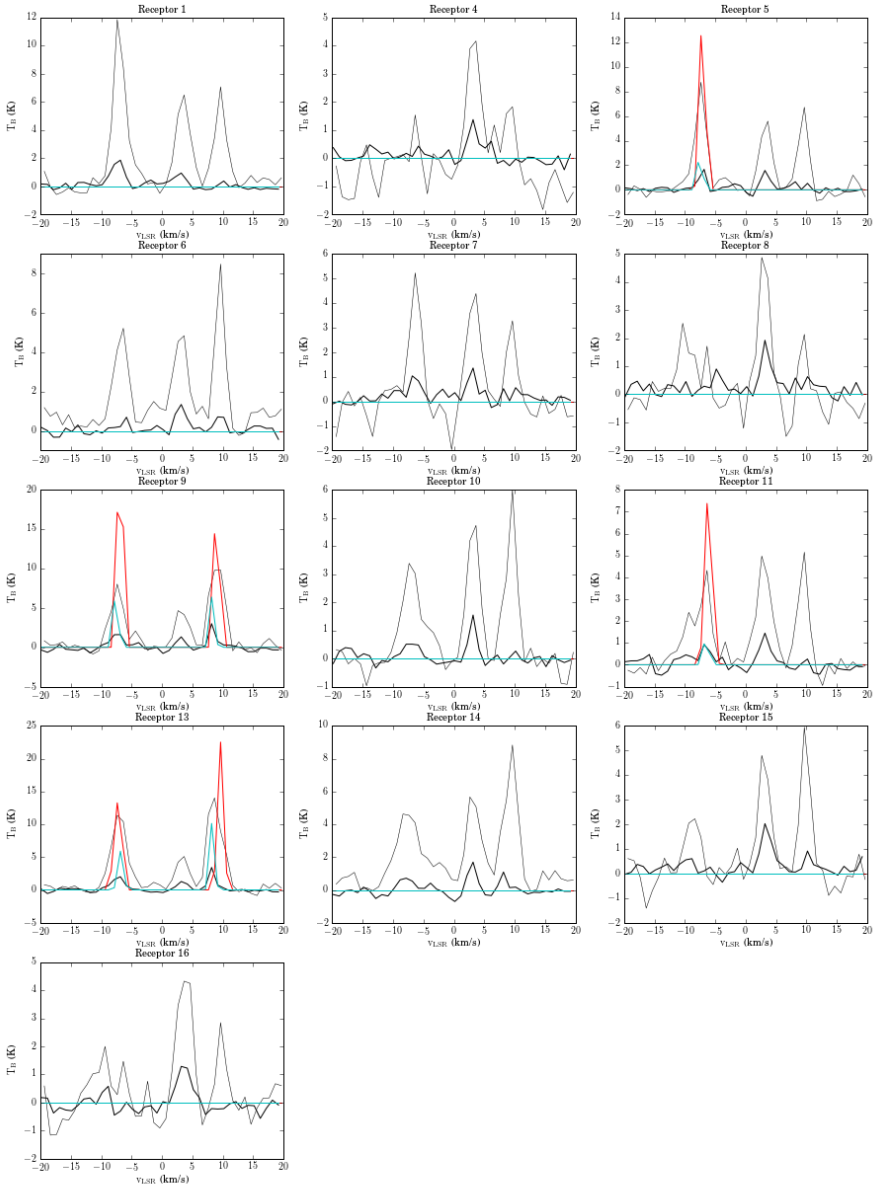

Bright Clouds CO(1-0) Spectrum: Cygnus X4

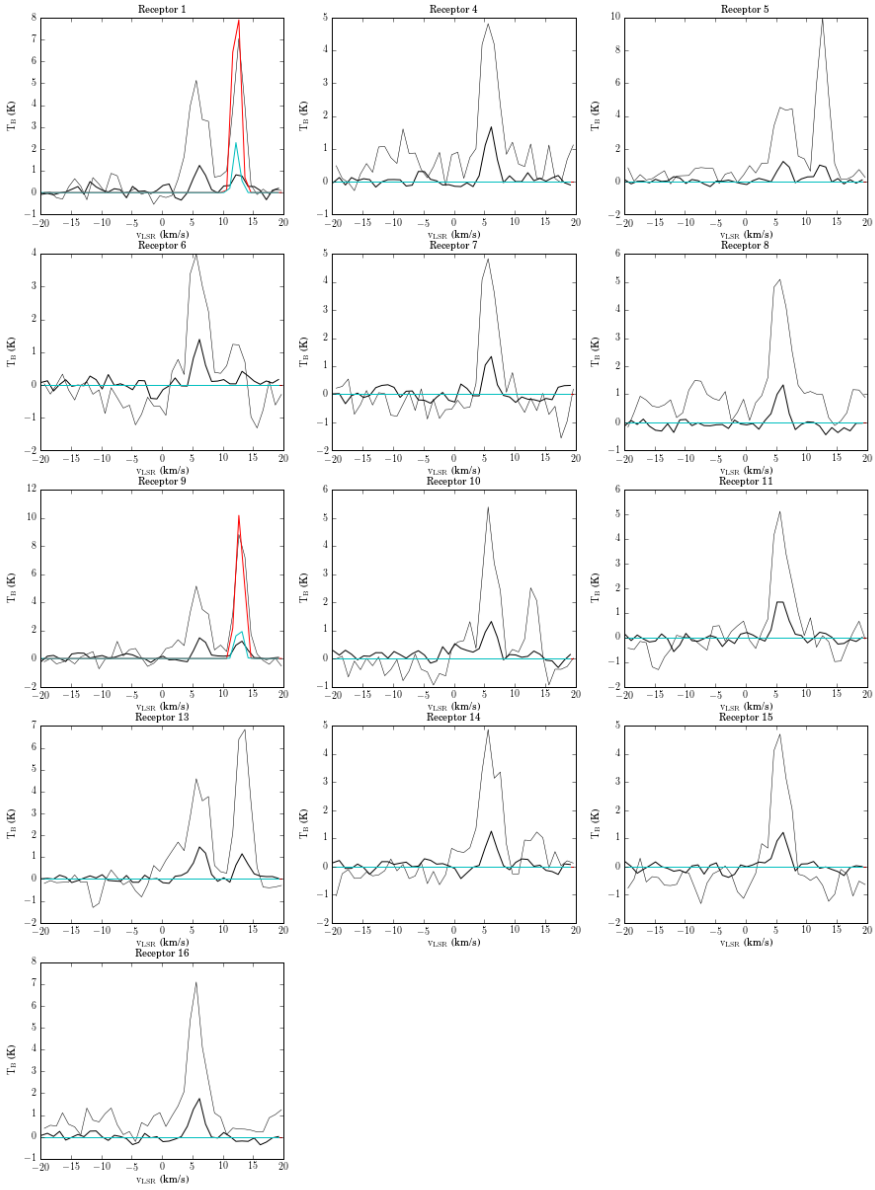

Bright Clouds CO(1-0) Spectrum: Cygnus X5

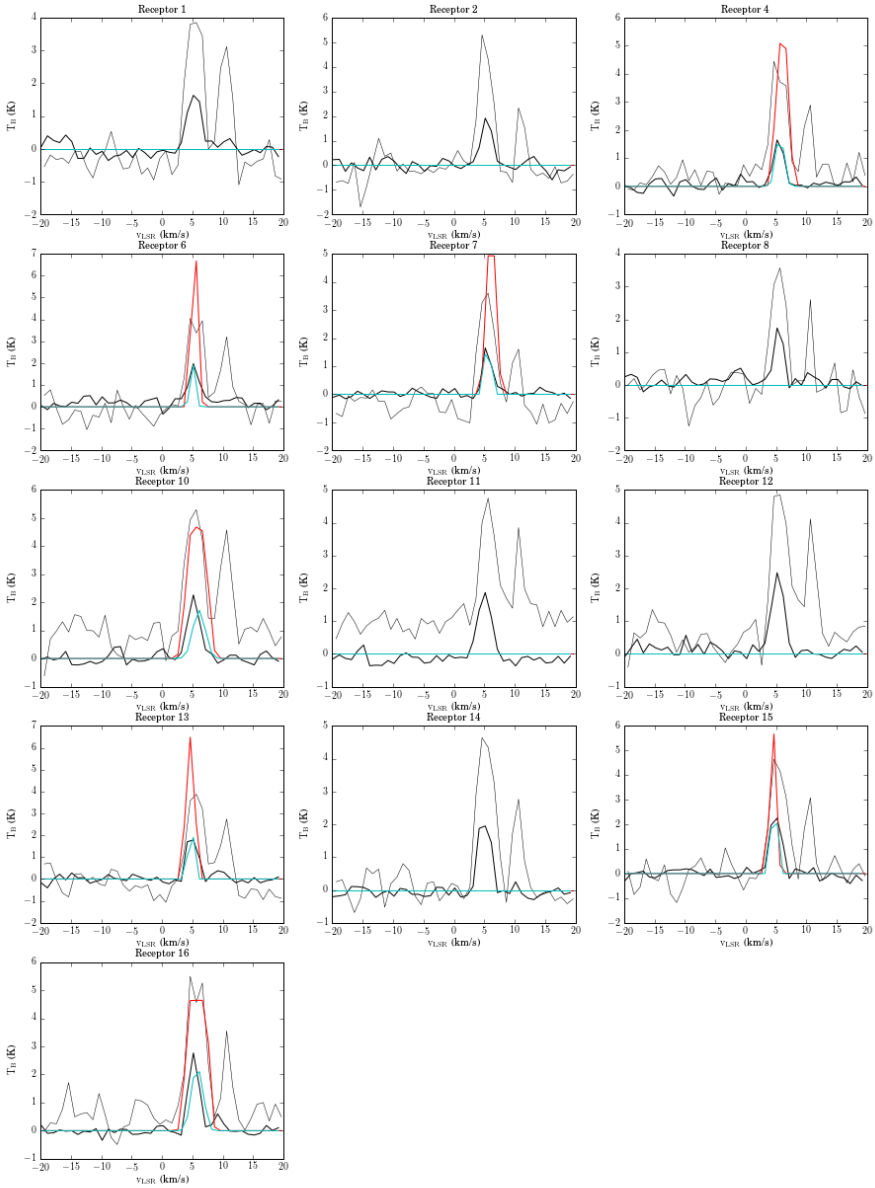

Bright Clouds CO(1-0) Spectrum: Cygnus X6

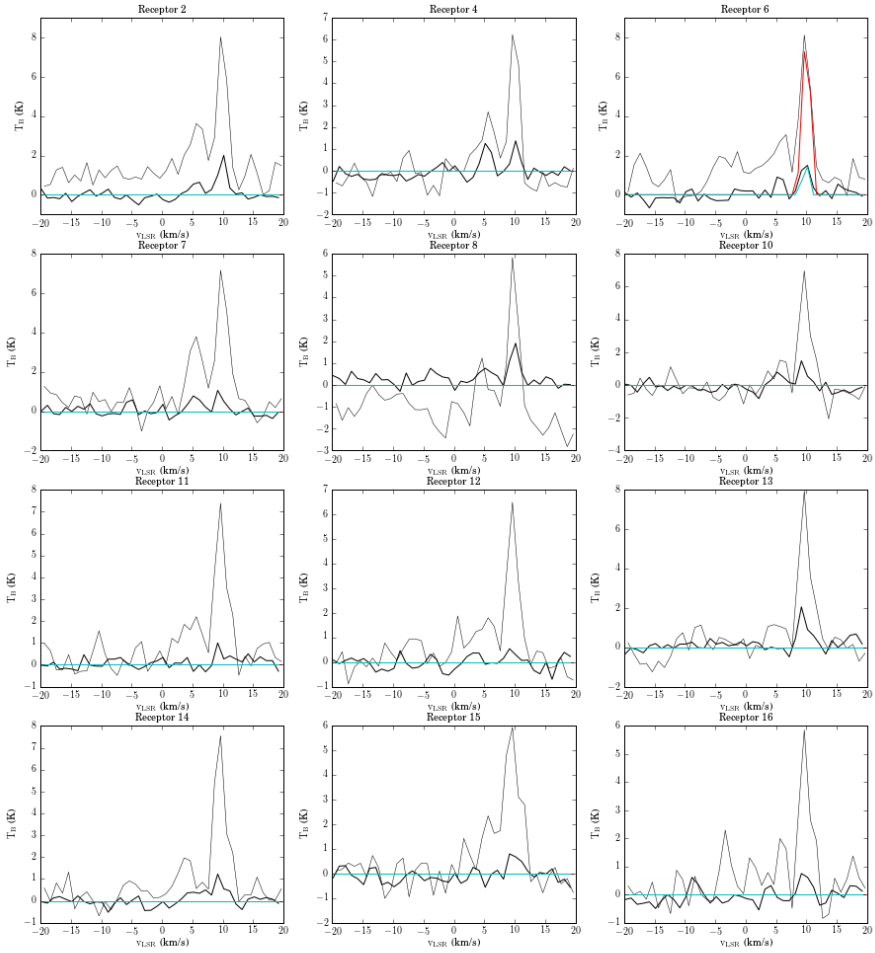

Bright Clouds CO(1-0) Spectrum: Cygnus X7

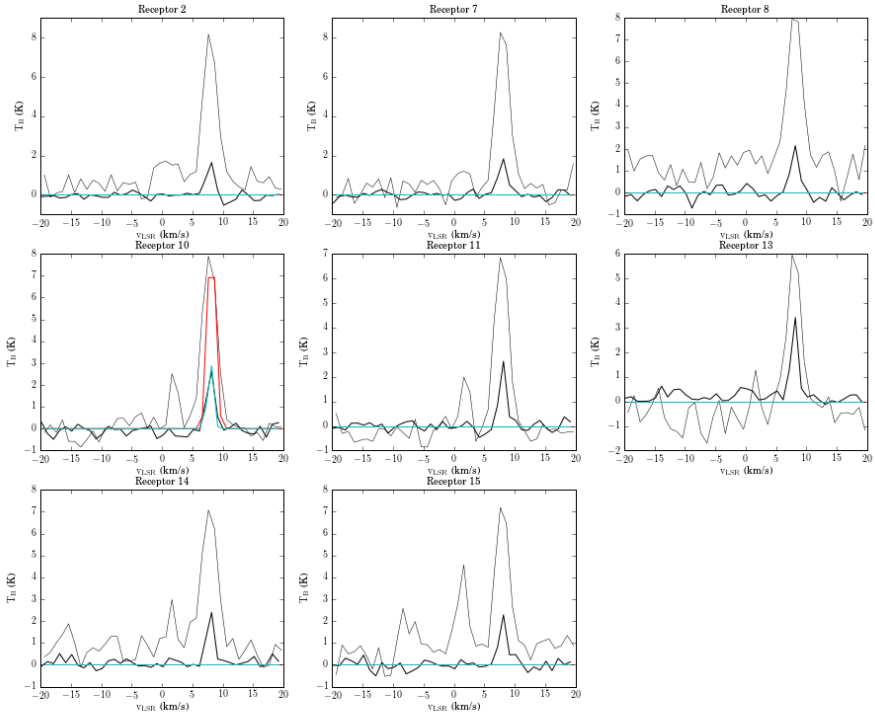

Bright Clouds CO(1-0) Spectrum: Cygnus X8

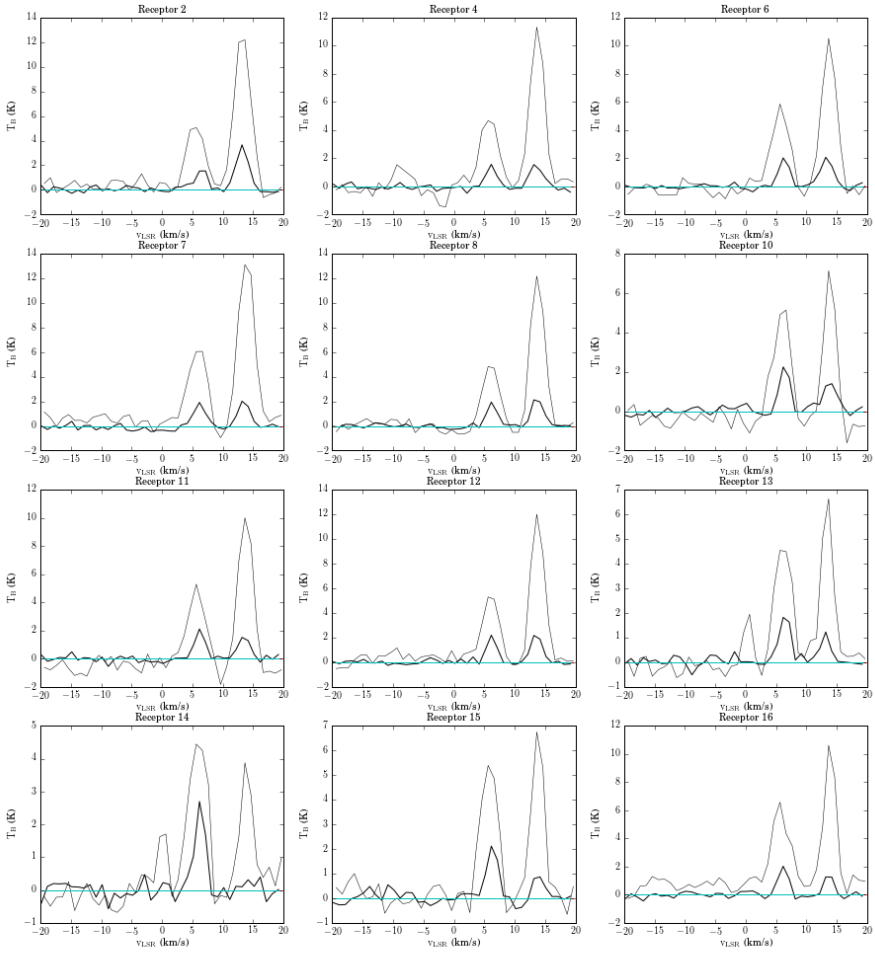

Bright Clouds CO(1-0) Spectrum: Cygnus X9